UCL Université catholique de Louvain

École polytechnique de Louvain (EPL)

epl

Large Eddy Simulation of a three-dimensional turbulent mixing layer by means of a Vortex Particle-Mesh method

Dissertation presented by
David HENNEAUX

for obtaining the Master's degree in
Mechanical Engineering

Supervisors
Philippe CHATELAIN, Grégoire WINCKELMANS

Readers
Matthieu DUPONCHEEL, Vincent LEGAT

Academic year 2016-2017

Acknowledgments

I would like to begin by thanking all the professors and assistants of EPL. Their skills and dedication have made all the courses that I have followed very exciting. They have especially conveyed to me the desire to learn and a taste for science in general. These 5 years of studies have passed very quickly and will leave me with very good memories.

To finish these studies, I had the chance to produce this master thesis in a field that I am passionate about : fluid mechanics. I would like to thank my two supervisors, Philippe Chatelain and Grégoire Winckelmans, for their coaching throughout this project. They gave me a taste of the joys and frustrations of numerical simulation and I come out of this dissertation convinced that I want to increase my knowledge in this exciting field. In particular, I thank them for giving me the opportunity to use a research code of this scope (VPM). This experience has taught me a lot of things and made me aware of the tremendous amount of work behind any simulation software. Finally, I appreciated the time they spent with me during their busy schedule and the extremely interesting discussions I had with them.

I would also like to express my gratitude to Denis-Gabriel Caprace for his great help and valuable advice. There is no doubt that without him this work wouldn't be as complete. I particularly appreciated his kindness and availability.

Finally, I would like to thank Matthieu Duponcheel and Vincent Legat for accepting to be the readers of this dissertation.

Computational resources have been provided by the Consortium des Équipements de Calcul Intensif (CÉCI), funded by the Fonds de la Recherche Scientifique de Belgique (F.R.S.-FNRS) under Grant No. 2.5020.11.

The present research benefited from computational resources made available on the Tier-1 supercomputer of the Fédération Wallonie-Bruxelles, infrastructure funded by the Walloon Region under the grant agreement No. 1117545.

Contents

List of symbols

$\boldsymbol{\omega}$	vorticity field
ΔU	velocity difference between U_1 and U_2
δ_ω	vorticity thickness
δ_{vis}	visual thickness
η	similarity variable
$\lambda_x,\ \lambda_z$	fundamental wavelengths of the Kelvin-Helmholtz instabilities
$\mathbf{v}'$	fluctuating velocity field
$\overline{\mathbf{v}}$	temporal mean velocity field
$\overline{k}$	mean turbulent kinetic energy
$\overline{T}$	Townsend term
θ	momentum thickness
u	streamwise velocity
$U_1,\ U_2$	upper and lower free stream velocities
U_c	convection velocity
v	transverse velocity
w	spanwise velcocity
y^*	position of the dividing streamline
$y_{0.5}$	position where the mean velocity is equal to the convection velocity

List of Figures

Introduction

This master thesis is about the numerical simulation of a *spatially-developing incompressible three-dimensional turbulent mixing layer*. This flow configuration is one of the most studied problems of fluid dynamics, as it is considered to be of fundamental importance in many practical engineering applications. It was first studied experimentally in laboratory apparatus. With the ever-increasing power of computers and the development of new numerical methods, it is now possible to simulate this flow on a computer and to obtain results comparable to experimental results.

A mixing layer flow forms when two streams of differing velocities meet at the end of a partition wall. The velocity difference creates a region of shear where the two originally separated fluids mix. This mixing region in which velocity and scalar properties depart from their free-stream values grows with downstream distance. There are two main characteristics in a mixing layer. The first one is the self-similarity property of the mean velocities and turbulent statistics that present the same profiles for different downstream locations when they are made dimensionless with the appropriate variable. The second one is the presence of large-scale organized vortex-like structures. These structures contain most of the turbulent kinetic energy and play an important role in the momentum transportation in the mixing layer. It is therefore important to describe the characteristics of these structures and accurately predict their evolution.

The numerical simulation carried out in the framework of this dissertation was made by means of a CFD solver used and developed by the researchers of UCL. The first step of this thesis was to correctly define the features of the solver to be used in order to carry out the simulation. Then, with the collaboration of the supervisors and assistant, some modifications had to be made in the code in order to make it operational. Afterwards, the rigorous selection of simulation parameters was done before running the final simulation. Finally, the last step was to get the results back, to process them and analyze them.

The first chapter describes in a more detailed manner the characteristics of the mixing layer and the objectives of this thesis. Some manipulations of the Navier-Stokes equations for the case of a mixing layer flow are also presented.
The second chapter deals with the numerical method implemented in the solver used for the simulation.
The third chapter explains the choices of the simulation parameters as well as the few modifications made in the code.
Finally, the results are presented and commented in the last chapter.

1 The mixing layer

1.1 Introduction

In this first chapter, the mixing layer flow is presented by successively addressing the interest of its understanding, its turbulent structure as well as the parameters that define it. Then, the objectives of this dissertation are exposed in the light of the work already done on the same subject. Finally, the general equations of fluid mechanics are recalled and their simplification for the case under consideration is developed.

1.2 Description of the flow

The mixing layer flow belongs to the family of boundary–free shear flows, such as wake flows or jets. The structure of such kind of flows evolves in the flow direction, not because of external influences such as pressure or temperature gradients, but only «under the influence of their own evolutionary tendencies» [13]. Moreover, they are not affected by the presence of a solid surface. In particular, a mixing layer forms when two parallel uniform flows of different velocities come into contact. This velocity difference creates a shear layer between the two free streams which grows in thickness with downstream distance. The situation is illustrated in figure 1.1.

This figure schematizes the initial velocity profile and the subsequent development of the mixing layer through a series of rollers that grow with downstream distance. U_1 and U_2 are the velocities of the two streams outside of the shear layer, where the flow is uniform. For the rest of the report, $U_1 > U_2$. Note that this discontinuous theoretical velocity profile is never met in reality, it is simply drawn as an illustration of the situation. Moreover, the rollers that are drawn are the ones of a flow in which three-dimensional effects due to turbulence are not present. In chapter 4, views of an actually three-dimensional turbulent mixing layer are presented. The coordinate axis represented on figure 1.1 will be used throughout this report and the corresponding velocity field is defined as :

$$\mathbf{v} = (v_x,\ v_y,\ v_z) = (u,\ v,\ w).$$

Moreover, the designation of the different directions will be as follows :

$$x \text{ direction} \equiv \text{streamwise direction},$$

$$y \text{ direction} \equiv \text{transverse direction},$$

$$z \text{ direction} \equiv \text{spanwise direction}.$$

In reality, the domain in which the mixing layer develops is infinite. Here, for the simulation, the computational domain needs to have finite dimensions that are denoted by $(L_x,\ L_y,\ L_z)$.

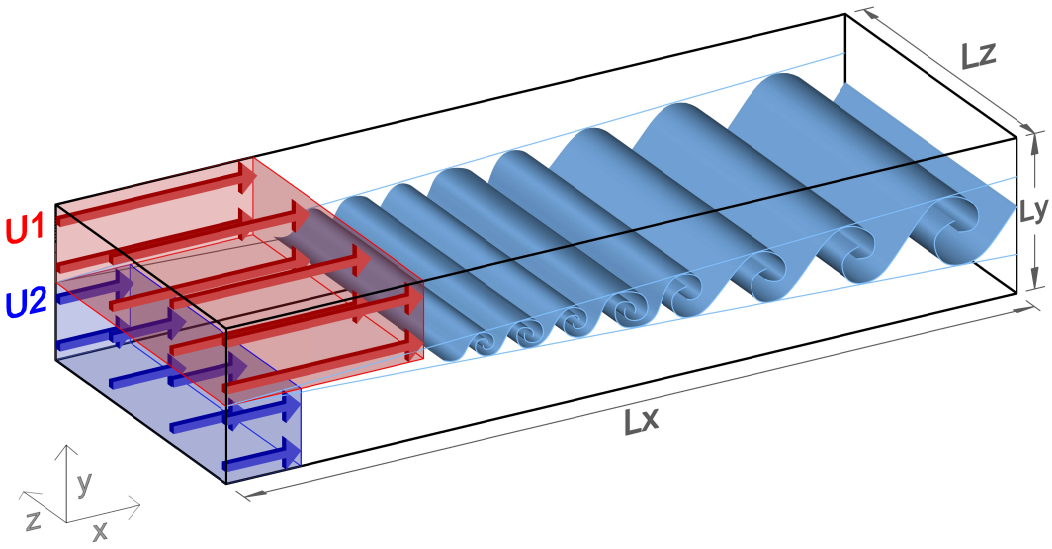

Figure 1.1: Schematic of a mixing layer

1.2.1 Motivations

In laboratory experiments, a mixing layer is formed at the end of a thin splitter plate when the upper and lower flows meet.
Mixing layers appear within many other flows such as in the initial part of a jet, more precisely at the interface between the edges of the jet flow and the quiescent surroundings flow. They also appear when a boundary layer flow separates from a solid surface.
From a practical point of view, mixing layers play a particularly important role in many combustion systems or mixers in the chemical industry. Since turbulence favors mixing due to its important diffusivity, they are used to optimize the mixing rate between two flows of different fluids. The understanding of the development and the structure (see 1.2.2) of a mixing layer is then of key importance in order to design such kind of systems [1]. They are also present in other applications, for example in aeropropulsion they influence the noise produced by a turbofan engine [7] while in structural mechanics, they induce vibrations [1].

1.2.2 Flow physics

Mixing layer flows all exhibit large-scale structures, often called “coherent structures”. Many experiments and numerical simulations has been conducted to understand the development and the mechanisms of those structures. Below, a short explanation tries to synthesize the main concepts resulting from years of researches [7], [1].

The discontinuities in the initial velocity profile either from the boundary layer flows emanating from the splitter plate, or from a more smooth discontinuity like the one in a hyperbolic tangent profile (see section 3.3) introduce some instabilities in the flow. These hydrodynamic instabilities, called the Kelvin-Helmholtz instabilities, are unstable over the whole range of Reynolds numbers. It can be shown by using the linear stability theory that an instability with a particular wavelength will be amplified more rapidly than the others and will determine the development of the flow

(see appendix A for more details). This property will be exploited for the initial condition of the simulations (see section 3.3).
When initiated, the Kelvin-Helmholtz instabilities grow in amplitude, which causes the mixing layer to roll-up into large spanwise vortices.
These vortices are convected downstream and the mixing layer starts to grow via 2 mechanisms. The first one is the entrainment of the fluid outside of the shear layer. The second one is the pairing of adjacent vortices which first rotate around each other before coalescing to form a larger vortex. This growth mechanism remains essentially two-dimensional and occurs in the initial development zone of the flow.
Then, further downstream, in the transition zone, secondary streamwise vortices develop in the "braid region" between successive primary spanwise rollers, «under the influence of positive strain existing in that region»[1]. The secondary structures interact with the primary ones, causing a distortion of the spanwise vortices and leading to three–dimensionality. Turbulence commences !
Finally in the fully developed (or fully turbulent) region of the flow, one observes a quasi-linear growth of the layer with the streamwise distance. The structures continue to merge but the growth mechanism can be different here : the structures can continuously grow individually without any interactions. In this region, the mean and fluctuating velocity profiles, measured at distinct streamwise locations, collapse if they are scaled with the appropriate similarity variable. It is called the self-similarity region.

1.2.3 Spatial versus temporal growths

It is important to differentiate between a spatially-developing and a time-developing mixing layer. In this dissertation, the first instance is considered. It is the "physical" example in laboratory coordinates. The second case can be seen by an observer moving in the streamwise direction at the convection speed U_c. If the ratio between the velocity difference ΔU and the convection speed tends to zero, the observer will see two flows moving in opposite directions at $1/2 \cdot \Delta U$ and $-1/2 \cdot \Delta U$, respectively [30]. A lot of numerical simulations of time-developing mixing layers were realized because of their relatively cheap simulation compared to the spatially-developing case. Indeed, the streamwise direction is chosen to be periodic, which avoids having to consider a very long domain. But, as mentionned in [37], «because the spatially-developing mixing layer does not adopt a periodic assumption in the streamwise direction, it could be an exact description of the mixing layer used in many applications» as it includes «the feedback interactions between upstream and downstream».

1.3 Position of the thesis

As already mentioned, the mixing layer is a classical and highly studied problem in fluid mechanics for its technological importance. A lot of works, either experimental or numerical, covering all the aspects of this key situation have been conducted and are still conducted nowadays (just look at the publication dates of the articles in the bibliography).
In the vast domain of mixing layer flows, it is important to situate the objectives of this master thesis.
One of the reference work in this domain is the experience conducted by Brown and Roshko in 1974 [11]. In their apparatus, they studied the mixing layer between two streams of different gases. One of their main discoveries has been the observation of large coherent structures at high Reynolds number. «Before this discovery coherent structures were considered a peculiar feature of the low Reynolds number mixing layer» [1]. In particular, they showed that the density difference effects are relatively small on the development of this large-scale structures. They also considered the case of homogeneous flows (with the same density) by conducting an experience with two streams of air, moving respectively at $U_1 = 1000$ $[cm/s]$ and $U_2 = 382$ $[cm/s]$. The

results of this experience will be used to assess the results of the present simulation. Therefore, the ratio between the upper and lower velocities U_1/U_2 will be chosen as equal to the one of the experiment.
Just to give an idea of other subjects already tackled, here is a non-exhaustive list with some references :

- inflow conditions effects :
  - shape of the incoming velocity profiles [35] ;
  - shape of the trailing edge of the splitter plate [33] ;
- influence of the numerical ingredients [3] ;
- relations between coherent fine scale eddy and laminar – turbulent transition [37] ;
- initial conditions effects on the Kelvin-Helmholtz roll-up, pairings and transition to turbulence [22], [23] ;
- compressibility effects [32].

The goal of this thesis is neither to study the influence of some parameters (physical or numerical), nor to study a feature of the mixing layer structure. This work therefore does not explore new aspects of the mixing layer topic. The main objective is rather to produce a simulation which is accurate while having quite a large computational domain. To achieve this objective, a large number of mesh points were used. Moreover, with this very good resolution and the LES model implemented in the code, a high initial Reynolds number could be chosen. It is undoubtedly these two characteristics which distinguish this study from previous works (see section 3.6.3).
To perform the simulation, the in-house VPM solver, which has never been used in this kind of situation, is employed. The second goal of the thesis is therefore to assess the code against classical results and to show how efficient it can be to simulate free shear flows.

1.4 Governing equations

1.4.1 Navier-Stokes equations

The general conservation equations for mass and momentum are written under their local forms in equation (1.1) in which ρ is the density in $[kg/m^3]$ and $\mathbf{v}$ is the velocity vector with units in $[m/s]$.

$$\begin{aligned} \frac{D\rho}{Dt} + \rho \boldsymbol{\nabla} \cdot \mathbf{v} = 0, \\ \rho \frac{D\mathbf{v}}{Dt} = \boldsymbol{\nabla} \cdot \boldsymbol{\sigma} + \mathbf{f}. \end{aligned} \tag{1.1}$$

The last equation relates the acceleration of a fluid particle expressed by the left-hand side term to the surface forces contained in the stress tensor $\boldsymbol{\sigma}$, and the body forces contained in the vector $\mathbf{f}$. In this report, the body forces (such as the gravity) will be neglected. The material derivative D/Dt is defined to be

$$\frac{D}{Dt} = \frac{\partial}{\partial t} + \mathbf{v} \cdot \boldsymbol{\nabla} \ . \tag{1.2}$$

The stress tensor for a Newtonian fluid can be decomposed as such

$$\boldsymbol{\sigma} = -p\boldsymbol{\delta} + \boldsymbol{\tau} = -p\boldsymbol{\delta} + 3\kappa \mathbf{d}^s + 2\mu \mathbf{d}^d \ , \tag{1.3}$$

where p is the thermodynamic pressure, μ and κ are the shear and bulk viscosity, respectively, and $\mathbf{d}^s$ and $\mathbf{d}^d$ are the spheric and deviatoric parts, respectively, of the strain rate tensor given by

$$\mathbf{d} = \frac{1}{2}\left(\boldsymbol{\nabla}\mathbf{v}^T + \boldsymbol{\nabla}\mathbf{v}\right) . \tag{1.4}$$

The studied flow is an incompressible flow (i.e. with a constant density) with constant coefficients (i.e. independent of pressure or temperature variations) and for such a kind of flow, the equation (1.1) can be written under the following form

$$\begin{aligned} \boldsymbol{\nabla}\cdot\mathbf{v} &= 0, \\ \frac{D\mathbf{v}}{Dt} &= -\boldsymbol{\nabla}\mathrm{P} + \nu\boldsymbol{\nabla}^2\mathbf{v}, \end{aligned} \tag{1.5}$$

where $\mathrm{P} = p/\rho$ is the modified pressure and $\nu = \mu/\rho$ the kinematic viscosity.

1.4.2 Reynolds equations

The studied flow is turbulent, which means that there are a lot of fluctuations in the velocity and pressure fields. It is therefore interesting to express these quantities as the sum of a mean quantity and a fluctuating one, as it is shown in the equation (1.6) :

$$\mathbf{v}(\mathbf{x},t) = \overline{\mathbf{v}}(\mathbf{x},t) + \mathbf{v}'(\mathbf{x},t) \quad \mathrm{P}(\mathbf{x},t) = \overline{\mathrm{P}}(\mathbf{x},t) + \mathrm{P}'(\mathbf{x},t), \tag{1.6}$$

where $\mathbf{v}'$ is the fluctuating part of the velocity field and

$$\overline{\mathbf{v}}(\mathbf{x},t) = \frac{1}{T}\int_{t-T/2}^{t+T/2} \mathbf{v}(\mathbf{x},\tau)\mathrm{d}\tau \tag{1.7}$$

is the mean component (the same notations apply for the pressure). The time T in which the average is computed needs to be "sufficiently large". Let us note that these notations for the mean and fluctuating components will be used throughout the report.
The Reynolds equations (or *RANS* equations) are obtained from the Navier-Stokes equations (1.5) by applying the mean temporal operator (equation (1.7)). In indicial notations, those equations are formulated as follows [1] :

$$\begin{aligned} \frac{\partial\overline{u_i}}{\partial x_i} &= 0, \\ \frac{\partial\overline{u_i}}{\partial t} + \overline{u_j}\frac{\partial\overline{u_i}}{\partial x_j} &= -\frac{\partial\overline{\mathrm{P}}}{\partial x_i} + \nu\frac{\partial^2\overline{u_i}}{\partial x_j\partial x_j} - \frac{\partial}{\partial x_j}(\overline{u_i'u_j'}). \end{aligned} \tag{1.8}$$

Compared to equation (1.5), one additional term involving fluctuating velocities appears : $-\overline{u_i'u_j'}$. This term (multiplied by ρ) is an additional stress and contributes to the stresses involved in the momentum equation in the same way as the the viscous stresses and the isotropic stresses from the mean pressure field. It forms the so-called Reynolds stress tensor.

[1] More precisely, those equations are the Unsteady RANS equations as the time derivative appears

In three dimensions, when the equation (1.8) is developed, the equations for the mean velocity field read :

$$
\begin{aligned}
&\frac{\partial \overline{u}}{\partial x}+\frac{\partial \overline{v}}{\partial y}+\frac{\partial \overline{w}}{\partial z}=0,\\
&\frac{\partial \overline{u}}{\partial t}+\overline{u}\frac{\partial \overline{u}}{\partial x}+\overline{v}\frac{\partial \overline{u}}{\partial y}+\overline{w}\frac{\partial \overline{u}}{\partial z}=-\frac{\partial \overline{\mathrm{P}}}{\partial x}+\nu\left(\frac{\partial^2\overline{u}}{\partial x^2}+\frac{\partial^2\overline{u}}{\partial y^2}+\frac{\partial^2\overline{u}}{\partial z^2}\right)-\left(\frac{\partial}{\partial x}(\overline{u'^2})+\frac{\partial}{\partial y}(\overline{u'v'})+\frac{\partial}{\partial z}(\overline{u'w'})\right),\\
&\frac{\partial \overline{v}}{\partial t}+\overline{u}\frac{\partial \overline{v}}{\partial x}+\overline{v}\frac{\partial \overline{v}}{\partial y}+\overline{w}\frac{\partial \overline{v}}{\partial z}=-\frac{\partial \overline{\mathrm{P}}}{\partial y}+\nu\left(\frac{\partial^2\overline{v}}{\partial x^2}+\frac{\partial^2\overline{v}}{\partial y^2}+\frac{\partial^2\overline{v}}{\partial z^2}\right)-\left(\frac{\partial}{\partial x}(\overline{u'v'})+\frac{\partial}{\partial y}(\overline{v'^2})+\frac{\partial}{\partial z}(\overline{v'w'})\right),\\
&\frac{\partial \overline{w}}{\partial t}+\overline{u}\frac{\partial \overline{w}}{\partial x}+\overline{v}\frac{\partial \overline{w}}{\partial y}+\overline{w}\frac{\partial \overline{w}}{\partial z}=-\frac{\partial \overline{\mathrm{P}}}{\partial z}+\nu\left(\frac{\partial^2\overline{w}}{\partial x^2}+\frac{\partial^2\overline{w}}{\partial y^2}+\frac{\partial^2\overline{w}}{\partial z^2}\right)-\left(\frac{\partial}{\partial x}(\overline{u'w'})+\frac{\partial}{\partial y}(\overline{v'w'})+\frac{\partial}{\partial z}(\overline{w'^2})\right).
\end{aligned}
\tag{1.9}
$$

1.4.3 Simplified equations

In a mixing layer, the spanwise dimension is sufficiently large so that the statistics of the flow vary little in this direction. Therefore the flow can be assumed to be statistically two-dimensional, which means that the statistics are independent of the spanwise direction ($\frac{\partial}{\partial z}(\bullet)=0$). This observation leads to neglect $\overline{w}$, $\overline{u'w'}$ and $\overline{v'w'}$ in equation (1.9). Note that $\overline{w'^2}$ cannot be neglected but still it will cancel since it appears as a derivative with respect to z. Moreover, the streamwise component of the velocity is dominant ($\overline{u} >> \overline{v}$) and the transverse variations of the mean quantities are much more important than the streamwise ones ($\frac{\partial}{\partial y} >> \frac{\partial}{\partial x}$). Finally, the flow is also assumed to be statistically stationary such that $\frac{\partial \overline{u_i}}{\partial t}=0$. Gathering all those simplifications, the approximation of the Reynolds equations are obtained :

$$
\begin{aligned}
&\frac{\partial \overline{u}}{\partial x}+\frac{\partial \overline{v}}{\partial y}=0,\\
&\overline{u}\frac{\partial \overline{u}}{\partial x}+\overline{v}\frac{\partial \overline{u}}{\partial y}=-\frac{\partial \mathrm{P}_0}{\partial x}+\nu\frac{\partial^2\overline{v}}{\partial y^2}-\frac{\partial}{\partial y}(\overline{u'v'})-\frac{\partial}{\partial x}(\underbrace{\overline{u'^2}-\overline{v'^2}}_{\triangleq T}),
\end{aligned}
\tag{1.10}
$$

where the pressure term in the streamwise momentum equation has been transformed thanks to the transverse momentum equation, which introduced the free stream pressure P_0 and $\overline{v'^2}$ in the Townsend term T.

Further simplifications are possible. First, by Bernoulli's equation outside the mixing layer (where the flow is not turbulent and at a constant velocity), $\frac{\partial \mathrm{P}_0}{\partial x}=0$. Then, $\nu\frac{\partial^2\overline{v}}{\partial y^2}$ can be neglected in turbulent flow away from a wall (which is the case here) since the inertia effects dominate the viscous ones. Finally, the Townsend term is often neglected even though it introduces some errors in the approximation. One then ends up with the following equations, which are the boundary-layer approximation of the Reynolds equations :

$$
\begin{aligned}
&\frac{\partial \overline{u}}{\partial x}+\frac{\partial \overline{v}}{\partial y}=0,\\
&\overline{u}\frac{\partial \overline{u}}{\partial x}+\overline{v}\frac{\partial \overline{u}}{\partial y}=-\frac{\partial}{\partial y}(\overline{u'v'}).
\end{aligned}
\tag{1.11}
$$

In these equations, the Reynolds stresses $-\rho\overline{u'v'}$ remain unknown : they need to be modeled in order to close the problem. One way to do that is to use an effective turbulent viscosity model and to reproduce the model for the Newtonian fluid :

$$
\begin{aligned}
-\rho\overline{u_i'u_j'} &= \overline{\sigma_{ij}}^t\\
&= \overline{\tau_{ij}}^t+\frac{1}{3}\underbrace{\overline{\sigma_{ii}}^t}_{=-2\rho\overline{k}}\delta_{ij}
\end{aligned}
\tag{1.12}
$$

where $\overline{k}$ is the turbulent kinetic energy and $\overline{\tau_{ij}}^t$ is the deviatoric part of the Reynolds stress tensor which is modeled as

$$\overline{\tau_{ij}}^t = 2\mu_t \overline{d_{ij}} \tag{1.13}$$

by analogy with the Newtonian model for the shear stress tensor. By writing that, the 6 unknown of the Reynolds stresses are replaced with one unknown, the turbulent or eddy viscosity μ_t. Then, to be able to solve the equations, the eddy viscosity also needs to be modeled in order to close the problem. The most simple model for the boundary-layer equations is the algebraic uniform-turbulent-viscosity model[2], which consists in writing [30] :

$$\nu_t(x, y) = \frac{U_0(x)\delta(x)}{R_T}$$

where $U_0(x)$ and $\delta(x)$ are «the characteristic velocity scale and lengthscale of the mean flow» [30]. Here, $U_0(x)$ can be selected as a constant equal to the the high-speed free-stream velocity U_1 for example, and $\delta(x)$ is the visual thickness of the layer (see section 1.5) which grows linearly with the streamwise location x as $\delta(x) = a \cdot x$. To find the constant a, the definition of the spreading rate S is used :

$$S = \frac{U_c}{\Delta U}\frac{\mathrm{d}\delta}{\mathrm{d}x}.$$

A typical value for a mixing layer of $S = 0.085$ is selected [30]. Then, a is found to be equal to 0.076 by choosing $U_1 = 1.0$ and $U_2 = 0.38$, the velocity values that will be used for the simulation. Finally, the value of R_T, which can be seen as a turbulent Reynolds number, is chosen to be $R_T = 85$, which is again a typical value for a mixing layer.
By using equation (1.13), the turbulent stresses in equation (1.11) can thus be written as :

$$\begin{aligned} -\frac{\partial}{\partial y}\left(\overline{u'v'}\right) &= \frac{\partial}{\partial y}\left(\nu_t \frac{\partial \overline{u}}{\partial y}\right) \\ \text{with} \quad \nu_t &= U_1 \cdot x \cdot \frac{a}{R_T} \end{aligned} \tag{1.14}$$

Now, since the flow is incompressible, a streamfunction $\overline{\psi}$ is defined :

$$\begin{aligned} \overline{u} = \frac{\partial \overline{\psi}}{\partial y}\ , \quad \overline{v} &= -\frac{\partial \overline{\psi}}{\partial x} \\ \text{with} \quad \overline{\psi} &= U_1 \cdot x \cdot F(\eta) \end{aligned} \tag{1.15}$$

where $\eta = \frac{y}{x}$ is the similarity variable and F is a dimensionless function.
By combining equation (1.14) and equation (1.15), it can be shown that the *PDE* (1.11) is transformed into an *ODE* of the following form [10] :

$$\frac{a}{R_T}F''' + FF'' = 0 \tag{1.16}$$

The conditions $\overline{u}(\eta = 0) = U_c$ and $\overline{v}(\eta = 0) = 0$ give two of the three initial conditions required to solve equation (1.16) : $F(\eta = 0) = F'(\eta = 0) = 0$. The third one is unknown and the resolution of equation (1.16) is done by iterating on values of $F''(\eta = 0)$ until obtaining $\overline{u}(\eta >> 1) \to U_1$. The solution is plotted on figure 1.2.

[2]There are more elaborate closure RANS models. The best known is probably the two-equation $k - \epsilon$ model in which two additional transport equations for the turbulent kinectic energy and the dissipation rate are solved in order to express the turbulent viscosity.

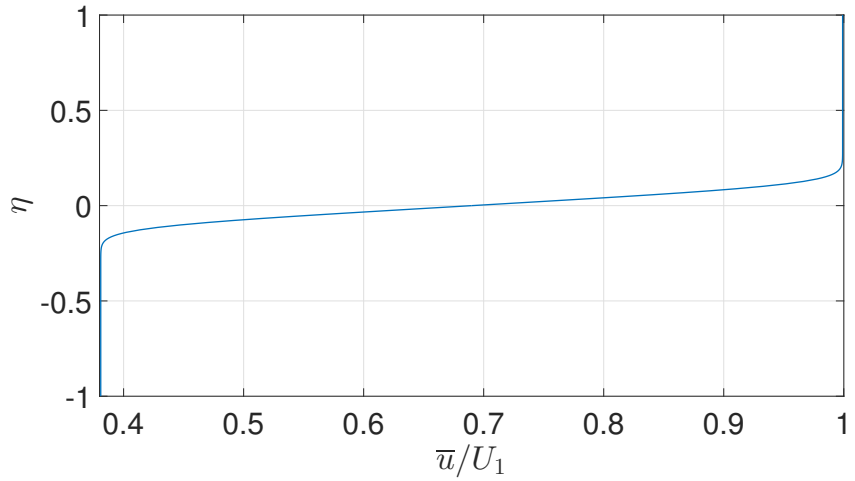

Figure 1.2: Velocity profile of the simplified Reynolds equations

Equation (1.16) is obviously not very accurate compared to the complete Navier-Stokes equations. The aim is simply to have an idea of the results that could be obtained by solving the complete equations. The resolution of the non-simplified equations uses sophisticated numerical techniques and obtaining a solution is never as easy as with the simplified approach that has just been described, as will be seen in the rest of this report.

1.5 Mixing layer parameters

1.5.1 Velocities

Four velocities will be used in this report. In the following, l is a length much greater than the shear layer thickness (see section 1.5.2).

- the high-speed free-stream velocity U_1

$$\overline{u}(x,y,z) \to U_1 \quad \text{as } y \to l \ ; \tag{1.17}$$

- the low-speed free-stream velocity U_2

$$\overline{u}(x,y,z) \to U_2 \quad \text{as } y \to -l \ ; \tag{1.18}$$

- the convection velocity

$$U_c = \frac{U_1 + U_2}{2} \ ; \tag{1.19}$$

- the velocity difference

$$\Delta U = U_1 - U_2 \ . \tag{1.20}$$

All these velocities are constant, independent of x.

1.5.2 Widths

To measure the growth of the mixing layer as function of the streamwise position, several characteristic widths are defined.

- the visual thickness

$$\begin{aligned} & \delta_{vis}(x) = y_{0.9}(x) - y_{0.1}(x) \ , \\ \text{with} \quad & y_{0.1}(x) \equiv \text{y position where } \overline{u} = U_2 + 0.1 \cdot \Delta U \ , \\ & y_{0.9}(x) \equiv \text{y position where } \overline{u} = U_2 + 0.9 \cdot \Delta U \ ; \end{aligned} \tag{1.21}$$

- the vorticity thickness

$$\delta_\omega(x) = \frac{\Delta U}{\left(\partial \overline{u}/\partial y\right)_{\max}} \; ; \tag{1.22}$$

- the momentum thickness

$$\theta(x) = \frac{1}{(\Delta U)^2} \int_{-l}^{l} (U_1 - \overline{u})\,(\overline{u} - U_2)\,\mathrm{d}y \; . \tag{1.23}$$

1.5.3 Dividing streamline

The dividing streamline divides the flow into two parts and is defined as the line across which the momentum flux is zero. The position $y^*(x)$ of the dividing streamline is obtained by resolving the following equation [10], [5] :

$$\int_{-l}^{y^*} \left[\overline{u}\,(\overline{u} - U_2) + \left(\overline{u'u'} - \overline{v'v'}\right)\right]\,\mathrm{d}y = \int_{y^*}^{l} \left[\overline{u}\,(U_1 - \overline{u}) - \left(\overline{u'u'} - \overline{v'v'}\right)\right]\,\mathrm{d}y \; . \tag{1.24}$$

1.5.4 Similarity variable

The scaled transverse variable used to make dimensionless graphs in chapter 4 is defined as

$$\eta = \frac{y}{x - x_0} \; , \tag{1.25}$$

where x_0 is the virtual origin of the turbulent mixing layer. The use of "$x - x_0$" at the denominator of the similarity variable is justified by the fact that all the thicknesses (see section 1.5.2) measured in the self-similarity region of the flow are defined to be equal to zero at the virtual origin. Note that the choice of this variable is arbitrary, but it must be chosen in such a way that the equations expressed with respect to η no longer depend on x and y.

1.5.5 Reynolds number

Different definitions of the Reynolds number are possible. For the rest of this report, the Reynolds number considered will be based on the initial vorticity thickness of the layer (see equation (1.22)), that is the vorticity thickness at the instant $t = 0$. Its definition is :

$$\mathrm{Re}_{\delta_{\omega_0}} = \frac{\Delta U \cdot \delta_{\omega_0}}{\nu} \; . \tag{1.26}$$

2 Numerical method

2.1 Introduction

Even though some practical situations can be studied experimentally (for example in wind tunnels with scale models), the numerical simulation of physical problems becomes inevitable for many situations for which experiments are too expensive or even impossible to realize. However, there are still complex flow problems requiring experimental facilities for their study. With the ever-increasing power of computers, the application fields of numerical simulations broaden more and more, which allow predicting physical problems taking place in real-life situations. It is in this context that CFD finds his place. Even if analytical solutions exist for simple cases where the Navier-Stokes equations can be simplified, in general no analytical solution is available. The complete non-linear partial differential equations are then resolved on computers using different techniques. Each of them is more or less appropriate to a given situation. In this dissertation, a state-of-the-art numerical method is employed and its operation will be explained in the following sections. Each section details an aspect of the numerical method and the relating pros and cons.

The simulation of fluid flows is far from being simple but turbulence introduces other difficulties. The velocity field is three-dimensional, unsteady and exhibits rapid fluctuations with time. There is also a large range of timescales and lengthscales that has to be taken into account when solving the equations. In one word, turbulence is "one of the principal unsolved problems in physics today" [13], which makes its simulation especially tricky. Simulating turbulent flows is a matter of compromises : a very high level of accuracy requires excessive computational resources while a lack of accuracy prevents the simulation results to be used to design real devices. In the present time, the best method with regard to these compromises is probably the Large Eddy Simulation (LES), that is implemented in the VPM solver.

2.2 Vorticity-velocity formulation

In fluid mechanics and especially in turbulence, the vorticity vector, denoted by $\boldsymbol{\omega}$, is an extremely used quantity. By definition, it is the curl of the velocity vector $\mathbf{v}$:

$$\begin{aligned}\boldsymbol{\omega} &= \boldsymbol{\nabla} \times \mathbf{v} \\ &= \left(\frac{\partial w}{\partial y} - \frac{\partial v}{\partial z}, \frac{\partial u}{\partial z} - \frac{\partial w}{\partial x}, \frac{\partial v}{\partial x} - \frac{\partial u}{\partial y}\right).\end{aligned} \tag{2.1}$$

It represents the rate of rotation of a fluid particle (more precisely, twice that rate) that rotates around its center without deformation. The Navier-Stokes equations (1.5) under their classical velocity-pressure formulation can be converted into their vorticity-velocity formulation. First, the two following identities are used to modify the convective and diffusive terms of equation (1.5) :

$$\boldsymbol{\nabla}^2\mathbf{v} = \boldsymbol{\nabla} \cdot (\boldsymbol{\nabla}\mathbf{v}) = \boldsymbol{\nabla}(\underbrace{\boldsymbol{\nabla} \cdot \mathbf{v}}_{=0}) - \boldsymbol{\nabla} \times (\underbrace{\boldsymbol{\nabla} \times v}_{=\boldsymbol{\omega}}) = -\boldsymbol{\nabla} \times \boldsymbol{\omega} \ ,$$

$$(\boldsymbol{\nabla}\mathbf{v}) \cdot \mathbf{v} = \boldsymbol{\nabla}(\underbrace{\frac{\mathbf{v} \cdot \mathbf{v}}{2}}_{=K}) + (\underbrace{\boldsymbol{\nabla} \times v}_{=\boldsymbol{\omega}}) \times \mathbf{v}.$$

Then, by taking the curl of the modified equation and by using the identities below

$$\boldsymbol{\nabla} \times \boldsymbol{\nabla}(\bullet) = 0 \ ,$$

$$\boldsymbol{\nabla} \times (\boldsymbol{\nabla} \times \boldsymbol{\omega}) = \boldsymbol{\nabla}(\underbrace{\boldsymbol{\nabla} \cdot \boldsymbol{\omega}}_{=0}) - \boldsymbol{\nabla}^2 \boldsymbol{\omega} = -\boldsymbol{\nabla}^2 \boldsymbol{\omega} \ ,$$

$$\boldsymbol{\nabla} \times (\boldsymbol{\omega} \times \mathbf{v}) = -\mathbf{v}(\underbrace{\boldsymbol{\nabla} \cdot \boldsymbol{\omega}}_{=0}) + (\mathbf{v} \cdot \boldsymbol{\nabla})\boldsymbol{\omega} + \boldsymbol{\omega}(\underbrace{\boldsymbol{\nabla} \cdot \mathbf{v}}_{=0}) - (\boldsymbol{\omega} \cdot \boldsymbol{\nabla})\mathbf{v} \ ,$$

the velocity-vorticity formulation of the Navier-Stokes equations is obtained :

$$\frac{D\boldsymbol{\omega}}{Dt} = \frac{\partial \boldsymbol{\omega}}{\partial t} + (\boldsymbol{\nabla}\boldsymbol{\omega}) \cdot \mathbf{v} = (\boldsymbol{\nabla}\mathbf{v}) \cdot \boldsymbol{\omega} + \nu \boldsymbol{\nabla}^2 \boldsymbol{\omega}. \tag{2.2}$$

It remains a convection-diffusion equation (for the vorticity and no more for the velocity) with the pressure source term replaced by the first term on the right-hand side. This term, which is only present in three dimensions, represents the vortex stretching and vortex tilting phenomena. It is through these phenomena that vorticity and velocity gradient interact to create vorticity in three dimensions [19]. This process repeats until the vorticity and velocity fields become chaotic : turbulence is then created. Turbulence is also maintained by these processes.
The velocity field is related to the vorticity field through a Poisson equation :

$$\boldsymbol{\nabla}^2 \mathbf{v} = -\boldsymbol{\nabla} \times \boldsymbol{\omega}. \tag{2.3}$$

In practice, the velocity is obtained from the streamfunction $\boldsymbol{\psi}$:

$$\mathbf{v} = \boldsymbol{\nabla} \times \boldsymbol{\psi} + U_\infty \tag{2.4}$$

with $\boldsymbol{\nabla} \cdot \boldsymbol{\psi} = 0$ and U_∞ the freestream velocity. $\boldsymbol{\psi}$ is computed via another Poisson equation :

$$\boldsymbol{\nabla}^2 \boldsymbol{\psi} = -\boldsymbol{\omega} \tag{2.5}$$

On the one hand, the advantages of this formulation are :

- the resolution of the N-S equations under this form in a non-inertial frame does not require to add other terms (centrifugal acceleration, Coriolis acceleration, etc.). The non-inertial effects are taken into account in the initial boundary conditions [6] ;
- for external flows, the freestream boundary conditions are easier to impose on the vorticity than on the pressure ;
- the vector $\boldsymbol{\omega}$, which is very important in turbulent flows, is directly available ;
- the continuity equation is automatically satisfied. There is no need to enforce incompressibility through the Poisson equation for the pressure as it is the case in the other formulation ;
- for flows with low viscous diffusion, the fluid volume with a significant vorticity intensity is only a small fraction of the total volume. Vorticity then has a much smaller support compared to velocity, which is interesting from a computational point of view.

On the other hand, the disadvantages of this approach are :

- for a three-dimensional flow, there are six equations to solve instead of four for the primitive formulation ;
- the solenoidal property of vorticity and velocity vectors has to be ensured ;
- «LES using the $\mathbf{v} - \boldsymbol{\omega}$ formulation are not very popular and the corresponding literature remains relatively scarce» [3].

2.3 Vortex method

Vortex methods belong to the class of Lagrangian methods in which particles, instead of a fixed mesh, are used to simulate «unsteady convection-dominated problems» [12]. In vortex methods, the vorticity field $\boldsymbol{\omega}$ is discretized using particles. Each particle p occupies a material volume $V_p(t)$ carried by the local velocity field. The Navier-Stokes equations (2.2) can then be integrated over those material volumes to give :

$$\int_{V_p(t)} \frac{D\boldsymbol{\omega}}{Dt} \, \mathrm{d}\mathbf{x} = \int_{V_p(t)} (\boldsymbol{\nabla}\mathbf{v}) \cdot \boldsymbol{\omega} + \nu \boldsymbol{\nabla}^2 \boldsymbol{\omega} \, \mathrm{d}\mathbf{x}. \tag{2.6}$$

By Reynolds Transport Theorem, the left-hand side term becomes :

$$\int_{V_p(t)} \frac{D\boldsymbol{\omega}}{Dt} \, \mathrm{d}\mathbf{x} = \frac{d}{dt} \int_{V_p(t)} \boldsymbol{\omega} \, \mathrm{d}\mathbf{x}.$$

The Lagrangian approach is thus different from the Eulerian approach : in the first one, the conservation equations apply to a material volume moving with the flow while in the second one, these same equations are for a fixed control volume through which the flow travels.
By definition, the strength of a particle p is expressed as

$$\alpha_p(t) \triangleq \int_{V_p(t)} \boldsymbol{\omega} \, \mathrm{d}\mathbf{x} \triangleq \boldsymbol{\omega}_p V_p \ .$$

Moreover, for an incompressible flow, $\frac{d}{dt} V_p(t) = 0$.
To consider the conservation equations applied to each particle, their positions, denoted by $\mathbf{x}_p$, have to be known and are simply given by :

$$\frac{d\mathbf{x}_p}{dt} = \mathbf{v}_p \ ,$$

where $\mathbf{v}_p = \mathbf{v}(\mathbf{x}_p(t), t)$ is the velocity of the particle p.
The set of ordinary differential equations associated with vortex methods writes then :

$$\begin{cases} \frac{d\mathbf{x}_p}{dt} = \mathbf{v}_p \\ \frac{d\boldsymbol{\omega}_p}{dt} = (\boldsymbol{\nabla}\mathbf{v})_p \cdot \boldsymbol{\omega}_p + \nu(\boldsymbol{\nabla}^2\boldsymbol{\omega})_p \end{cases} \tag{2.7}$$

To predict the evolution of a flow, one thus needs to recover the velocity field from the vorticity field in order to update the particle positions and compute the stretching term, to evaluate the Laplacian of the vorticity and to advance in time the 2 vectorial equations. Recovering $\mathbf{v}(\mathbf{x}_p(t), t)$ and $\boldsymbol{\nabla}^2\boldsymbol{\omega}(\mathbf{x}_p(t), t)$ from $\boldsymbol{\omega}(\mathbf{x}_p(t), t)$ is the main challenge in vortex particle methods [24].

From these considerations, the pros and cons of this method can be listed below. The advantages are :

- the non-linear inertia term is no more present in equation (2.7) since the flow description is Lagrangian. The classical CFL constraint of mesh-based methods

  $$\frac{\Delta t \, \|\mathbf{v}\|}{h} < \mathcal{O}(1)$$

  is thus relaxed. This feature enables the use of time steps that are bigger than for an Eulerian description. Two conditions on the time step (which do not involve the mesh resolution) must however be satisfied :

  $$\Delta t \, \|\boldsymbol{\nabla}\mathbf{v}\| < \mathcal{O}(1) \ ,$$

$$\Delta t \, \|\boldsymbol{\omega}\| < \mathcal{O}(1).$$

Those conditions ensure that the local strain and the rotation of particles with respect to each other will not lead to collisions between particles [24].
In convection diffusion equation, there is also a stability constraint related to the viscous term. This term is still present in the equations (unlike the advective term) and it introduces an additional stability constraint :

$$\frac{\Delta t \nu}{h^2} < \mathcal{O}(1) \ ;$$

- it has negligible dispersion errors ;
- since particles represent the vorticity field, they are often only needed on small sets in the computational domain.

The disadvantages of vortex methods are :

- the set of particles needs to be frequently reinitialized in order to prevent clustering and depletion of particles in some regions of the domain due to local velocity gradients, which could lead to a less accurate representation of the vorticity field ;
- to compute the differential operators in the right-hand side of equation (2.7) , a costly neighbour-finding loop has to be used [28]. With mesh-based methods, those differentiations can be more efficiently performed ;
- the evaluation of the velocity field becomes too expensive when the number of particles N grows very large. The use of fast summation algorithms to compute the Biot-Savart solution of equation (2.3) leads to a complexity in $\mathcal{O}(N \cdot logN)$, reduced compared to the $\mathcal{O}(N^2)$ complexity of direct summation but not enough to treat problems with huge amount of particles ;
- the simulation of near-wall flows requires a lot of particles in the boundary-layer. Indeed, in the boundary layer, the flow is anisotropic while the particles provide an isotropic representation of the field considered [21].

2.4 Vortex particle-mesh method

The vortex particle-mesh (VPM) methods, also called vortex-in-cell (VIC), combine particles and an underlying grid to solve the flow. The main interest of the grid is to use the available efficient grid-based Poisson solvers to compute the velocity and to compensate for the third drawback of grid-free methods (see section 2.3). This operation is of prime importance as it is the most expensive computational step of the method.
The mesh also has other usages :

- in response to the second drawback of vortex methods, the spatial differential operators are evaluated on the grid with finite differences ;
- when the distorded particles need to be reinitialized (or remeshed in this case), the grid is used to replace the old particles with new ones placed at the node positions of the grid ;
- the enforcement of the solenoidal character of the vorticity field (second drawback of $\mathbf{v} - \boldsymbol{\omega}$ formulation) is done by exploiting the available grid-based Poisson solver in Fourier space.

For that hybrid Lagrangian-Eulerian method to be applicable, the particles and the mesh need to communicate. It is realized by high order interpolation schemes.

In short, the mesh handles the computations of the right-hand side of the equation (2.7) and of the velocity field from the vorticity field interpolated on the mesh. Then, those quantities are interpolated back onto particles that are used for the advection of the vorticity field. Those operations are repeated in order to advance the problem in time. A detailed algorithm of the method is presented in section 3.5.

By examining the characteristics of the VPM method, one realizes that it is optimal to simulate a mixing layer flow :

- initially, the mixing layer is just a thin slab of vorticity in the domain (see section 3.3) and particles are only used in this region. When it grows, the vorticity still occupies a small fraction of the domain ;
- it is a free flow without solid boundaries for which particle methods are not optimal ;
- boundary conditions are imposed on $\boldsymbol{\omega}$ and $\mathbf{v}$ and not on the pressure, which is easier for external flows.

The solver used to produce the simulations for this thesis relies on the vortex-particle mesh method. It is a *Fortran* code that continues to be developed at UCL. It uses the open source Parallel Particles Mesh (PPM) library that provides the functions for the interaction between the mesh and the particles, the FFT-based Poisson solver as well as the definition of topologies, i.e. space decomposition and the assignment of sub-domains to processors [26]. The code uses the Message Passing Interface (MPI) to realize fast parallel computations on several processors.

2.5 Large eddy simulation

The direct resolution of the Navier-Stokes equations for a turbulent flow (DNS) is far too expensive in most of the situations. Indeed, turbulence is characterized by a large range of different scales and resolving exactly the smallest scales requires an extremely fine discretization. That is why turbulence models were developed.

In section 1.4.2, the RANS equations governing the mean flow quantities were derived. The quantities in those equations are time-averaged and the resulting turbulence stresses are modeled. By doing this, all the turbulent scales, from the largest eddies to the smallest ones, are modeled. In Large Eddy Simulation (LES), the quantities are filtered (it is a volume average) so that only the effects of the smaller-scale motions are modeled. The larger turbulent motions are resolved. This makes LES a more accurate method than RANS (but also more expensive).

The general space filtering operation on a vector $\boldsymbol{\phi}$ is defined as follows :

$$\boldsymbol{\phi} = \widetilde{\boldsymbol{\phi}} + \boldsymbol{\phi}'$$

$$\widetilde{\boldsymbol{\phi}} = \int_{\Omega} \mathbf{G}(\mathbf{r}) \cdot \boldsymbol{\phi}(\mathbf{x} - \mathbf{r}, t) \, \mathrm{d}\mathbf{r}$$

where Ω represents the entire flow domain and $\mathbf{G}$ is the normalized homogeneous filter function such that $\int_{\Omega} \mathbf{G}(\mathbf{r}) \, \mathrm{d}\mathbf{r} = 1$. Note that the filtered vector $\widetilde{\boldsymbol{\phi}}$ is capped with a wave to make the distinction with the time-average of section 1.4.2.
The simplest filter is the box filter, which is defined in one dimension as [19] :

$$G(r) = \begin{cases} \frac{1}{\Delta} & \text{if} \quad r \leq \frac{\Delta}{2} \\ 0 & \text{if} \quad r > \frac{\Delta}{2} \end{cases} \tag{2.8}$$

where Δ is the filter width which is often equal to the grid resolution h. In three dimensions, $\Delta = (\Delta_x \Delta_y \Delta_z)^{1/3}$ and the box filter is equivalent to a volume average over the sphere of radius $\frac{1}{2}\Delta$. Let us note that the filtering operation equation (2.8) is generally not explicitly performed, as it is the case for RANS methods in which the mean temporal operator is not explicitly performed. It is usually achieved directly through the spatial discretization of the domain.
It is convenient to study the filtering process in the spectral space. The box filter function in this space becomes :

$$\hat{G}(\kappa) = \begin{cases} \frac{1}{\Delta} & \text{if} \quad \kappa \leq \kappa_c \\ 0 & \text{otherwise} \end{cases} \tag{2.9}$$

where κ is the wavenumber and $\kappa_c = \frac{\pi}{\Delta}$ is the cut-off wavenumber. κ_c is supposed to lie in the inertial subrange of the turbulent kinetic energy spectrum in which the energy coming from the largest eddies is transferred to the dissipation range where the turbulent kinetic energy is dissipated under thermal energy by the smallest isotropic eddies.

In the same way as for the RANS equation (1.8), the filtering operation introduces an additional term in equation (1.5) :

$$\begin{aligned} \boldsymbol{\nabla} \cdot \widetilde{\mathbf{v}} &= 0, \\ \frac{\partial \widetilde{\mathbf{v}}}{\partial t} + \widetilde{\mathbf{v}} \cdot \boldsymbol{\nabla} \widetilde{\mathbf{v}} &= -\boldsymbol{\nabla} \widetilde{\mathrm{P}} + \nu \boldsymbol{\nabla}^2 \widetilde{\mathbf{v}} + \boldsymbol{\nabla} \cdot \boldsymbol{\tau}^M. \end{aligned} \tag{2.10}$$

where the subgrid stresses are given by

$$\tau_{ij}^M = -\left(\widetilde{u_i u_j} - \widetilde{u}_i \widetilde{u_j}\right).$$

The isotropic part of τ_{ij}^M is included in the modified filtered pressure while the deviatoric part needs to be modeled. From the spectral viewpoint described earlier, it is evident that this model needs to dissipate energy since it represents the smallest scales of turbulent motions. The simplest model is the eddy-viscosity model coupled with the Smagorinsky model :

$$\begin{aligned} \tau_{ij}^{M,dev} &= \tau_{ij}^M - \frac{1}{3}\tau_{ii}^M \delta_{ij}, \\ &= 2\nu_{sgs}\widetilde{d_{ij}}, \\ \text{with} \quad \nu_{sgs} &= (C_s \Delta)^2 \left(2\widetilde{d_{ij}}\widetilde{d_{ij}}\right)^{1/2} . \end{aligned} \tag{2.11}$$

If one considers instead the vorticity-velocity formulation, the filtered equations write :

$$\frac{\partial \widetilde{\boldsymbol{\omega}}}{\partial t} + \widetilde{\mathbf{v}} \cdot (\boldsymbol{\nabla} \widetilde{\boldsymbol{\omega}}) = (\boldsymbol{\nabla} \widetilde{\mathbf{v}}) \cdot \widetilde{\boldsymbol{\omega}} + \nu \boldsymbol{\nabla}^2 \widetilde{\boldsymbol{\omega}} + \boldsymbol{\nabla} \cdot \mathbf{T}^M. \tag{2.12}$$

where the deviatoric part of the subgrid scale tensor $\mathbf{T}^{M,dev}$ is modeled as [18] :

$$T_{ij}^{M,dev} = \nu_{sgs} \underbrace{\left(\frac{\partial \widetilde{\omega_i}}{\partial x_j} + \frac{\partial \widetilde{\omega_j}}{\partial x_i}\right)}_{\triangleq 2\widetilde{q_{ij}}} \tag{2.13}$$

A striking advantage of LES over some RANS models is that the subgrid scale model is not flow specific. Indeed, from a statistical point of view, turbulence at the smallest scales is assumed to be universal, which means independent of the flow configuration.
The drawback of the model just described is that it dissipates too much energy at the largest scales. The idea to improve the model is to confine the dissipation of the subgrid scale model to the smallest scales of the flow. The subgrid stresses are then computed from the small scales (denoted by a superscript "s") and no more from the entire range of scales :

$$\tau_{ij}^{M,dev} = 2\nu_{sgs}\widetilde{d_{ij}^s} \ ,$$

$$T_{ij}^{M,dev} = 2\nu_{sgs}\widetilde{q_{ij}^{s}}.$$

To do that, the filtered velocity field (or vorticity field) is decomposed into two parts :

$$\widetilde{u_i} = \widetilde{u_i}^L + \widetilde{u_i}^s \ ,$$

where the large scale field $\widetilde{u_i}^L$ is obtained via the application of a low pass filter. The methods based on this approach are called Regularized Variational Multiscale (RVM) methods. In the VPM code, one of these methods is implemented.

2.6 Time integration

The spatial discretization used in the code having been explained in the previous sections, the time integration scheme to resolve the set of ODE's (2.7) is briefly developed here. A low storage third order Runge-Kutta scheme from [16] is implemented. It is divided in three substeps [21] :

$$\frac{\mathrm{d}U}{\mathrm{d}t} = F(U,t)$$

Substep 1 : from t^n to $t^{n+\frac{1}{3}} = t^n + \frac{1}{3}\Delta t$

$$U^* = F(U^n, t^n)$$
$$U^{n+\frac{1}{3}} = U^n + \frac{1}{3}\Delta t U^*$$

Substep 2 : from $t^{n+\frac{1}{3}}$ to $t^{n+\frac{3}{4}} = t^n + \frac{3}{4}\Delta t$

$$U^* = F(U^{n+\frac{1}{3}}, t^{n+\frac{1}{3}}) - \frac{5}{9}U^*$$
$$U^{n+\frac{3}{4}} = U^{n+\frac{1}{3}} + \frac{15}{16}\Delta t U^*$$

Substep 3 : from $t^{n+\frac{3}{4}}$ to $t^{n+1} = t^n + \Delta t$

$$U^* = F(U^{n+\frac{3}{4}}, t^{n+\frac{3}{4}}) - \frac{153}{128}U^*$$
$$U^n = U^{n+\frac{3}{4}} + \frac{8}{15}\Delta t U^*$$

3 Numerical simulation of a turbulent mixing layer

3.1 Introduction

In the previous chapter, the theory on which the VPM solver is based has been described. Having this powerful solver at its disposal is a chance. In order to use it correctly and simulate the mixing layer flow, the choice of the initial and boundary conditions, which constitutes a recurrent step in *CFD*, has to be judicious. That is why the three first sections of this chapter are devoted to the explanations about boundary, initial and inflow conditions. Then, the next section explains how these conditions were implemented in VPM on the basis of a detailed algorithm of the code. Finally, the last crucial step before running a simulation, which is the choice of the parameters, is treated.

3.2 Boundary conditions

On the basis of figure 1.1 , the boundary conditions (B.C.) for the computational domain are defined as :

1. *periodic* B.C. in the spanwise direction : in experiments, the spanwise length is sufficiently large so that the flow is nearly statistically two-dimensional. Moreover, the initial slab of vorticity cannot be cut at its edges (Helmholtz's second theorem) and a periodic B.C. is therefore required in this direction ;

2. *unbounded* transverse direction : as in the experiments, the flow must not be influenced by any upper or lower boundaries as it is a free flow and this kind of B.C. is thus needed ;

3. streamwise direction :

   - inflow : $\frac{\partial u}{\partial x} = v = w = 0 \Leftrightarrow \omega_x = \frac{\partial \omega_y}{\partial x} = \frac{\partial \omega_z}{\partial x} = 0$,
   - outflow : $\frac{\partial u}{\partial x} = v = w = 0 \Leftrightarrow \omega_x = \frac{\partial \omega_y}{\partial x} = \frac{\partial \omega_z}{\partial x} = 0$,

   The streamwise vorticity as well as the spanwise and transverse velocities at the inflow and outflow are thus eliminated.

In the code, it is an "outflow-outflow" condition with a "zero-lift" outlet type. Note that the choice of an "inflow-outflow" condition would have imposed $u = U_\infty$ at the inflow (and $\frac{\partial v}{\partial x} = \frac{\partial w}{\partial x} = 0$). The particles would have entered the domain at the same velocity, which is in disagreement with the imposed initial velocity profile.
In practice, the imposition of those B.C. in the code is done in the following way :

1. the positions of the particles that exited the domain from the left or right side along the periodic direction are reinserted in the domain at the opposite side where they exited ;

2. VPM uses a dynamic resizing in the unbounded direction. If particles with a vorticity intensity different from zero are too close to the upper or lower side, the domain grows such that particles of null intensity are always adjacent to the transverse boundaries. In fact, those particles are not involved in the computation. The underlying grid used to compute the velocity occupies the entire domain and is also present where particles are not. The Poisson solver imposes $u = U_\infty$ for $y \to \pm\infty$ by doubling the size of the domain in the transverse direction and by padding the extension with zeros [25] ;

3. the inflow and outflow conditions correspond to a restriction of the Fourier modes to be considered in the resolution of the Helmholtz equation in the unbounded direction after Fourier transforms along the spanwise and streamwise directions have been performed [28]. In the Fourier space, the velocity can be written as follows :

$$u = \sum_i \left(A\cos(k_i x) + B\sin(k_i x)\right) .$$

The imposition of $\frac{\partial u}{\partial x} = 0$ at the inflow and outflow yields :

$$u = \sum_i A_i \cos\left(\frac{2\pi i}{2L_x}\right) ,$$

$$\omega_x = \sum_i B_i \sin\left(\frac{2\pi i}{2L_x}\right) .$$

The same reasoning applies for the other components of the velocity and vorticity fields. The allowed modes thus have a period $2 \cdot L_x$ and this restriction is made through the use of Discrete Sine and Cosine transforms (DCT and DST). It corresponds to make an axial symmetry of the domain with respect to the inflow and outflow planes respectively, and to impose periodic boundary conditions at the extremities of this new fictive domain.

3.3 Initial conditions

In section 1.4.3, the solution of the simplified Reynolds equations provides a velocity profile going smoothly from U_2 to U_1 (figure 1.2). It is then suitable to express the initial mean streamwise velocity profile with a hyperbolic tangent function :

$$u_{init}(y) = U_c + \frac{\Delta U}{2}\tanh\left(\frac{2y}{\delta_{\omega_0}}\right) , \tag{3.1}$$

where δ_{ω_0} is the initial vorticity thickness. Linear stability theory can be applied on this profile to find the streamwise and spanwise wavelengths λ_x and λ_z leading to the fastest development of the Kelvin-Helmholtz instabilities. They are found to be approximately equal to :

$$\lambda_x = 14.0 \cdot \delta_{\omega_0} , \quad \lambda_z = 0.6 \cdot \lambda_x . \tag{3.2}$$

These values will be used to perturb the initial condition (see section below). A brief explanation of the linear stability theory can be consulted in appendix A.
Since the other components of the velocity field are zero, the corresponding initial vorticity field is :

$$\boldsymbol{\omega}_{init}(y) = (\omega_x,\ \omega_y,\ \omega_z) = \left(0,\ 0,\ -\frac{\Delta U}{\delta_{\omega_0}}\frac{1}{\cosh^2\left(\frac{2y}{\delta_{\omega_0}}\right)}\right) . \tag{3.3}$$

In the code, the domain is initially filled with this vorticity slab and the desired velocity profile is obtained via Biot-Savart. The initial velocity and vorticity profiles are plotted on figures 3.1 and 3.2, respectively. A 3-D view of the velocity is also represented on figure 3.3 to show the

"extrusion" of the 2-D profile along the spanwise direction.

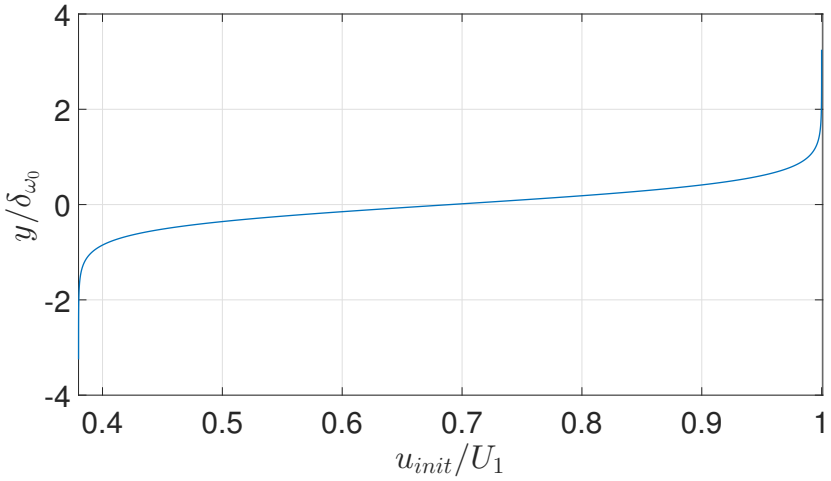

Figure 3.1: Initial velocity profile

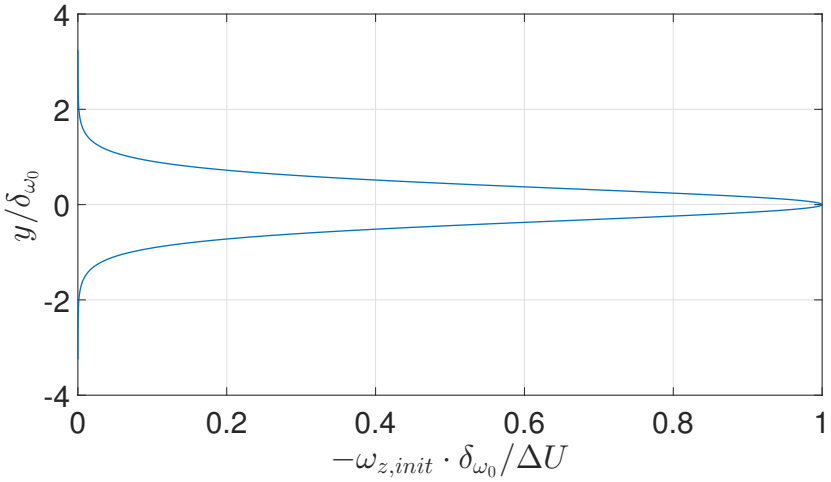

Figure 3.2: Initial vorticity profile

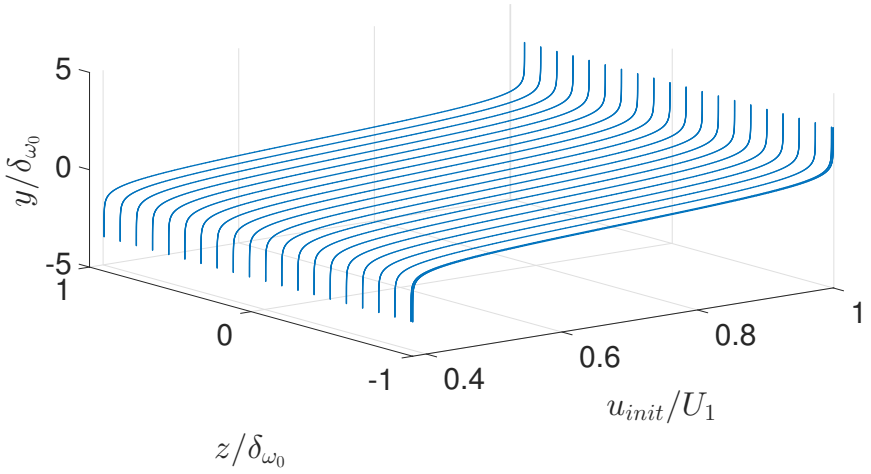

Figure 3.3: Initial velocity profile in three dimensions

Instead of the Gaussian slab of vorticity, an interesting case to consider is a two dimensional singular vortex sheet with a uniform circulation per unit length γ. In that case, the velocities above and under the sheet correspond to the theoretical velocity profile of a mixing layer represented in figure 1.1 :

$$U_1 = U_\infty + \frac{\gamma}{2} \ ,$$

$$U_2 = U_\infty - \frac{\gamma}{2} \ .$$

Some perturbations are added to $\boldsymbol{\omega}_{init}$ in order to accelerate the development of the large-scale turbulent structures. Those perturbations, denoted by a "*" superscript, are inspired by the ones presented in [23] :

$$\begin{aligned} \omega_x^*(x,y,z) &= A_{pert} \cdot e^{-\pi y^2} \cdot \sin\left(\frac{2\pi z}{\lambda_z}\right) \ , \\ \omega_z^*(x,y,z) &= A_{pert} \cdot e^{-\pi y^2} \cdot \left[\cos\left(\frac{2\pi x}{\lambda_x}\right) + \cos\left(\frac{\pi x}{\lambda_x}\right) + \cos\left(\frac{\pi x}{2\lambda_x}\right)\right] . \end{aligned} \tag{3.4}$$

In equation (3.4), the exponential factor allows the perturbations to be more intense in the center of the vorticity slab. The perturbations on the streamwise vorticity component involve the fundamental unstable mode with wavelength λ_z, while the spanwise perturbations involve the 3 first unstable modes of the initial velocity profile according to linear stability theory (see appendix A). The amplitude A_{pert} is chosen so that it corresponds to 5% of the maximal value of the initial vorticity profile. The introduction of ω_z^* favors the formation of coherent spanwise structures while ω_x^* introduces three-dimensional effects to accelerate the transition to the turbulent state. Near the inflow, the perturbations are smoothly set to zero because the particles in the buffer are not submitted to those perturbations (see section 3.4). Moreover, they are corrected so that they are solenoidal in order to "help" the reprojection of $\boldsymbol{\omega}$ after few time steps. To do that, one writes :

$$\begin{aligned} \omega_x^{*,corrected}(x,y,z) &= \omega_x^*(x,y,z) \cdot f(x) \ , \\ \omega_z^{*,corrected}(x,y,z) &= \omega_z^*(x,y,z) \cdot f(x) \cdot g(z) \ , \end{aligned} \tag{3.5}$$

with $f(x)$ a Gaussian function smoothly setting the perturbations to zero and $g(z)$ the "corrector function" such that :

$$\frac{\partial \omega_x^{*,corrected}}{\partial x} + \frac{\partial \omega_z^{*,corrected}}{\partial z} = 0.$$

The initial vorticity field in the domain is therefore given by :

$$\boldsymbol{\omega}_{init} = \begin{cases} \boldsymbol{\omega}_{init} + \boldsymbol{\omega}^{*,corrected} & \text{near the inflow,} \\ \boldsymbol{\omega}_{init} + \boldsymbol{\omega}^{*} & \text{otherwise.} \end{cases} \tag{3.6}$$

The streamwise and spanwise components of the initial vorticity field are presented in figure 3.4. The perturbations added to the initial vorticity are clearly visible. It is important to note that the domain on this figure is half as long as the domain actually used in the simulation.

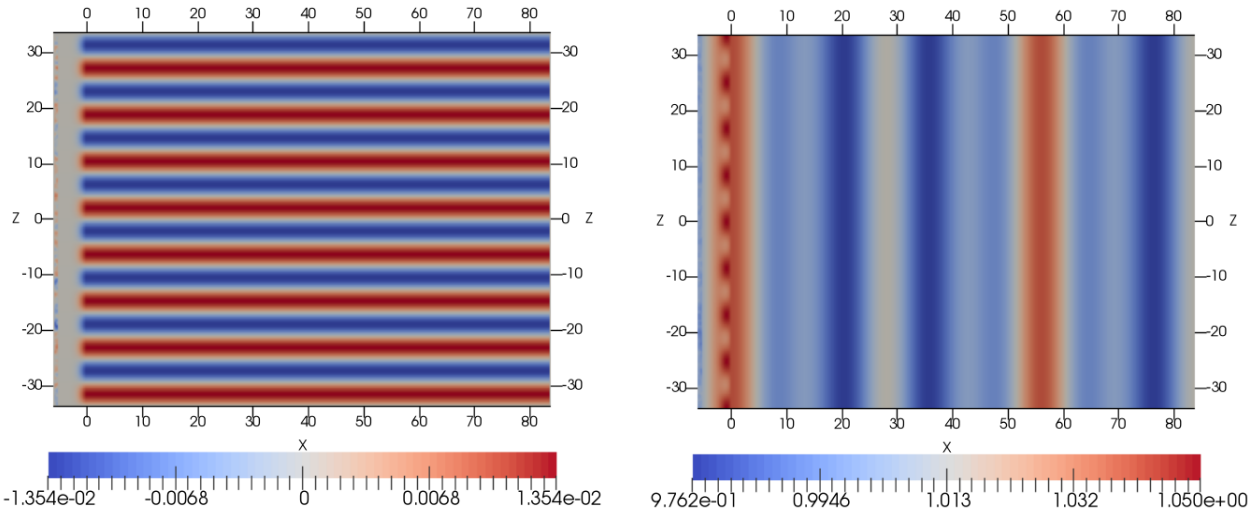

(a) $\omega_{x,init}/\omega_{init,max}$ (b) $\omega_{z,init}/\omega_{init,max}$

Figure 3.4: Transverse slice in the middle of the domain of the initial condition showing the effects of the perturbations.

3.4 Incoming flow

The insertion of an incoming flow in the computational domain is made through a buffer region that overlaps a small fraction of the domain. In the buffer, the particles are advected in the same way as in the domain except that the velocity does not result of the resolution of the Poisson equation but is set to the value of U_∞ in the portion of the buffer that does not overlap the domain. In the overlapping region, the particles in the buffer are progressively inserted in the domain with a blending function. The buffer is fed with particles with a precomputed database. Each time a row of particles advances in the buffer, a new one from the database is inserted at the beginning of the buffer.

3.4.1 Database

With the same idea as with the initial condition, the incoming flow is perturbed in order to accelerate the development of the mixing layer. First, the Mann algorithm [15] is used to generate a turbulent velocity field in a box. It is a homogeneous isotropic turbulence with the following characteristics :

- The turbulence intensity TI is defined as :

$$TI = \frac{u'_{rms}}{U_c} \ ,$$

  where $u'_{rms} = \sqrt{\frac{1}{3}(u'^2 + v'^2 + w'^2)}$ is the root-mean-square of the turbulent velocity fluctuations. The selected value is

$$TI = 0.25\% \ ,$$

  which is a typical value of wind tunnel experiments [20]. This value should not be too large, as it may cause the mixing layer to be much too perturbed ;

- the integral lengthscale L_{int}, which represents the length on which turbulent quantities are correlated, is chosen to be equal to the fundamental wavelength of the Kelvin-Helmholtz instability :

$$L_{int} = \lambda_x.$$

Once the turbulent velocity field is obtained with this algorithm, the vorticity field is computed and clipped along its edges in the unbounded direction. This turbulent vorticity field, denoted by $\widetilde{\boldsymbol{\omega}}$, is then read by the code to feed the buffer with particles. This field is presented on figure 3.5. Its intensity ranges from approximately $-6 \cdot 10^{-3}$ to $6 \cdot 10^{-3}$.

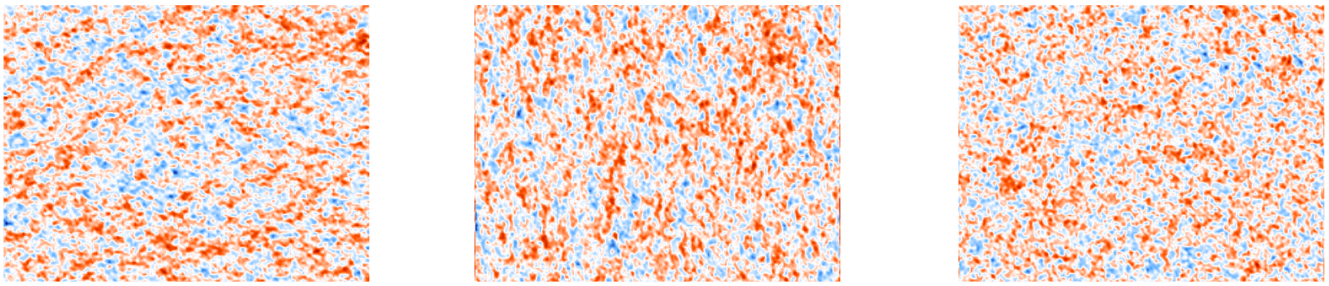

(a) $\widetilde{\omega_x}$ (b) $\widetilde{\omega_y}$ (c) $\widetilde{\omega_z}$

Figure 3.5: Spanwise slice of the turbulent vorticity field used to perturb the incoming flow

3.4.2 Buffer

In order to let the desired velocity profile enter the domain, the same Gaussian vorticity profile as for the initial condition (equation (3.3)) is imposed analytically in the buffer. Furthermore, the turbulent vorticity of the database is superposed to the analytical profile such that the incoming vorticity is perturbed. Hence the incoming vorticity can be expressed as :

$$\boldsymbol{\omega}_{inflow} = \boldsymbol{\omega}_{init} + \widetilde{\boldsymbol{\omega}}. \tag{3.7}$$

The perturbations are thus precomputed before the simulation and are added to the vorticity in the buffer. These operations are situated in the global algorithm of the code in section 3.5.

Before opting for this solution, other alternatives that do not involve the database have been tested to perturb the incoming flow :

- a white noise was generated at each time step in the buffer and was added to the vorticity field. Even if the sum of those perturbations was zero, there was no way to make this noise solenoidal since the FFT-based functions are not available in the buffer ;
- to solve the problem of the first alternative, the white noise was added to the vorticity field in a small region of the computational domain, just after the end of the buffer. However, the implementation of the white noise generator was not adapted to be called at each time step and it slowed the program. A figure obtained with this approach is presented in appendix C.

Let us remark that the hyperbolic tangent velocity profile for the incoming flow is not the one that will provide results closest to the experimental results. Indeed, in experiments, a splitter plate is used to separate the two incoming flows. In this case, the velocity profile at the inflow has a small wake-deficit caused by the boundary layers of the flows above and under the plate before the inflow. This profile is known to be more unstable that the "tanh" profile used for this simulation, and the transition to turbulence occurs faster [35]. Such an inflow condition can be implemented either by pre-computing two turbulent boundary layer flows and by extracting their mean velocity profiles in order to use them as inflow conditions, or simply by considering two laminar Blasius boundary layers as in [35].

Note finally that the simulation could have been carried out without the addition of any perturbations. In this case, the flow would have remained longer two-dimensional with the features of a two-dimensional mixing layer before transitioning to the turbulent state. However, it would have required a domain with too large dimensions in order to correctly study the fully turbulent region. The aim of this thesis being not to study the laminar and transition regions, perturbations were included in the incoming flow and in the initial condition to accelerate the transition to the fully-turbulent state.

3.5 Code overview and modifications

In order to impose the analytical vorticity profile at the right place in the thousands of lines of code, an overview of the VPM code was necessary. That is why an algorithm containing the main steps of the code when resolving a turbulent mixing layer is presented on page 26. For the sake of simplicity and readability, the time integration scheme is here simplified and it involves only one step. The real scheme was presented in section 2.6. In this algorithm, the subscripts "p" and "ij" designate a field on the particles or on the mesh, respectively. When the subscript "TIB" is also present, it represents a field in the Turbulent Inflow Buffer (TIB). The superscipt "n" states the field at time $t = t^n$. The acronyms "P2M" and "M2P" mean "Particles-to-Mesh" and "Mesh-to-Particles" interpolations. Finally, the **Rhs** term designates the right-hand side term of equation (2.7).
The changes to the program allowing the simulation of the mixing layer are highlighted in blue in the algorithm. The fact is that only a few additions were necessary, as it was expected at the beginning of the thesis. By defining the correct boundary and initial conditions and the appropriate incoming flow, the VPM code solves the flow which corresponds to a three-dimensional mixing layer.

Behind this apparent simplicity of implementation, there were several issues to overcome in order to make the code operational. The VPM code was never tested with the boundary conditions used for this work. Even though the code was globally ready to run with the desired boundary conditions, it was necessary to make some adaptations, with the consequent help of the supervisors and the assistant. Indeed, some functions which were already operational for other combinations of boundary conditions were not yet functional for the desired combination. Identifying, locating and then resolving these bugs have taken some time.

Algorithm 1 VPM code

Initialization :

1: $\omega_{ij}^0 = \omega_{init}$ ▷ equation (3.3)

Temporal loop :

2: **while** $t < t_{end}$ **do**

Domain

3: B.C. transverse : Dynamic resizing (if needed) ▷ section (3.2)

4: $\boldsymbol{\omega}_p^n \xrightarrow{\text{P2M from } \boldsymbol{x_p^n}} \boldsymbol{\omega}_{ij}^n$

5: B.C. streamwise : $\boldsymbol{\omega}_{ij}^n\Big|_{\substack{x=0\\x=end}}$ ▷ section (3.2)

6: $\boldsymbol{\omega}_{TIB,p}^n \xrightarrow{\text{P2M from } \boldsymbol{x_{TIB,p}^n}} \boldsymbol{\Omega}_{TIB,ij}$

7: $\boldsymbol{\Omega}_{TIB,ij} = \boldsymbol{\Omega}_{TIB,ij} + \boldsymbol{\omega}_{inflow}$ ▷ equation (3.7)

8: $\boldsymbol{\Omega}_{TIB,ij} \xrightarrow{\text{Blending}} \boldsymbol{\omega}_{ij}^n$

9: $\boldsymbol{\omega}_{ij}^n \xrightarrow{\text{Poisson}} \boldsymbol{\Psi}_{ij}^n$ ▷ equation (2.5)

10: $\boldsymbol{\Psi}_{ij}^n \xrightarrow{\text{FD}} \boldsymbol{u}_{ij}^n$ ▷ equation (2.4)

11: B.C. transverse : ghosts on $\boldsymbol{\omega}_{ij}^n$ and $\boldsymbol{u}_{ij}^n$ ▷ section (3.2)

12: B.C. streamwise : $\boldsymbol{u}_{ij}^n\Big|_{\substack{x=0\\x=end}}$, $\boldsymbol{\omega}_{ij}^n\Big|_{\substack{x=0\\x=end}}$ ▷ section (3.2)

13: $\boldsymbol{\omega}_{ij}^n \xrightarrow{FD} (\boldsymbol{\nabla}^2\boldsymbol{\omega})_{ij}^n$ & $\boldsymbol{u}_{ij}^n \xrightarrow{FD} (\boldsymbol{\nabla}\boldsymbol{u})_{ij}^n \Rightarrow \boldsymbol{Rhs}_{ij}^n$ ▷ equation (2.7)

14: LES : $\boldsymbol{Rhs}_{ij}^n = \boldsymbol{Rhs}_{ij}^n + f\left(\boldsymbol{\omega}_{ij}^n\right)$ ▷ section (2.5)

15: $\boldsymbol{u}_{ij}^n = \boldsymbol{u}_{ij}^n + U_\infty$

16: B.C. transverse : ghosts on $\boldsymbol{Rhs}_{ij}^n$

17: B.C. streamwise : $\boldsymbol{Rhs}_{ij}^n\Big|_{\substack{x=0\\x=end}}$

18: $\boldsymbol{Rhs}_{ij}^n \xrightarrow{\text{M2P on } \boldsymbol{x_p^n}} \boldsymbol{Rhs}_p^n$

19: $\boldsymbol{u}_{ij}^n \xrightarrow{\text{M2P on } \boldsymbol{x_p^n}} \boldsymbol{u}_p^n$

20: $\boldsymbol{x}_p^{n+1} = \boldsymbol{x}_p^n + \Delta t \cdot \boldsymbol{u}_p^n$ ▷ section (2.6)
$\boldsymbol{\omega}_p^{n+1} = \boldsymbol{\omega}_p^n + \Delta t \cdot \boldsymbol{Rhs}_p^n$

TIB

▷ section (3.4)

21: $\boldsymbol{u}_{TIB,ij}^n = U_\infty$ ▷ No Biot-Savart in the TIB

22: $\boldsymbol{u}_{TIB,ij}^n \xrightarrow{\text{Blending}} \boldsymbol{u}_{ij}^n$

23: $\boldsymbol{u}_{TIB,ij}^n \xrightarrow{\text{M2P on } \boldsymbol{x}_{TIB,p}^n} \boldsymbol{u}_{TIB,p}^n$

24: $\boldsymbol{\omega}_{TIB,p}^n \xrightarrow{\text{P2M from } \boldsymbol{x}_{TIB,p}^n} \boldsymbol{\omega}_{TIB,ij}^n$

25: $\boldsymbol{\omega}_{TIB,ij}^n \xrightarrow{\text{Blending}} \boldsymbol{\omega}_{ij}^n$

26: $\boldsymbol{\omega}_{TIB,ij}^n \xrightarrow{FD} (\boldsymbol{\nabla}^2\boldsymbol{\omega}_{TIB})_{ij}^n$ & $\boldsymbol{u}_{ij}^n \xrightarrow{FD} (\boldsymbol{\nabla}\boldsymbol{u}_{TIB})_{ij}^n \Rightarrow \boldsymbol{Rhs}_{TIB,ij}^n$

27: $\boldsymbol{Rhs}_{TIB,ij}^n \xrightarrow{\text{Blending}} \boldsymbol{Rhs}_{ij}^n$

28: $\boldsymbol{Rhs}_{TIB,ij}^n \xrightarrow{\text{M2P on } \boldsymbol{x}_{TIB,p}^n} \boldsymbol{Rhs}_{TIB,p}^n$

29: $\boldsymbol{x}_{TIB,p}^{n+1} = \boldsymbol{x}_{TIB,p}^n + \Delta t \cdot \boldsymbol{u}_{TIB,p}^n$
$\boldsymbol{\omega}_{TIB,p}^{n+1} = \boldsymbol{\omega}_{TIB,p}^n + \Delta t \cdot \boldsymbol{Rhs}_{TIB,p}^n$

30: $\boldsymbol{\omega}_{data,ij}^n \xrightarrow{\text{M2P near the entry of the TIB}} \boldsymbol{\omega}_{TIB,p}^{n+1}$ ▷ Feeding of the TIB with the database

Domain

31: B.C. spanwise + reinsertion of particles into the domain ▷ section (3.2)
32: Mapping of the particles

TIB

33: $\boldsymbol{\omega}_{TIB,p}^{n+1} \xrightarrow{\text{P2M from } \boldsymbol{x}_{\boldsymbol{TIB,p}}^{\boldsymbol{n+1}}} \boldsymbol{\Omega}_{TIB,ij}$
34: $\boldsymbol{\Omega}_{TIB,ij} = \boldsymbol{\Omega}_{TIB,ij} + \boldsymbol{\omega}_{inflow}$ ▷ equation (3.7)
35: $\boldsymbol{\Omega}_{TIB,ij} \xrightarrow{\text{M2P on } \boldsymbol{x}_{TIB,p}^{n+1}} \boldsymbol{\Omega}_{TIB,p}$
36: $\boldsymbol{\Omega}_{TIB,p} \xrightarrow{\text{Blending}} \boldsymbol{\omega}_{p}^{n+1}$

Domain

37: Remeshing of particles (if it is time to) : $\xrightarrow{\text{P2M from } \boldsymbol{x}_{\boldsymbol{p}}^{\boldsymbol{n+1}}}$ ▷ section (2.4)
38: Reprojection of $\boldsymbol{\omega}_{\boldsymbol{ij}}^{\boldsymbol{n+1}}$ (if it is time to) ▷ section (2.4)
39: **end while**

3.6 Simulation parameters

3.6.1 Constraints

The choice of the simulation parameters is crucial because it will determine the quality of the results. A bad choice of parameters can lead to results that do not correspond to the physics, even though the computations performed by the solver are correct. That is why special care has been taken to choose the best possible the parameters, on the basis of the following constraints :

1. **Maximum number of points** : the more points, the more it is possible to solve exactly the smallest turbulent scales. It is obviously interesting to produce results as accurate as possible but limitations exist in terms of computational resources. First, the time during which simulation will run is limited by the clusters. This issue can be circumvented by the "restart" functionality of VPM code which allows to restart a simulation from a certain instant. This feature has been used extensively to realize the simulation. The second issue is linked with the available memory on the clusters. Nowadays, this aspect is the most restrictive one when numerical simulations are performed. With VPM, a maximum of $1 \cdot 10^9$ to $2 \cdot 10^9$ points can be envisaged on *Zenobe*, the most powerful cluster in Wallonia ;

2. **Simulation time** : hoping to have fully converged results, the simulation should ideally reach at least two convective times t_{conv} defined by

$$t_{conv} = \frac{L_x}{U_c}.$$

   Intermediate simulations made it possible to estimate the required CPU time to reach $2 \cdot t_{conv}$. Using the maximum number of points would have led to a far too long simulation and that is why the total number of points has been chosen to be less than this upper limit;

3. **Number of points and *FFT*** : the Fast Fourier Transform algorithm enables the computation of the discrete Fourier transform in $\mathcal{O}(N \log N)$ floating point operations if the number of points N is highly composite, that is, a product of small prime factors [34]. In order to take advantage of this gain in speed, a number of points respecting this condition have been chosen in each of the three spatial directions ;

4. **Spanwise length** L_z : let us recall that the initial spanwise perturbation which is superposed on the initial vorticity profile is composed of the fundamental spanwise wavelength of the Kelvin-Helmholtz instability λ_z. Since the spanwise direction is periodic, the length

in this direction is chosen to be a multiple of λ_z. Moreover, the spanwise length must be large enough to allow the proper development of the rollers. Indeed, if it is too small, the large scale structures of the flow could be truncated and the expected three-dimensional phenomena could be affected. In order to choose a priori a correct spanwise length, the following criterion has been met:

$$L_z = 2 - 3 \cdot \delta_{vis,final} \ ,$$

where $\delta_{vis,final}$ is the visual thickness (equation (1.21)) at the end of the domain. This quantity was estimated on the basis of the growth rate of the vorticity thickness measured in the experiment of Brown and Roshko [11]:

$$\delta_\omega = 0.088 \cdot (x - x_0)$$

where the virtual origin x_0 was chosen to be equal to 0, which is the situation where the mixing layer is the more spread. Then, $y_{0.9}(x)$ and $y_{0.1}(x)$ were computed on the basis of their definitions (equation (1.21)) by using the initial velocity profile as the mean profile (equation (3.1)). This estimation gave

$$\delta_{vis,final} \approx 17.3 \ ;$$

5. **Streamwise length** L_x : the streamwise length needs to be chosen in such a way that the fully turbulent region of the flow occupies at least half of the computational domain. This choice of parameter was made by carrying out pre-simulations before launching the final simulation. Indeed, the choices of the initial and incoming profiles as well as the perturbations strongly influence the instabilities growth rate and thus the position of the origin of the turbulent region. It is therefore through an iterative process that the appropriate combination of these parameters has been determined ;

6. **Resolution** : during a previous simulation, the flow was seen to be under-resolved at certain points in the domain[1], in particular in the "filaments" connecting two successive vortices. This observation led to discretize the initial vorticity thickness with at least 7 to 8 grid points, which set a maximum spatial step ;

7. **Spatial step** : in a particle methods, the particles carrying the information are isotropic and the spatial steps in each direction have to be equals.

3.6.2 Values

The parameters of the final simulation have been selected by meeting the constraints cited above. They are presented in table 3.1 on page 30.

3.6.3 Comparison with some references

The following comments can be made based on the analysis of table 3.2 on page 30 :

- **Reynolds number** : the selected initial Reynolds number is very high compared to the other works. With a simple LES model of the type "Smagorinsky", this could be problematic since most of the flow scales would be solved by the LES model instead

[1] In fact, with a LES, the flow is always under-resolved since the smallest scales are modeled but the more the points, the more the range of scales being resolved exactly is large.

[2] The values for the dimensions are approximate because the initial vorticity thickness was not directly available and it was therefore measured on a graph in the article.

of being resolved exactly[3]. Hopefully, the implemented RVM model (see section 2.5) is activated only where the flow exhibits large fluctuations and acts only on the smallest scales. The LES model does not influence the laminar region of the flow or the large scale structures, for example, which guarantees a good accuracy. The subgrid viscosity ν_{SGS} totally dominates the molecular viscosity ν_m in the majority of the flow ;

- **Streamwise dimension** : the length of the domain is two to three times greater in the references. Nevertheless, with the high value of $Re_{\delta_{\omega_0}}$ and the perturbations added to the incoming and initial vorticity, the mixing layer develops fairly quickly. The fully-turbulent region of the flow thus occupies a reasonable portion of the domain so that correct statistics can be realized ;

- **Spanwise dimension** : the ratio between the length and the width of this domain L_x/L_z is nearly two times smaller than for the two LES simulations presented in the table (for the DNS simulation, the gap is even greater). Here, three possibilities are conceivable :

  - it was not necessary to choose such a large width for this domain. A smaller width might not have influenced too much the good development of the flow ;
  - the width chosen in the references is perhaps too low, which influences the flow too much by "enclosing" it ;
  - the growth rate of the mixing layers in the references is smaller than in the present simulation, the visual thickness evolves slower and the width can be chosen also smaller, relative to the length (see point 4 of section 3.6.1).

  In [3], a study of the influence of the spanwise dimension was realized by conducting a simulation on a domain twice as wide. Their conclusions seem to substantiate the first possibility : «No significant influence of the spanwise extent is recorded on the distribution of the vorticity thickness. Both results correspond to a linear δ_ω which agrees well with the experimental data.» ;

- **Number of points** : let us notice first that the mesh in the transverse direction is tightened around the centerline of the mixing layer in the three references, so that they can afford a reduced number of points in this direction. What is rather surprising is to notice that the mesh spacing in the streamwise and spanwise direction Δx and Δz is twice as large in the DNS simulation compared to the present mesh resolution. This may be explained by their relatively low Reynolds number value. In any case, their spatial resolution seems to be fine enough : «In this simulation, we also set the spatial resolution to about 3η (where η is the Kolmogorov length)» [37]. This observation could imply that by decreasing the present Reynolds number, a DNS could have been made while keeping the same spatial resolution. The present resolution is indeed very good with 11 mesh points in the initial vorticity thickness.

[3] Indeed, a high Reynolds number implies that the lengthscale of the smallest eddies η, also called the Kolmogorov lengthscale, is particularly small compared to the lengthscale of the largest eddies l_o since their ratio η/l_0 is proportional to $Re^{-3/4}$. Therefore, if the mesh is not sufficiently fine, the LES model will resolve most of the lengthscales.

	Symbol	Name	Value	Comments
Initial and incoming profiles	U_1	upper velocity	1.0	the same value as in [11]
	U_2	lower velocity	0.38	the same value as in [11]
	δ_{ω_0}	initial vorticity thickness	1.0	chosen arbitrarily to have simple values for the dimensions
	$Re_{\delta_{\omega_0}}$	Reynolds number based on the initial vorticity thickness	$1 \cdot 10^5$	high Reynolds number turbulent flow
Initial and incoming perturbations	λ_x	streamwise fundamental wavelength of the K-H instability	$14.0 \cdot \delta_{\omega_0}$	relation from [35]
	λ_z	spanwise fundamental wavelength of the K-H instability	$0.6 \cdot \lambda_x$	relation from [22]
	A_{pert}	amplitude of the initial perturbations	$0.05 \cdot \omega_{init,max}$	
	TI	turbulence intensity of the incoming flow	0.25%	typical value of wind tunnel experiments [20]
Discretization	$N_x \times N_y \times N_z$	number of points in each direction	$2048 \times 384 \times 768$	total of $\pm 6 \cdot 10^8$ points
	$L_x \times L_y \times L_z$	length in each direction	$179.2 \times 33.6 \times 67.2$	L_y can slightly increase with the dynamic resizing
	Δx	spatial step	0.0875	The same in each direction.
	Δt	initial time step	0.06	Δt is divided by ≈ 2 during the simulation : adaptative time step
VPM	N_{remesh}	frequency of particles remeshing	5 time steps	
	$N_{solenoidal}$	frequency of solenoidal reprojection	20 time steps	
Computational resources	N_{procs}	number of processors in each direction	$32 \times 4 \times 8$	total of 1024 processors
	/	total memory	2688000 $[MB]$	2625 $[MB]$ per processor
	t_{exec}	total execution time	200 hours	it corresponds to 7 restarted runs
Simulation time	t_{simu}	time reached at the end of the simulation	886	
	$N_{t_{conv}}$	number of convective time	3.4	$t_{conv} = 260$
	$N_{\Delta t}$	number of time steps	27300	

Table 3.1: Simulation parameters

References \ Parameters	$Re_{\delta_{\omega_0}}$	$(L_x \times L_y \times L_z)/\lambda_x$	$N_x \times N_y \times N_z$	Type
VPM	$1 \cdot 10^5$	$12.8 \times 2.4 \times 4.8$	$2048 \times 384 \times 768$	LES
[35]	700	$25 \times 6.5 \times 5$	$1024 \times 200 \times 64$	LES
[37]	700	$30 \times 6 \times 2.6$	$2160 \times 433 \times 192$	DNS
[3][2]	1750	$35.5 \times 8.5 \times 7$	$501 \times 71 \times 55$	LES

Table 3.2: Comparison with some references

4 Results

4.1 Introduction

In this last chapter, the results from the simulation are presented and commented. First, two- and three-dimensional views of the velocity and vorticity are shown in order to have a global view of the flow and to observe the large-scale turbulent structures. Then, it is usual to present the results with one-point statistics showing the mean velocity profiles and the variances and the covariances of the fluctuating parts of the velocity measured at different streamwise locations. These graphs are scaled with the similarity variable η in order to highlight the self-similarity of the various profiles. The growth rate and the velocity spectrum are also analyzed.

Before inspecting all these figures, here are some information about the statistics applied to the velocity field.
In the axis labels of the graphs presented below, the "overline operator" $\overline{\bullet}$ designates a temporal mean *with* a spatial mean in the periodic spanwise direction :

$$\overline{\bullet} = \frac{1}{L_z T} \int_{L_z} \int_{T} \bullet \, \mathrm{d}t \, \mathrm{d}z \ ,$$

where T is the period in which the statistics were collected. The statistics were first spatially averaged in a single spanwise plane before applying a time average. More precisely, this mean operator applies on the resolved velocity components of the LES. So, one should write $\overline{\overline{\mathbf{v}}}$ instead of just $\overline{\mathbf{v}}$. But for the sake of readability, the second notation will be kept.
In table 4.1, the statistics parameters are listed.

During the simulation, the statistics $\overline{u_i}$ and $\overline{u_i u_j}$ were collected. The calculation of the

Symbol	Name	Value
$[t_1, t_2]$	time interval	$[450, 880] = [1.73, 3.38] \cdot t_{conv}$
T	period	430
$N_{t_{conv}}$	number of convective times	1.65
$\% \, t_{simu}$	% of the total simulation time	50 %

Table 4.1: Statistics parameters

components of the Reynolds stress tensor was made using one of the property of the mean operator :

$$\overline{u_i' u_j'} = \overline{u_i u_j} - \overline{u_i} \cdot \overline{u_j}.$$

Finally, let us recall that the initial vorticity thickness $\delta_{\omega_0} = 1$, so that when "$x = 100$" is written for example, this can be seen as the streamwise location corresponding to 100 times the value of the initial vorticity thickness. In the same way, when the time "t" is written in the following, it is a time made dimensionless with δ_{ω_0} and U_1.

4.2 2-D and 3-D views

4.2.1 2-D views

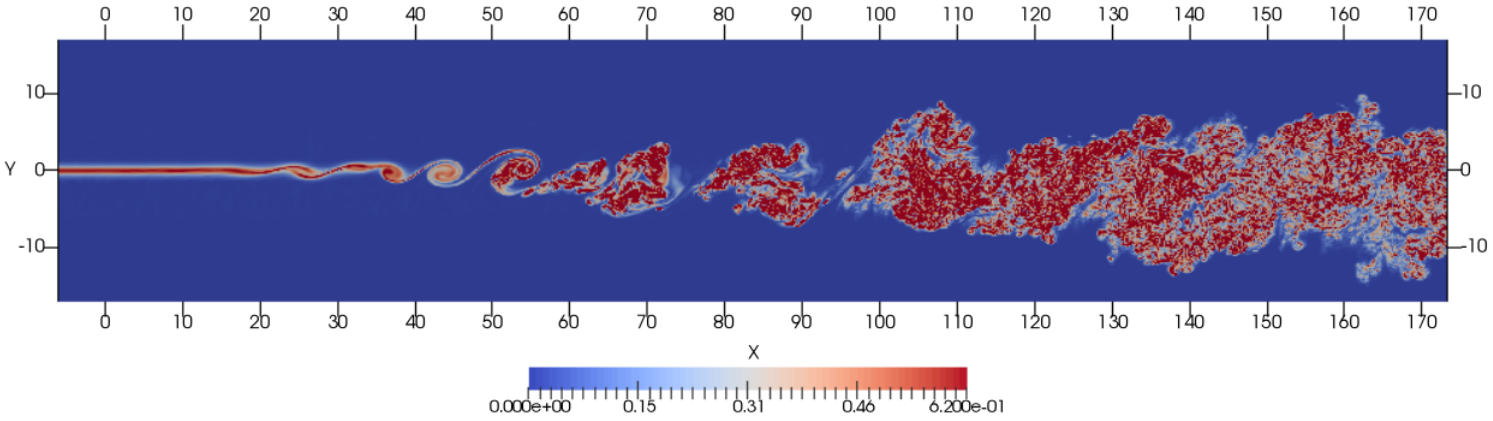

Figure 4.1: Slice of the norm of $\boldsymbol{\omega}$ saturated at the value of $\omega_{init,max}$ at t = 812 $(3.12 \cdot t_{conv})$.

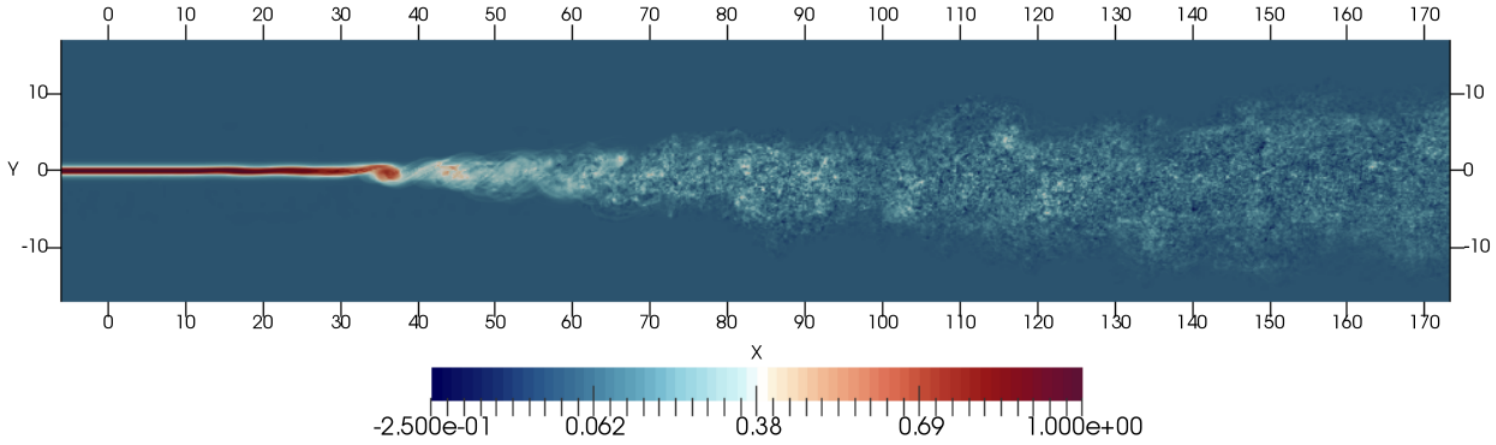

Figure 4.2: Spanwise average of $\omega_z/\omega_{init,max}$ at t = 812 $(3.12 \cdot t_{conv})$.

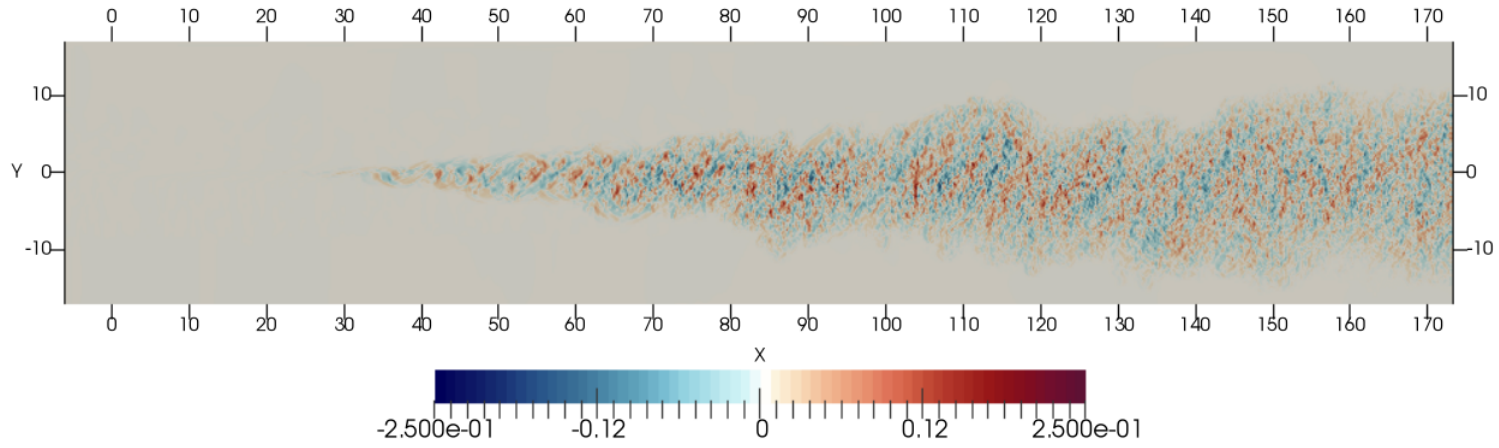

Figure 4.3: Spanwise average of $\omega_y/\omega_{init,max}$ at t = 812 $(3.12 \cdot t_{conv})$.

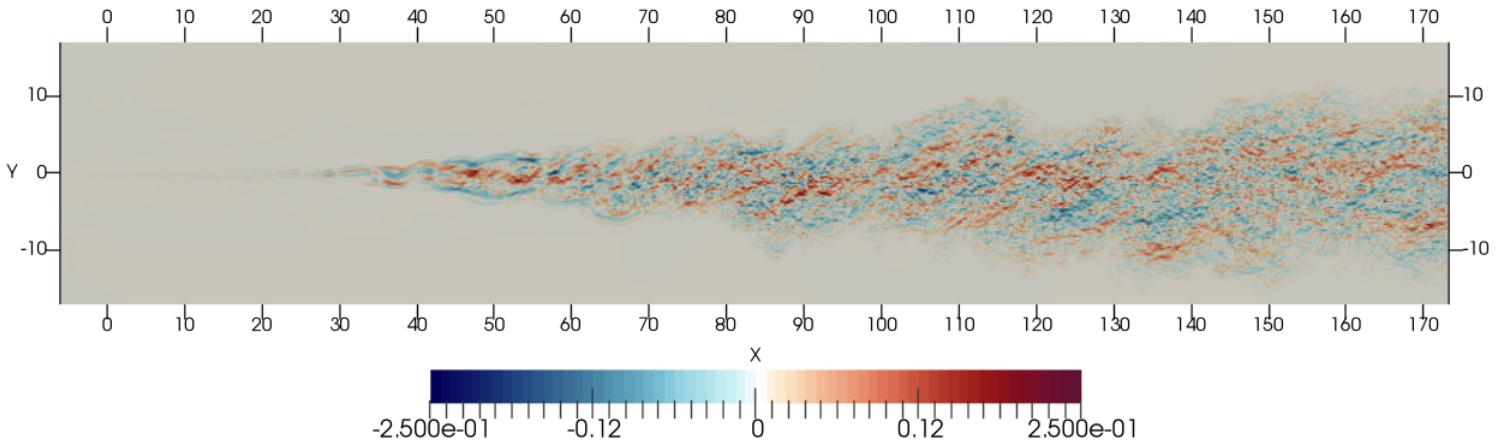

Figure 4.4: Spanwise average of $\omega_x/\omega_{init,max}$ at t = 812 $(3.12 \cdot t_{conv})$.

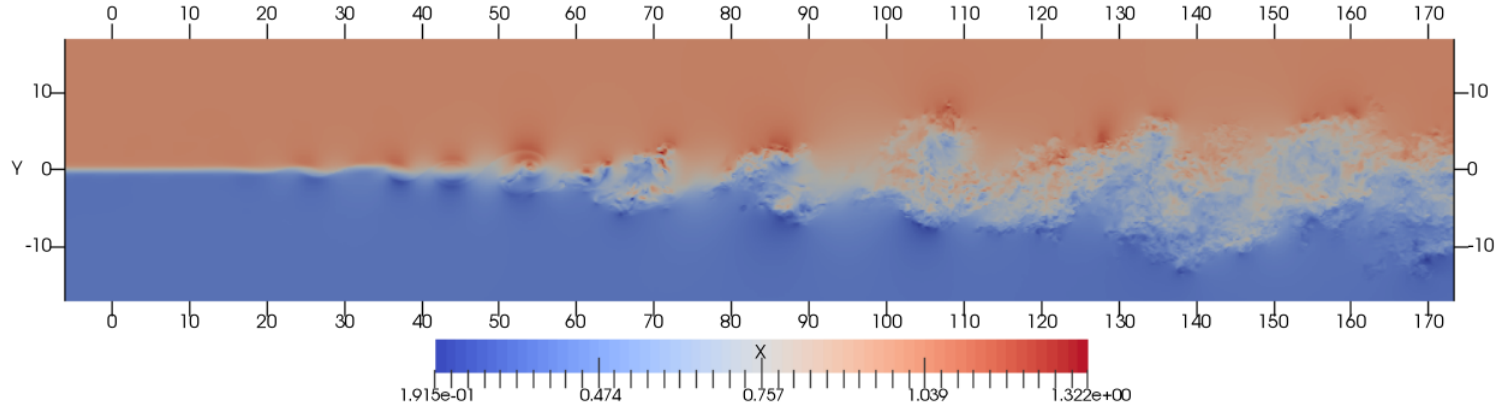

Figure 4.5: Slice of u/U_1 at t = 812 $(3.12 \cdot t_{conv})$.

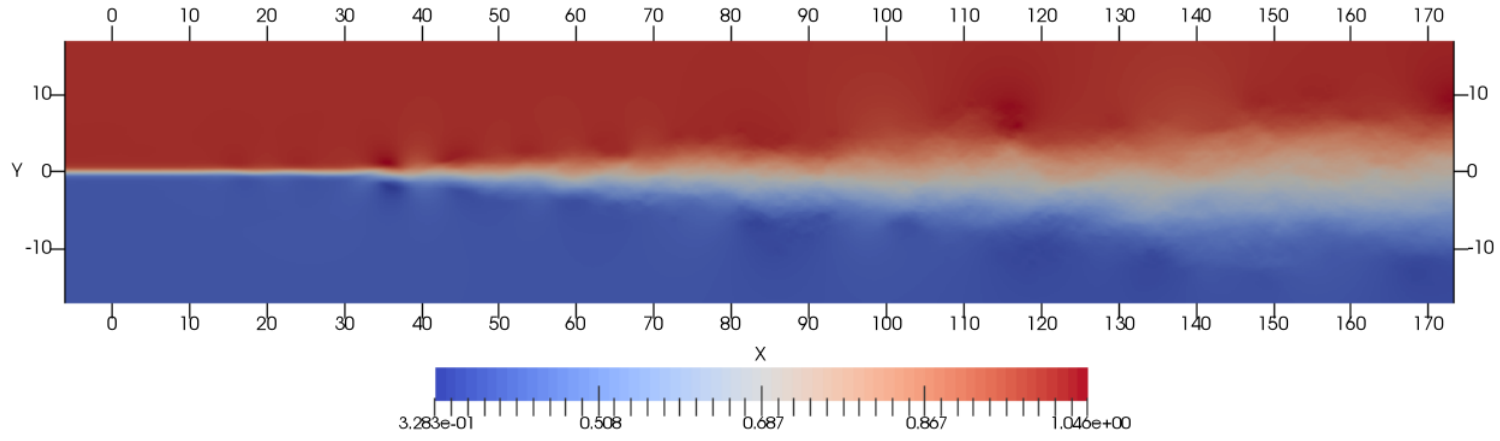

Figure 4.6: Spanwise average of u/U_1 at t = 812 $(3.12 \cdot t_{conv})$.

4.2.2 Comments

The following comments can be made about figures 4.1 to 4.6 :

- in figure 4.1, different zones of the flow can be analyzed. From the beginning of the domain to $x \simeq 15$, the initial vorticity slab has still the same shape and the flow in this region can be seen as laminar. Then, from $x \simeq 15$ to $x \simeq 30$, the development of the Kelvin-Helmholtz instabilities is visible. First, waves appear in the initial vorticity slab before the vorticity begins to roll up. Between $x \simeq 30$ and $x \simeq 45$, spanwise vortex rollers form. The flow has remained until here quite two-dimensional. Then, from $x \simeq 50$ to $x \simeq 70$, the spanwise rollers are influenced by three-dimensional effects and small scales motions appear. It is the transition zone. After $x \simeq 70$, the flow is fully turbulent with strong three-dimensional dependence and the presence of small scales motions. One can guess the pairing of two vortex structures between $x \simeq 60$ and $x \simeq 70$ and also between $x \simeq 80$ and $x \simeq 90$. The visualization of large-spanwise coherent structures becomes not very clear ;

- in figure 4.2, the spanwise vorticity has been averaged along with the periodic spanwise direction. The result may seem surprising at first glance. The spanwise-averaged vorticity intensity is lower in the fully turbulent part of the flow than in the laminar part. When a simple slice is considered, it is the opposite (see figure 4.1 and D.1). In fact, with three-dimensional turbulence, the places where the vorticity is most intense differ from one plane to another. Moreover, in a given plane, places where vorticty is maximal can be adjacent to places with a low vorticity due to the small scales motions. Therefore, the spanwise average results in this view. Let us remark that this view bears resemblance to those presented in [35]. The transition zone can be identified to range from $x \simeq 40$ to $x \simeq 70$ as the distribution of vorticity in the flow changes «from being concentrated in the laminar vortex cores into a more uniform distribution» [35]. Finally, this view perfectly illustrates the quasi-linear growth rate of the layer if one imagines straight lines adjacent to the edges of the mixing layer ;

- in figures 4.3 and 4.4, the place from which the streamwise and transverse vorticity becomes non-zero marks the beginning of three-dimensional motions. The growth of the layer is again clearly visible. Note that the intensities of the two spanwise-averaged vorticity fields are substantially the same ;

- in figure 4.5, the streamwise velocity slice shows well the vortex structures and the resulting mixing in the layer. It also shows that the vortices rotate in the clockwise direction : the velocity at the top of a vortex is higher than the high speed free-stream velocity while the velocity at the bottom of a vortex is lower than the low speed free-stream velocity ;

- in figure 4.6, the spanwise-averaged streamwise velocity shows that, as the layer grows, the transition from the upper free-stream velocity to the lower one is done in an increasingly larger region. Furthermore, outside of the mixing layer, the velocity is not exactly equal to U_1 or U_2, in the upper or lower part, respectively. There are regions where the velocity is slightly higher and other where it is slightly lower. It depends on the positions of the vortices at this moment.

4.2.3 3-D views

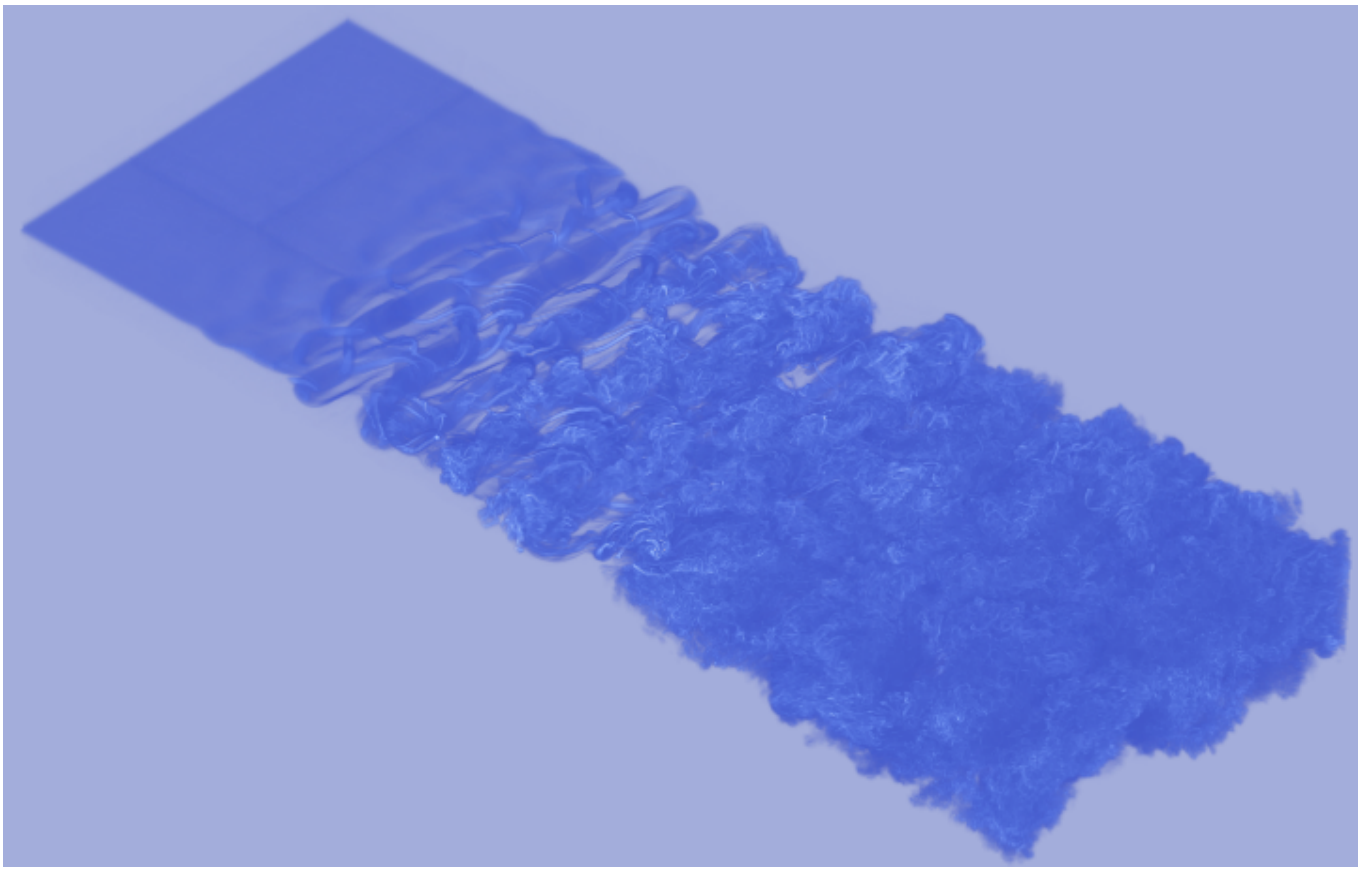

Figure 4.7: 3-D view of the magnitude of the vorticity field at t = 800 ($3.08 \cdot t_{conv}$).

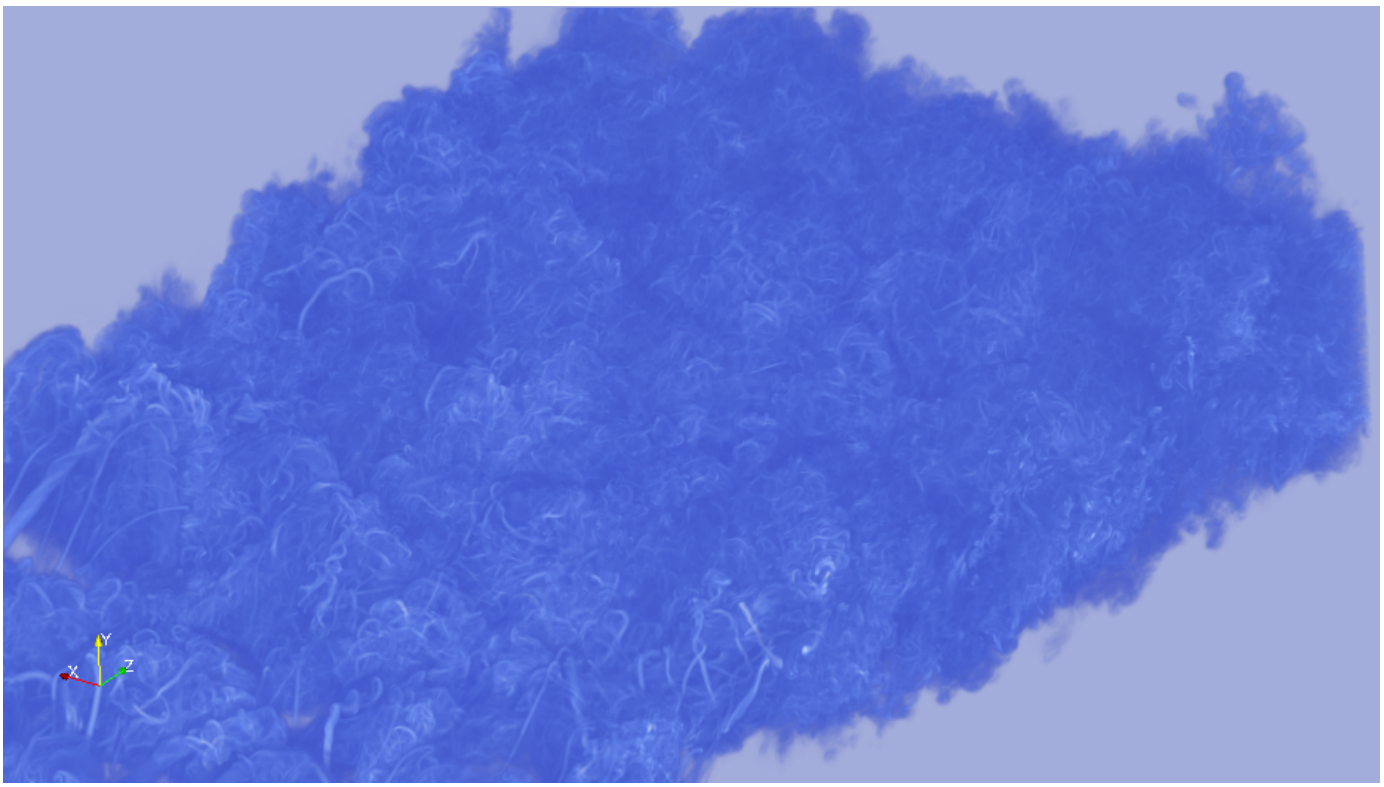

Figure 4.8: Another 3-D view of the magnitude of the vorticity field centered on the fully-turbulent region of the flow at t = 800 ($3.08 \cdot t_{conv}$).

4.2.4 Comments

The following comments can be made about figures 4.7 and 4.8 :

- in figure 4.7, the large two-dimensional rollers that span over the entire width of the domain are clearly visible in the transition region. Because three-dimensional effects are present, these spanwise rollers are somewhat deformed along the periodic direction. The three-dimensional effects are manifested by the appearance of streamwise vortices (often called the ribs) in the braid region between two successive rollers. These secondary vortices interact with the primary ones and produce fine-scale turbulence. In the second half of the domain, the flow is fully turbulent and the large coherent structures disappear and are replaced with fine scale turbulent motions ;
- in figure 4.8, the fully-turbulent region of the flow is shown more closely. Many tube-like small scale structures can be identified. These structures are called «coherent fine scale eddy and are considered as a universal structure in complicated turbulent flows» [37] ;

Other two- and three-dimensional views are presented in appendix D.

4.3 Determination of the self-similar region

It has already been mentioned on the basis of the slices above that the transition zone seemed to terminate in the vicinity of $x \simeq 70$. Before this position, it is in principle not expected to obtain self-similar profiles. The studied region of the flow should therefore start from $x \simeq 70$ at least. There is also a constraint on the end position of this region. Indeed, the statistics are inevitably influenced by the outlet boundary condition and the profiles should not be considered in the region "polluted" by this condition. In order to evaluate the region of influence of this outflow condition and the end of the transition region, figures 4.9 and 4.10 are used.

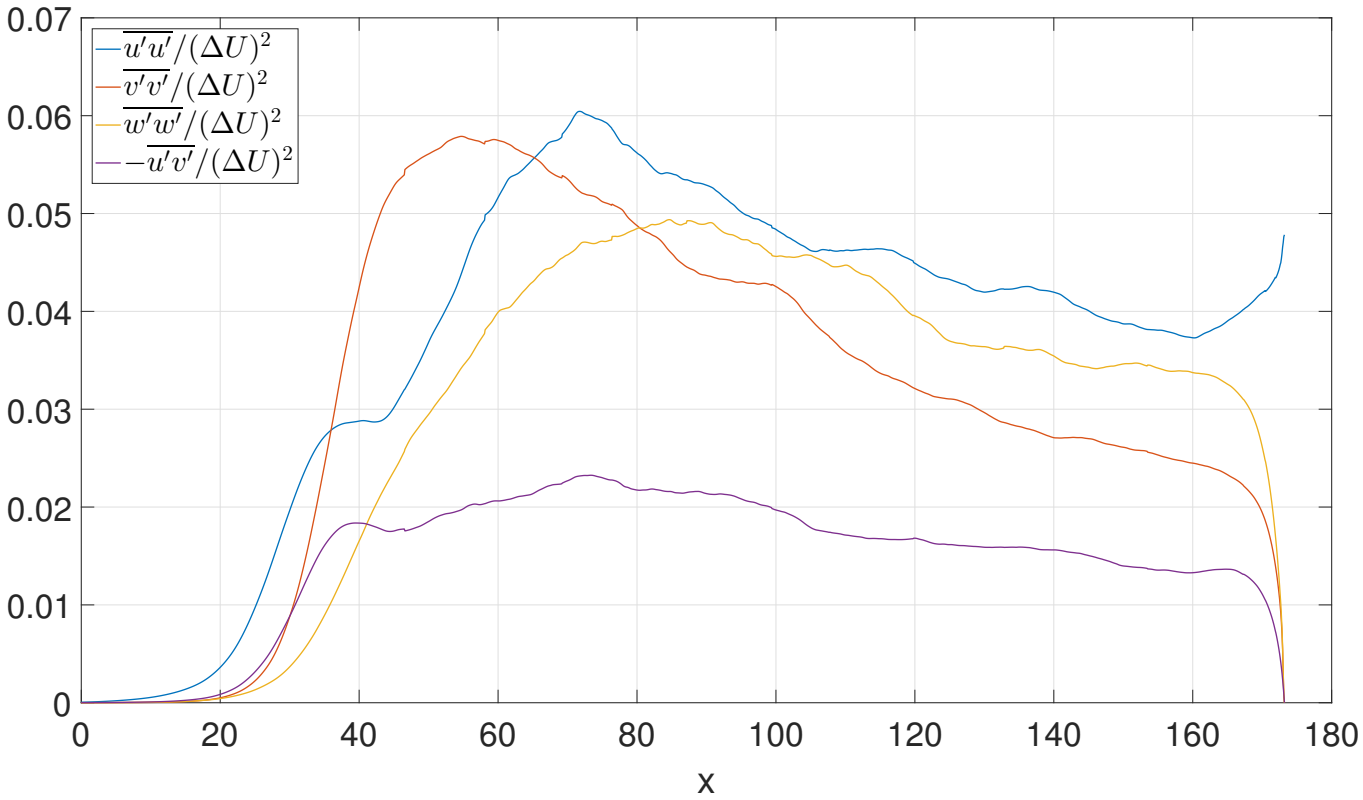

Figure 4.9: Streamwise evolution of the Reynolds tensor components on the dividing streamline.

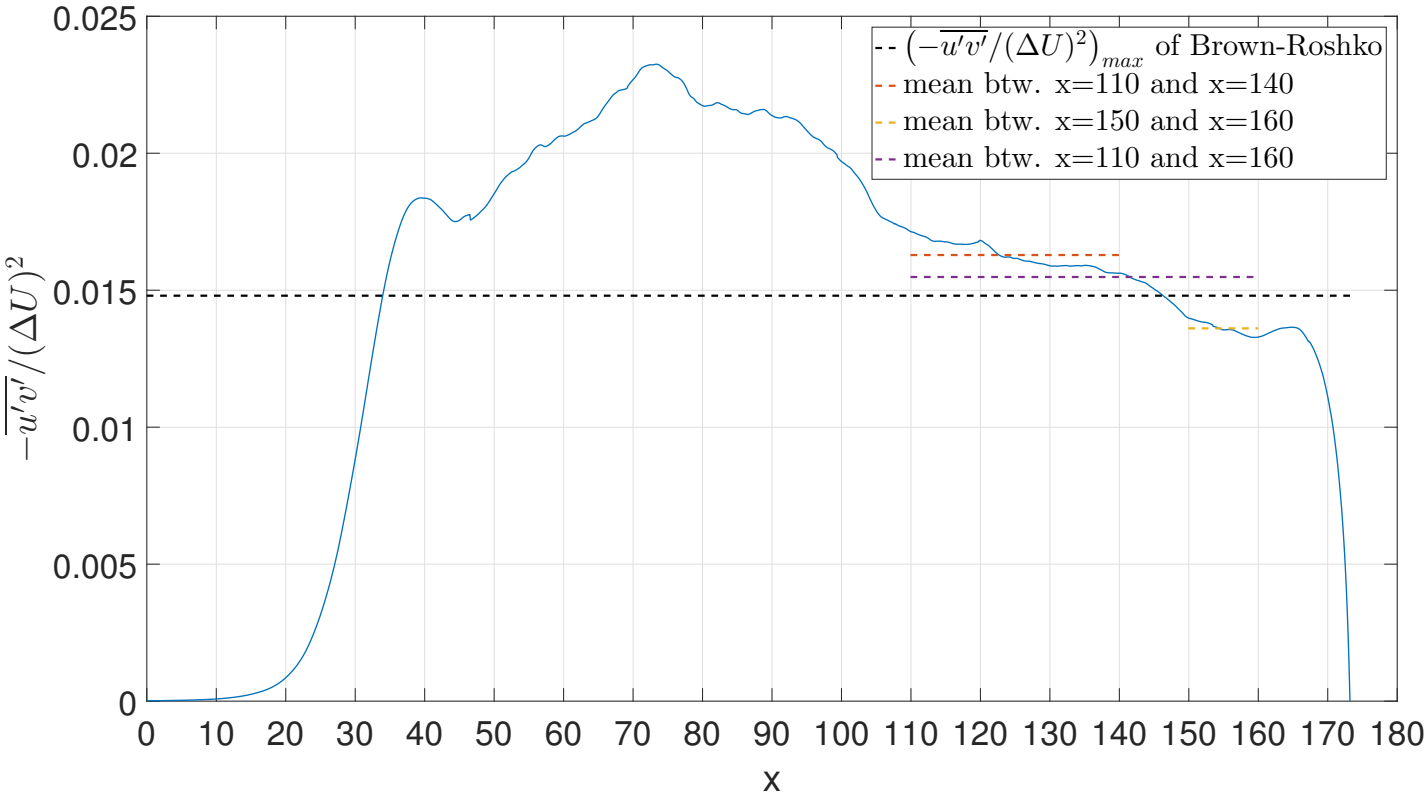

Figure 4.10: Streamwise evolution of the turbulent shear stress on the dividing streamline.

The following comments can be made about these figures :

- the boundary condition imposing $v = w = 0$ at the outflow (see section 3.2) seems to have an influence until $x \simeq 160$;
- the variances and the covariance of the velocity fluctuations are zero in the laminar region. Then, they grow until reaching a peak value around $x \simeq 55$ for $\overline{v'v'}$ and $x \simeq 85$ for $\overline{w'w'}$. These peaks in the profiles could correspond to «the mean locations of the first vortex amalgamations» while the shoulder in the curve of $\overline{u'u'}$ is «due to the roll-up of the layer into primary vortices» [35]. After these peaks, the level of turbulence progressively decreases as it it the case for the graphs presented in [35] ;
- let us remark that these curves follow the dividing streamline (equation (1.24)) and on this streamline, $\left(-\overline{u'v'}\right)^* = \left(-\overline{u'v'}\right)_{max}$ should be constant in the region of self-similarity based on the experimental results of Brown and Roshko [11]. In figure 4.10, the region between $x = 110$ and $x = 140$ was identified as potentially self-similar (in the sense of Brown and Roshko) because the value of $\left(-\overline{u'v'}\right)^*$ reaches a quasi-plateau represented by the red dot line. In the following, particular attention will be paid to this region, especially to estimate the growth rates of the mixing layer where a linear regression will be made on this region only. Another plateau represented by the yellow dot line, between $x = 150$ and $x = 160$, was identified but will not be considered because there is a risk that this region is influenced by the outflow condition. Finally, the purple dot line represents the mean of $\left(-\overline{u'v'}\right)^*$ between $x = 110$ and $x = 160$ and is pretty close to the experimental value recorded by Brown and Roshko (black dot line). The comparison between the two situations is discussed in section 4.11.

On the basis of these considerations, it was chosen to study the flow region between $x = 70$ and $x = 150$ and the different figures that follow will present profiles from $x = 70$ to $x = 150$ by step

of 10. For the graphs of the layer thicknesses, two linear regressions will be made : one from $x = 70$ to $x = 150$ and another one in the potential region of self-similarity from $x = 110$ to $x = 140$, as explained before.

4.4 Velocity profiles and virtual origin

4.4.1 Comments

The following comments can be made about figures 4.11 and 4.12 :

- in figure 4.11, the various mean streamwise velocity profiles have the same shape as the initial profile and the theoretical profile (see figures 3.1 and 1.2). The velocity profiles tend towards U_2 and U_1 more and more slowly as one moves downstream, which simply reflects the growth of the mixing layer ;
- in figure 4.11, the transverse locations on which the streamwise mean velocity has a value $\overline{u} = \delta \cdot U_1$, with $\delta = [0.55,\ 0.65,\ 0.7,\ 0.8,\ 0.85,\ 0.9]$, are identified by black dots. These dots are then reported into the $x - y$ plane in figure 4.12 and linear regressions are computed in order to find several lines intersecting in a same point, the virtual origin x_0 ;
- the value of the virtual origin is found to be $x_0 \simeq 10$ and will be used to form the similarity variable η (see equation (1.25)).

4.4.2 Graphs

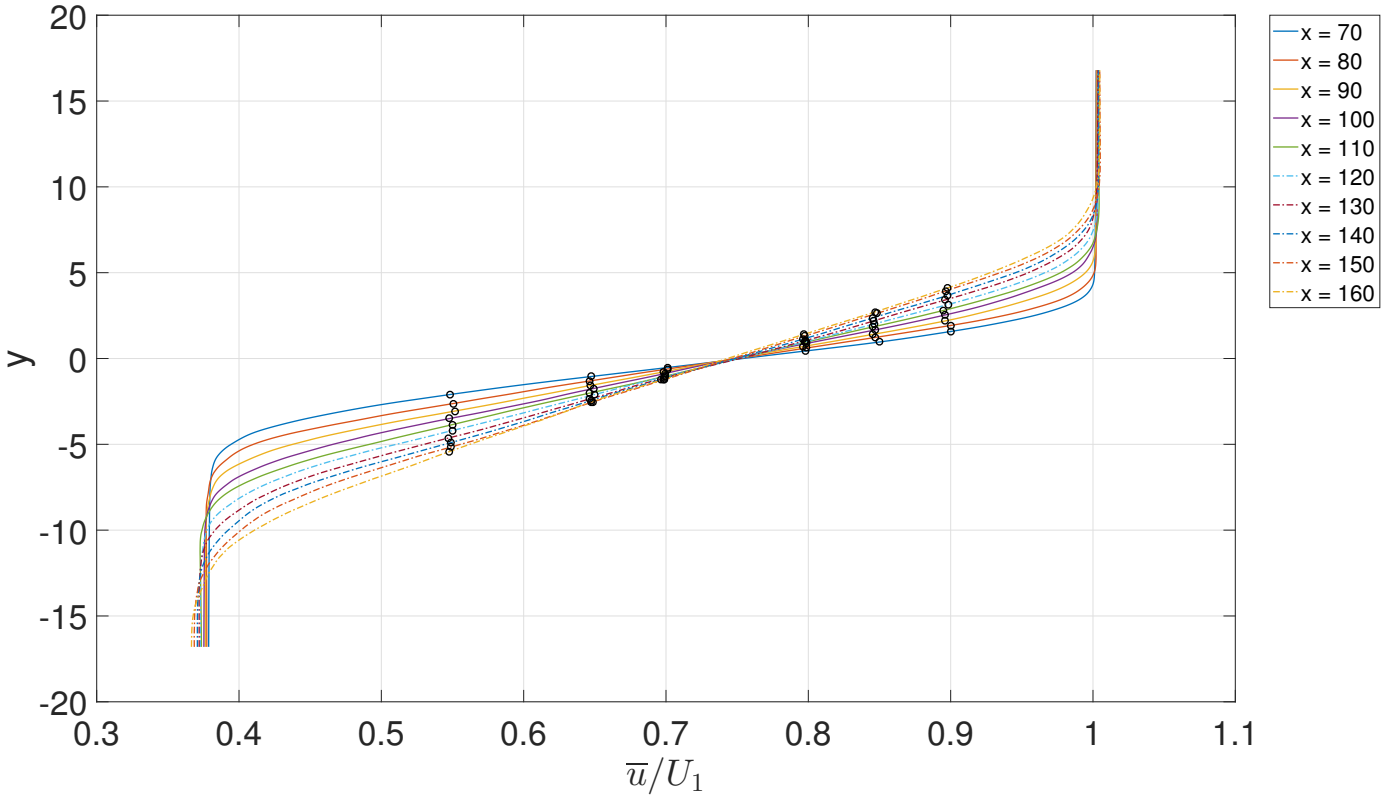

Figure 4.11: Mean velocity profiles for different x locations. The black dots are drawn to find the virtual origin.

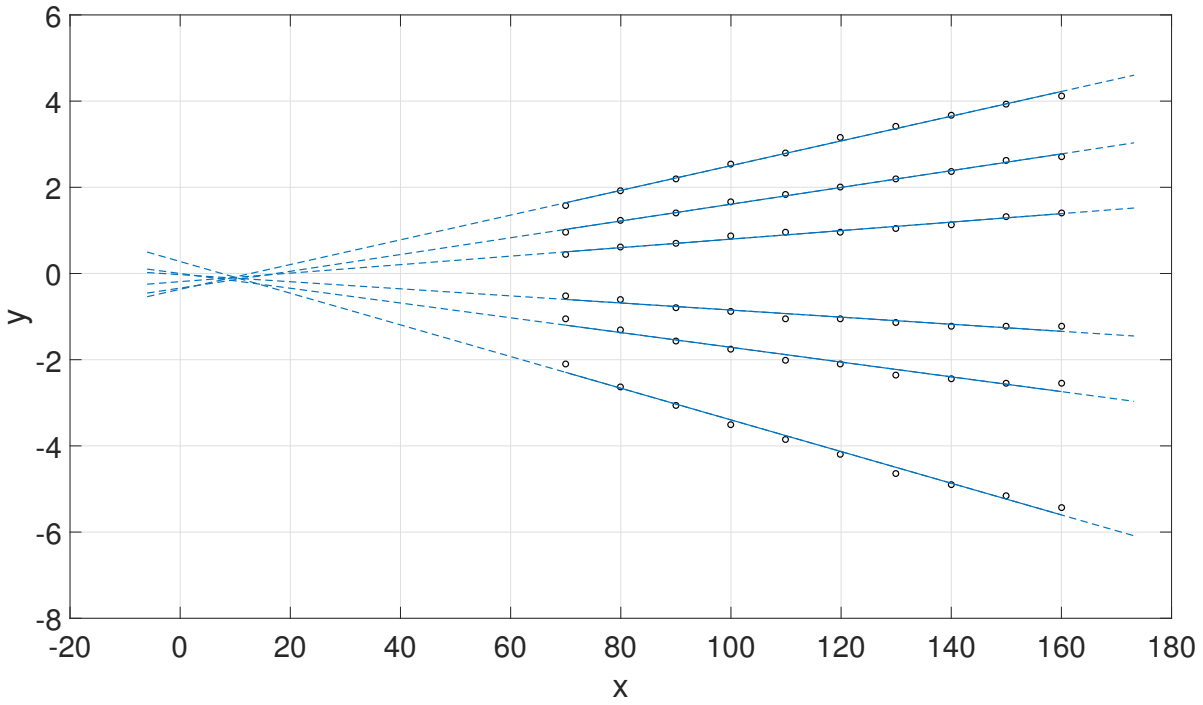

Figure 4.12: Determination of the virtual origin. Linear regressions between $x = 70$ and $x = 160$ (solid blue lines) and their extensions (dash blue lines).

4.5 Mean velocity profiles

4.5.1 Graphs

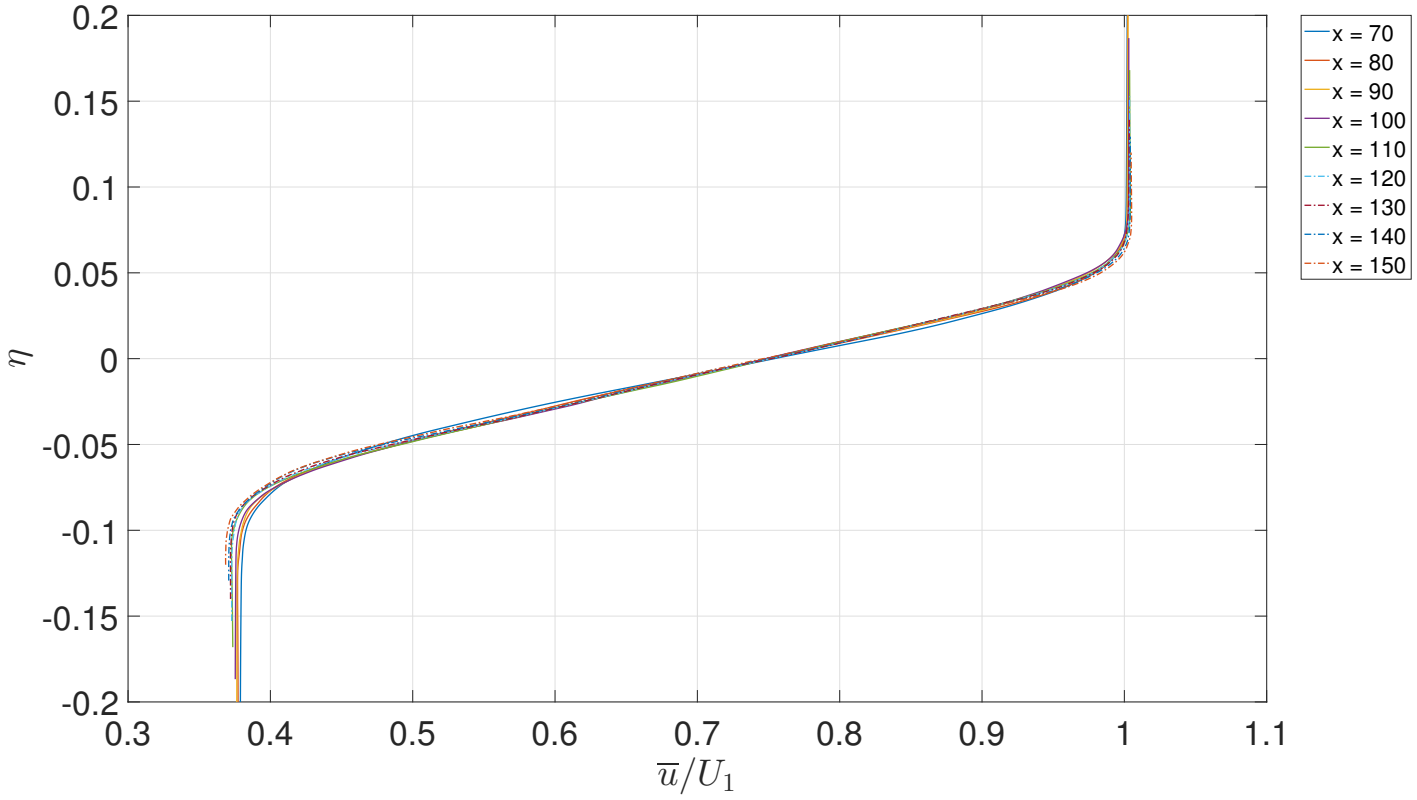

Figure 4.13: Mean streamwise velocity profiles at different x locations as a function of η.

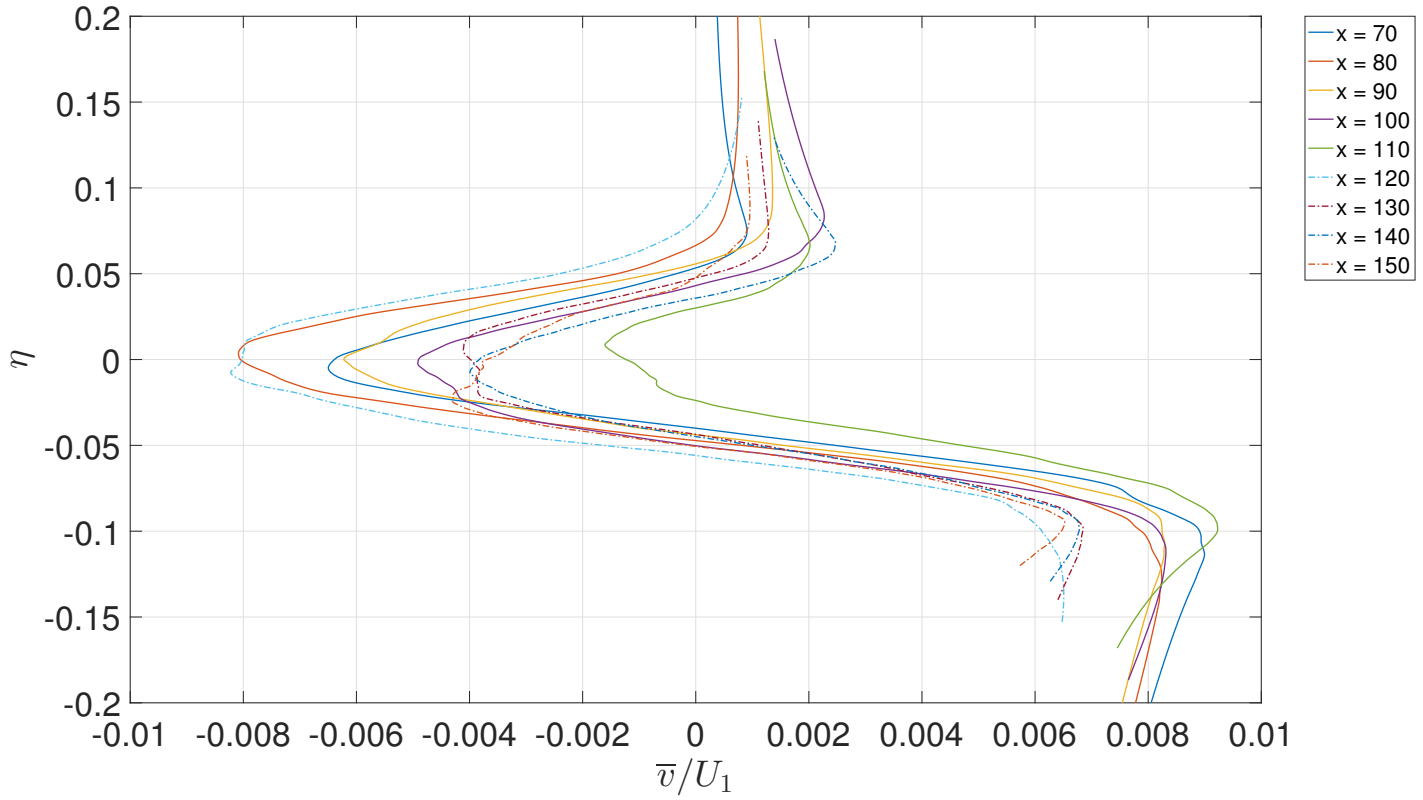

Figure 4.14: Mean transverse velocity profiles at different x locations as a function of η.

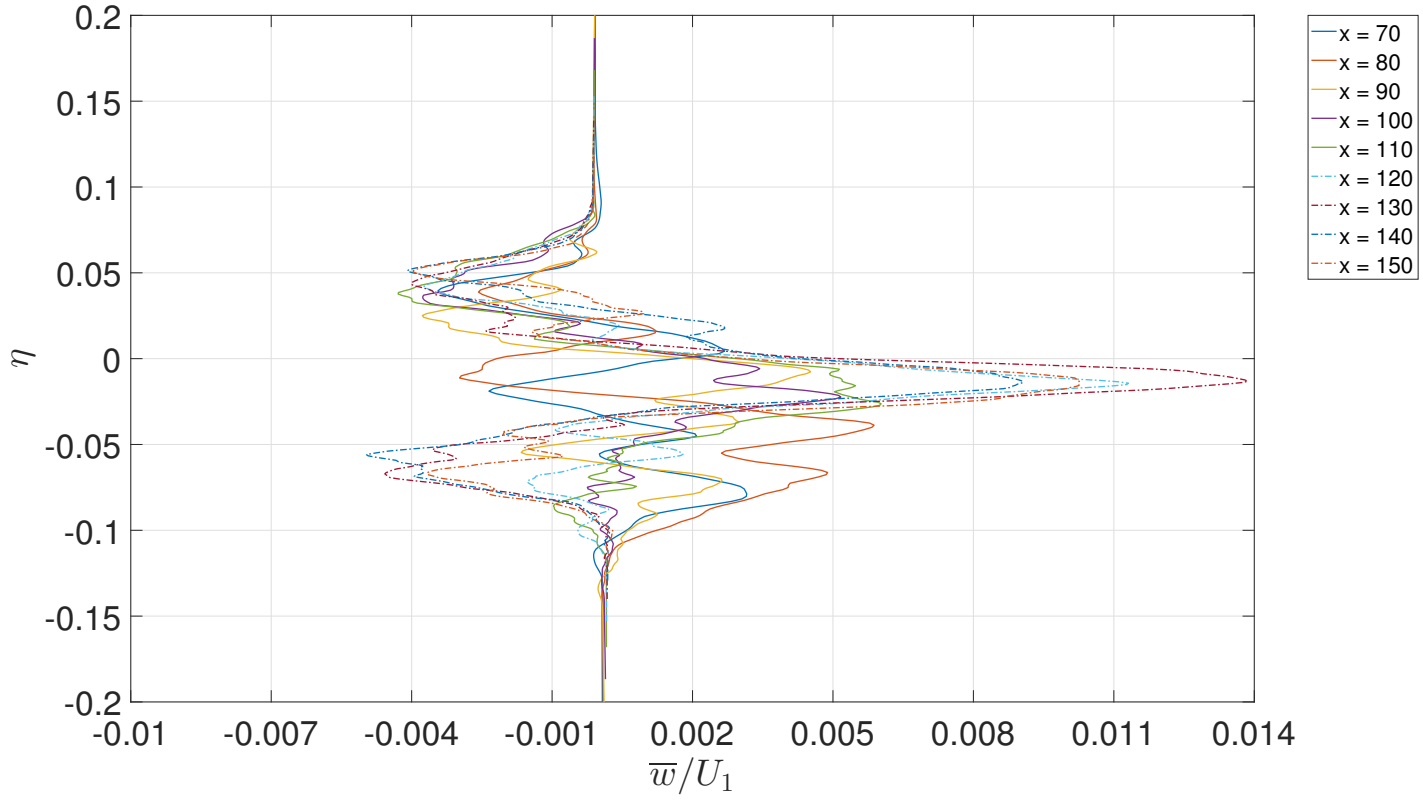

Figure 4.15: Mean spanwise velocity profiles at different x locations as a function of η.

4.5.2 Comments

The following comments can be made about figures 4.13 to 4.15 :

- in figure 4.13, the profiles of the mean streamwise velocity measured at various x collapse and the self-similarity is very good, except on the left side where the curves differ a little ;
- in figure 4.14, the self-similarity is quite poor. Let us remark however that the differences between the different curves are of the same order of magnitude for $\overline{u}$ and $\overline{v}$ but they appear amplified on the graph of $\overline{v}$ since its magnitude is significantly smaller than the one of $\overline{u}$. The shape of these profiles, which is the same for the different x locations, is representative of the entrainment of the fluid outside of the shear layer. In the upper region, the velocity is slightly positive so that the fluid at this place is note entrained in the layer. Then, around $\eta = 0$, there is an important peak of negative velocity and the rate of entrainment in this region is large. Going down a bit in the domain, velocity quickly becomes positive, reaches a peak value and then decreases. Note that velocity remains largely positive in the lower region while in the upper region, it tends towards zero. This shows that the layer develops preferentially in the low-speed stream region ;
- in figure 4.15, the values of $\overline{w}$ are small and they would tend to zero if they were averaged over a longer period. It is therefore normal to observe no self-similarity.

4.6 Covariances of the Reynolds stress tensor

4.6.1 Graphs

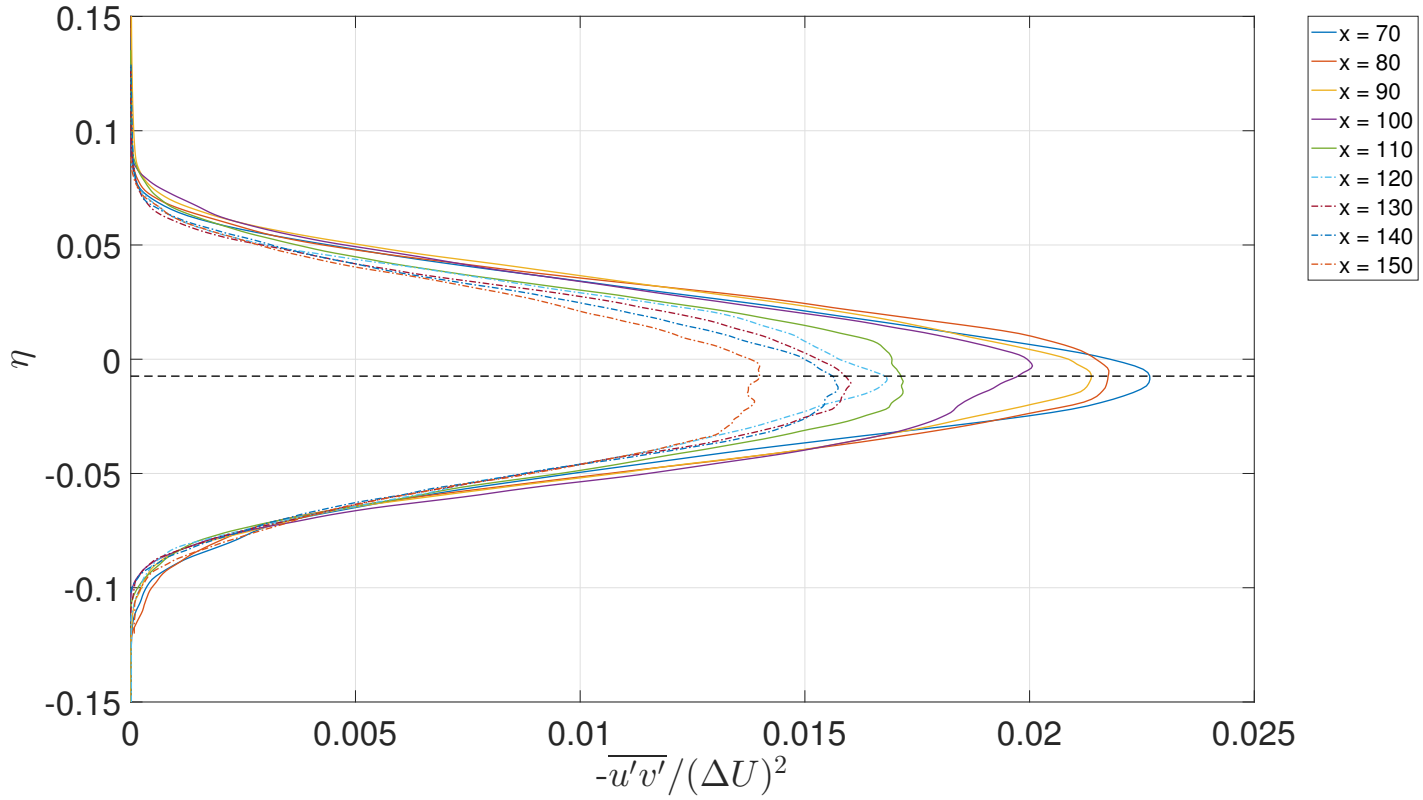

Figure 4.16: Covariance of the streamwise and transverse velocity fluctuations at different x locations as a function of η. The position of the dividing streamline is shown by the black dash line.

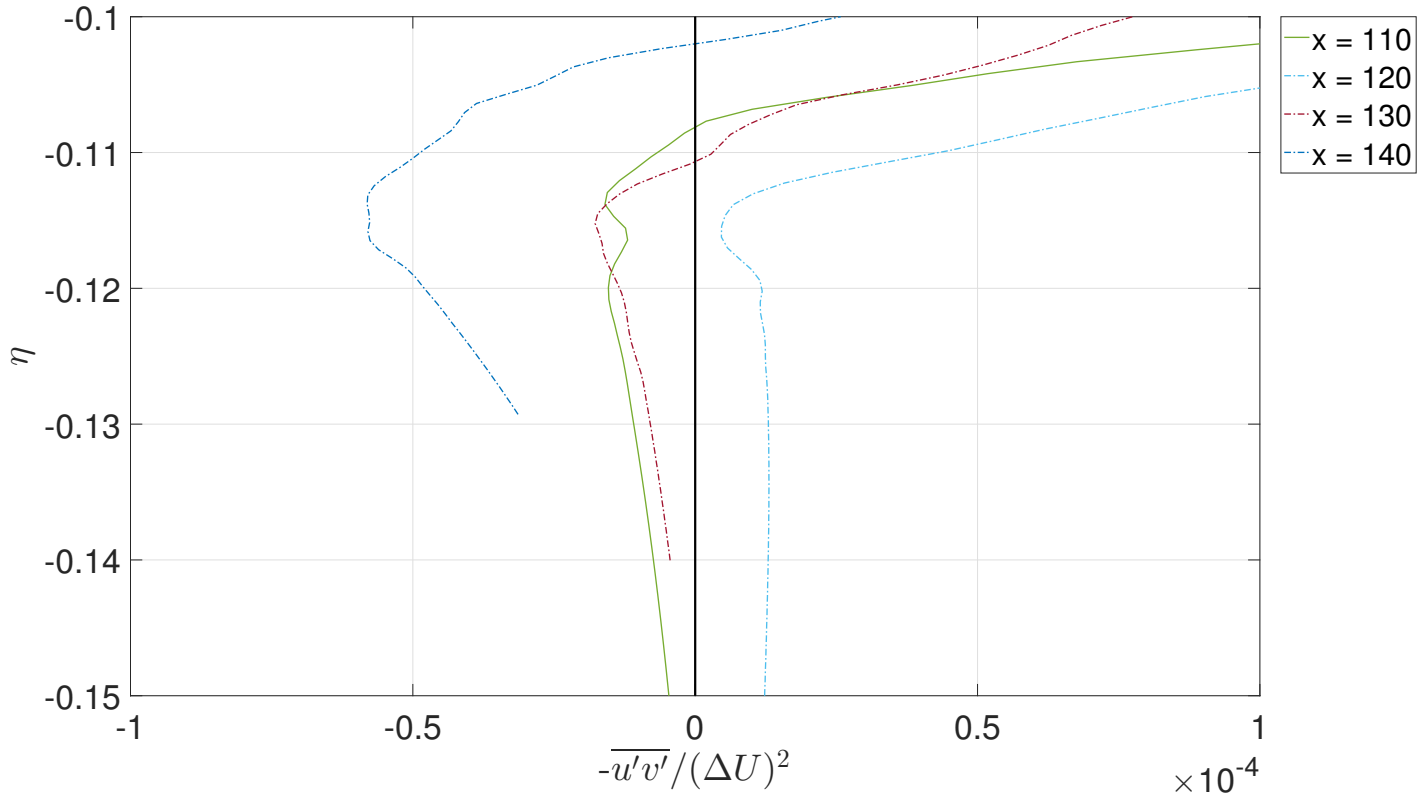

Figure 4.17: Zoom on figure 4.16 to show negative values of the turbulent shear stress.

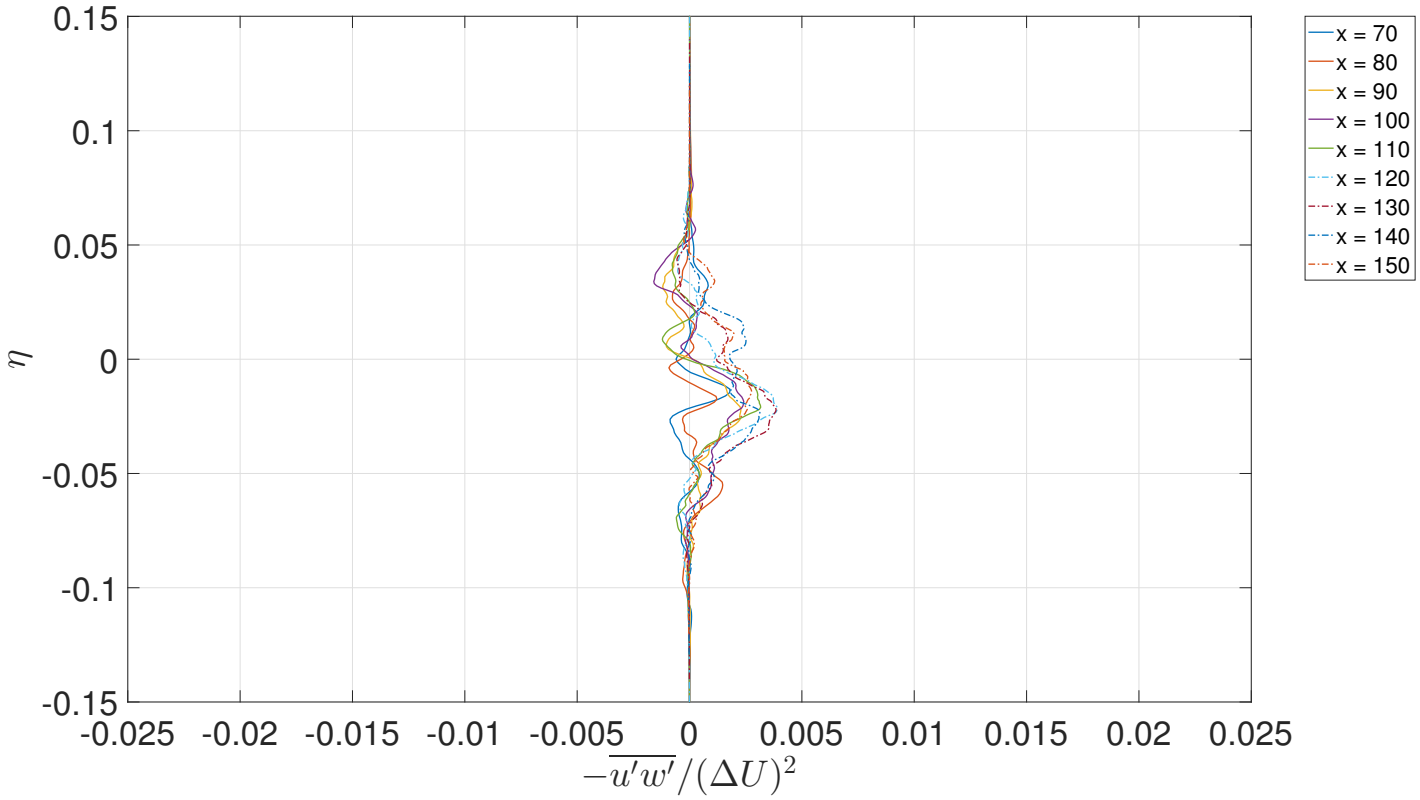

Figure 4.18: Covariance of the streamwise and spanwise velocity fluctuations at different x locations as a function of η.

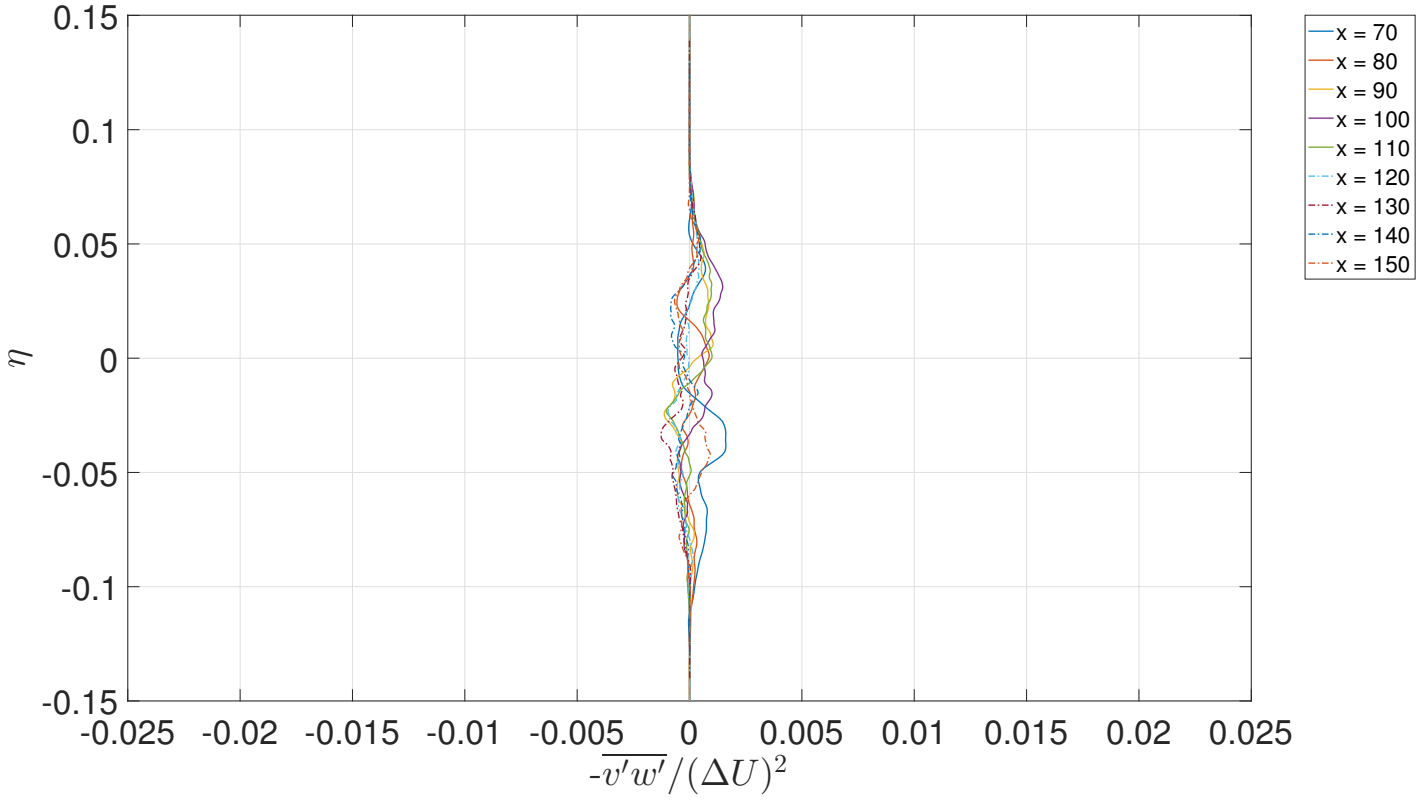

Figure 4.19: Covariance of the transverse and spanwise velocity fluctuations at different x locations as a function of η.

4.6.2 Comments

The following comments can be made about figures 4.16 to 4.19 :

- in figure 4.16, the term $-\overline{u'v'}$, which is very important as it represents the intensity of the modeled turbulent stresses, is plotted. On this graph, the position of the dividing streamline
$$\eta^* = \frac{y^*}{x - x_0} = -0.0074$$
is also represented by the black dot line. This position is equal to the slope of the dividing streamline $\mathrm{d}y^*/\mathrm{d}x$ in the region considered (see section 4.8). It can be demonstrated mathematically that the turbulent shear stress is maximal on the dividing streamline [5] :
$$\left(-\overline{u'v'}\right)_{max} = \left(-\overline{u'v'}\right)^* \ .$$
This behavior is fairly well respected for the curves presented in figure 4.16.
The profiles in the potentially self-similar region are close to each other which confirms the hypothesis according to which the region between $x = 110$ and $x = 140$ is the region with the best self-similarity *in the sense of Brown and Roshko* ;

- in figure 4.17, a zoom was made on 4.16 to show negative values of the turbulent shear stress around the edges of the mixing layer. Although small in magnitude, these negative values could indicate a "backscatter" phenomenon in which a reverse flux of energy from small to large scales is observed. An explanation of the energy cascade in turbulence is briefly presented in section 4.9 ;

- in figures 4.18 and 4.19, the covariances including the spanwise velocity oscillate in the region of the centerline. In theory, the statistics about these quantities should tend towards zero. The oscillations could thus suggest that flow statistics are not yet fully converged even if the period T in which they are collected is quite large.

4.7 Variances of the Reynolds stress tensor

4.7.1 Graphs

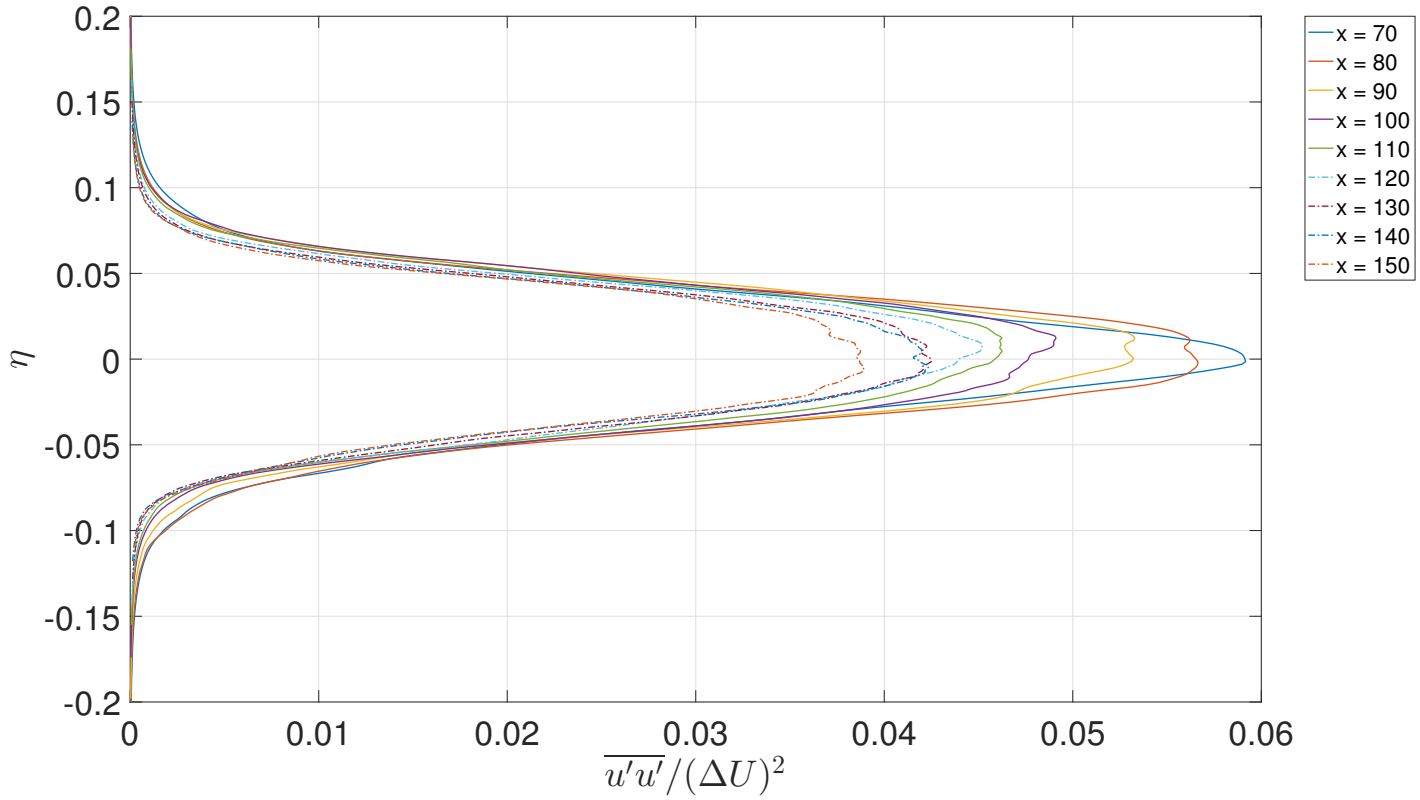

Figure 4.20: Variance of the streamwise velocity fluctuations at different x locations as a function of η.

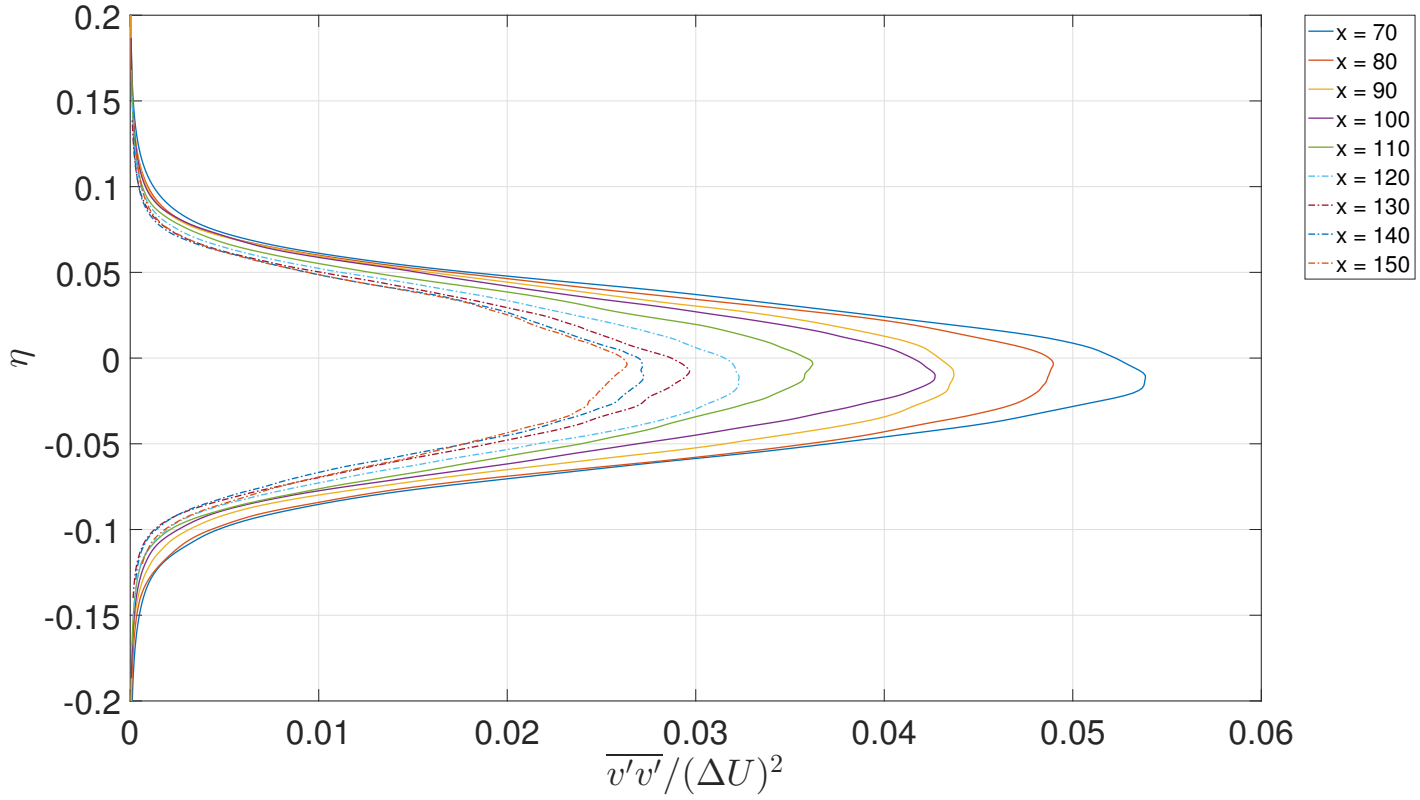

Figure 4.21: Variance of the transverse velocity fluctuations at different x locations as a function of η.

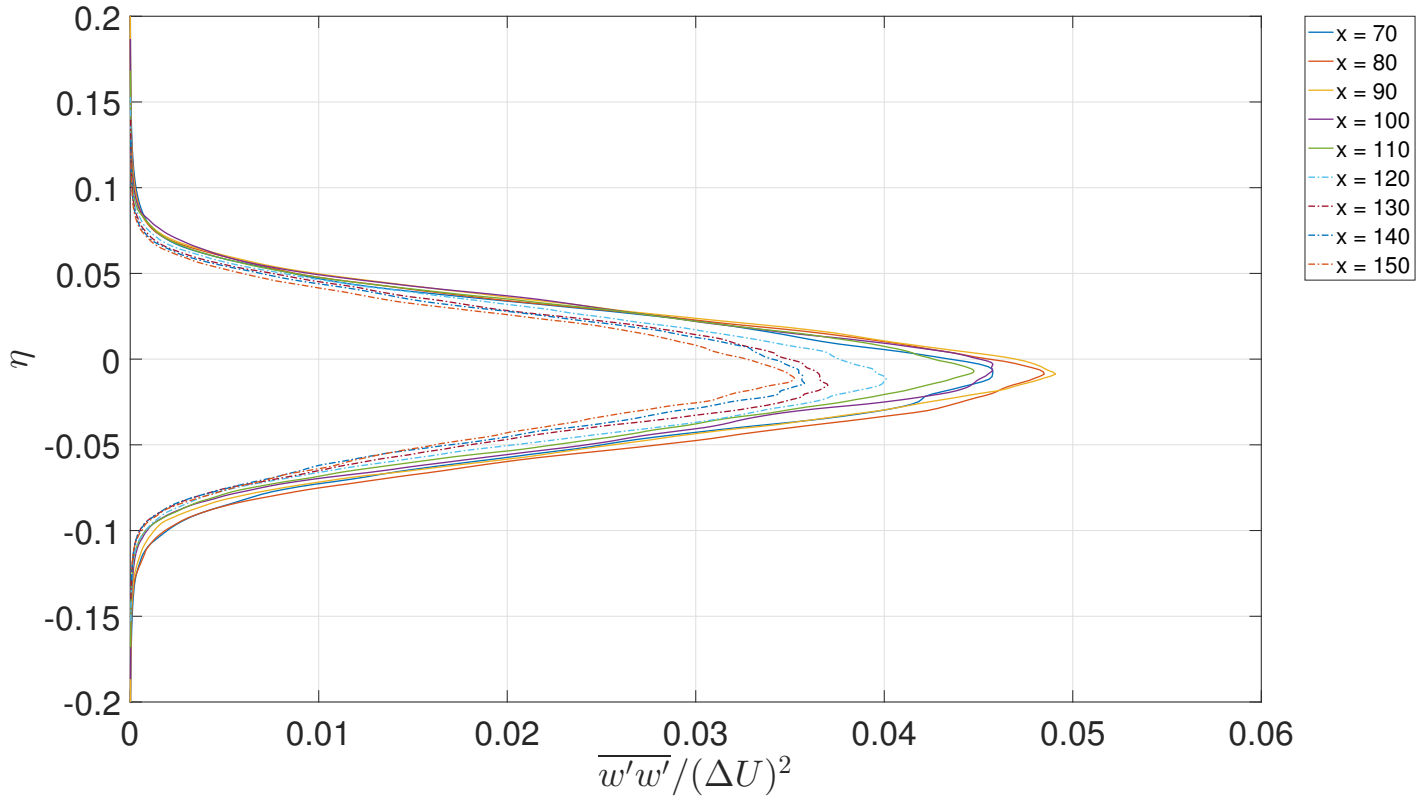

Figure 4.22: Variance of the spanwise velocity fluctuations at different x locations as a function of η.

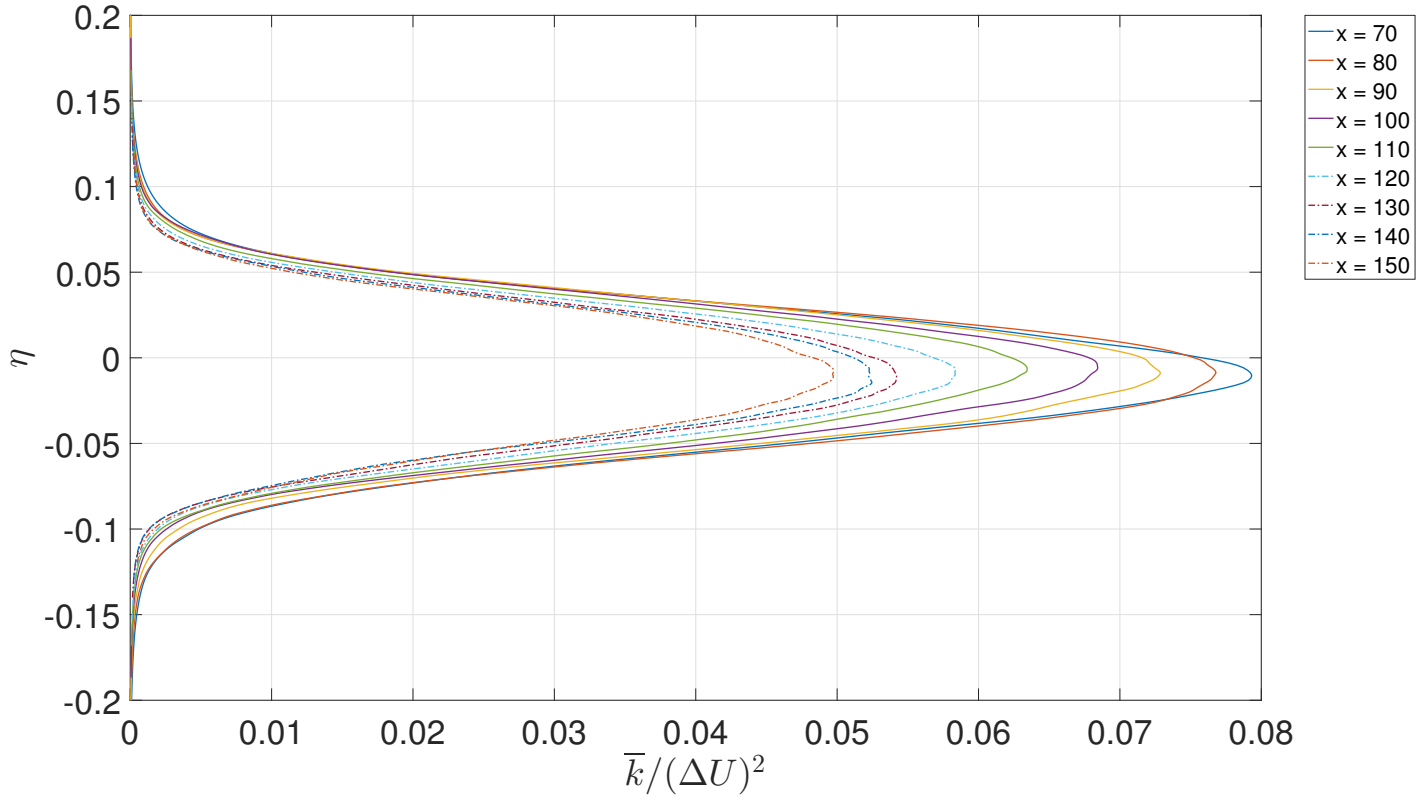

Figure 4.23: Turbulent kinetic energy at different x locations as a function of η.

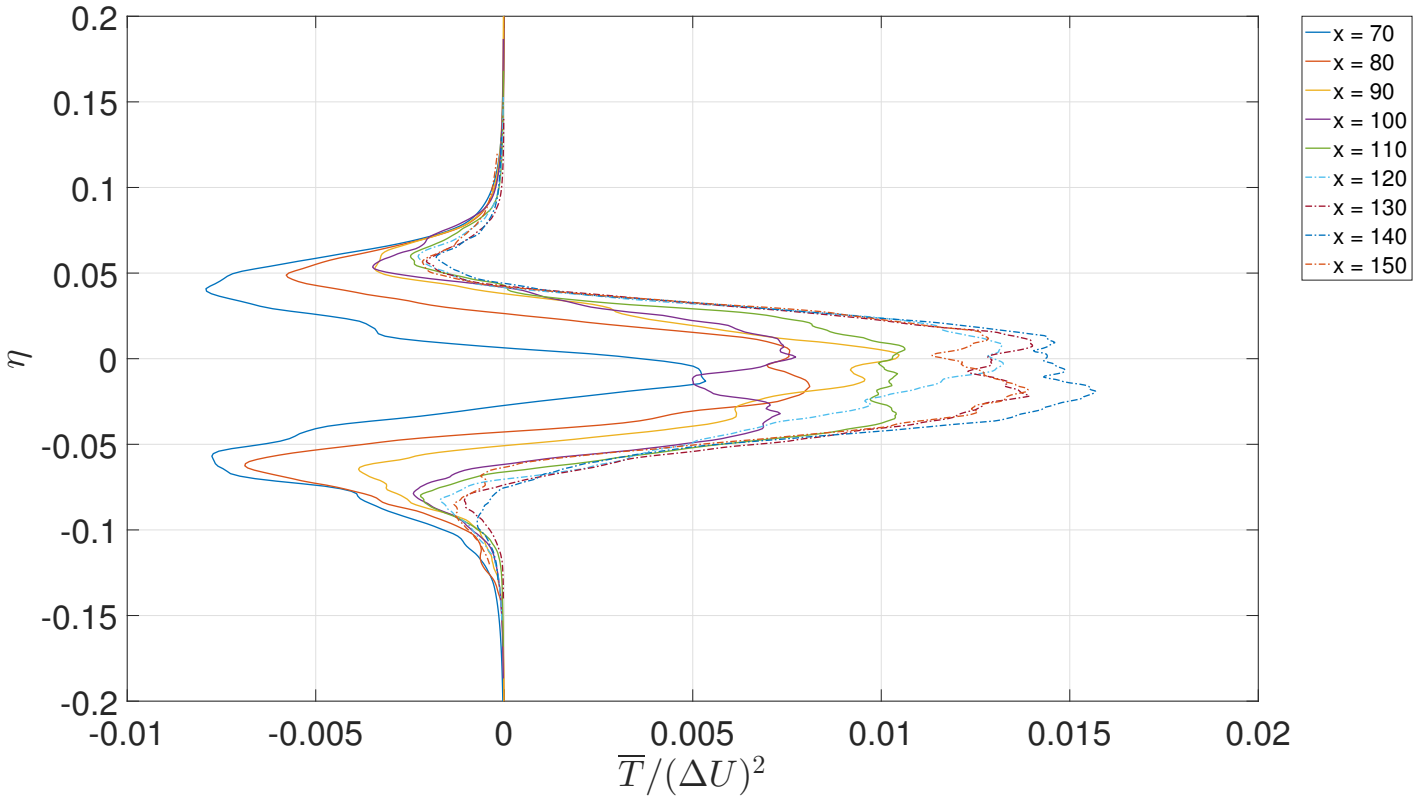

Figure 4.24: Townsend term at different x locations as a function of η.

4.7.2 Comments

The following comments can be made about figures 4.20 to 4.24 :

- in figures 4.20, 4.21 and 4.22, the self-similarity is "the best one" for the spanwise velocity variance and the worst one for the transverse velocity variance, as it is the case for the simulation in [33]. Rigorously speaking, one could say that there is no self-similarity because the curves don't collapse. The values of the maxima of the variances are decreasing with downstream distance ;
- in figures 4.23 and 4.24, the turbulent kinetic energy (TKE) $\overline{k} = 0.5 \cdot (\overline{u'u'} + \overline{v'v'} + \overline{w'w'})$ and the Townsend term $\overline{T} = \overline{u'u'} - \overline{v'v'}$ are shown. The TKE presents a "quite good" self-similarity and is maximal around the center of the layer, as expected. The Townsend term does not have such a good self-similarity. This is expected as this term is the difference of two terms that are of the same order of magnitude, hence small differences appear relatively larger. It is slightly negative just above and under the centerline and reaches a peak positive value around the center.

4.8 Thicknesses and growth rate

4.8.1 Graphs

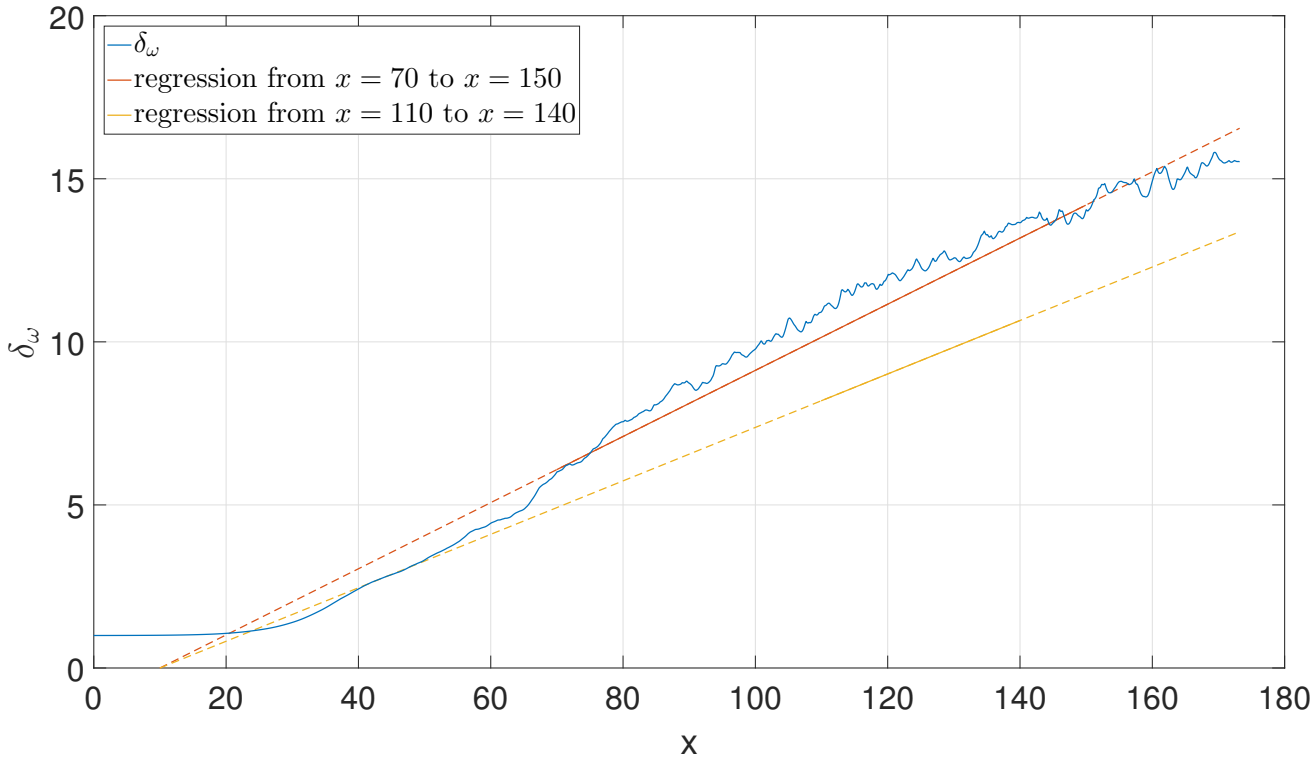

Figure 4.25: Streamwise evolution of the vorticity thickness with its linear regression approximation.

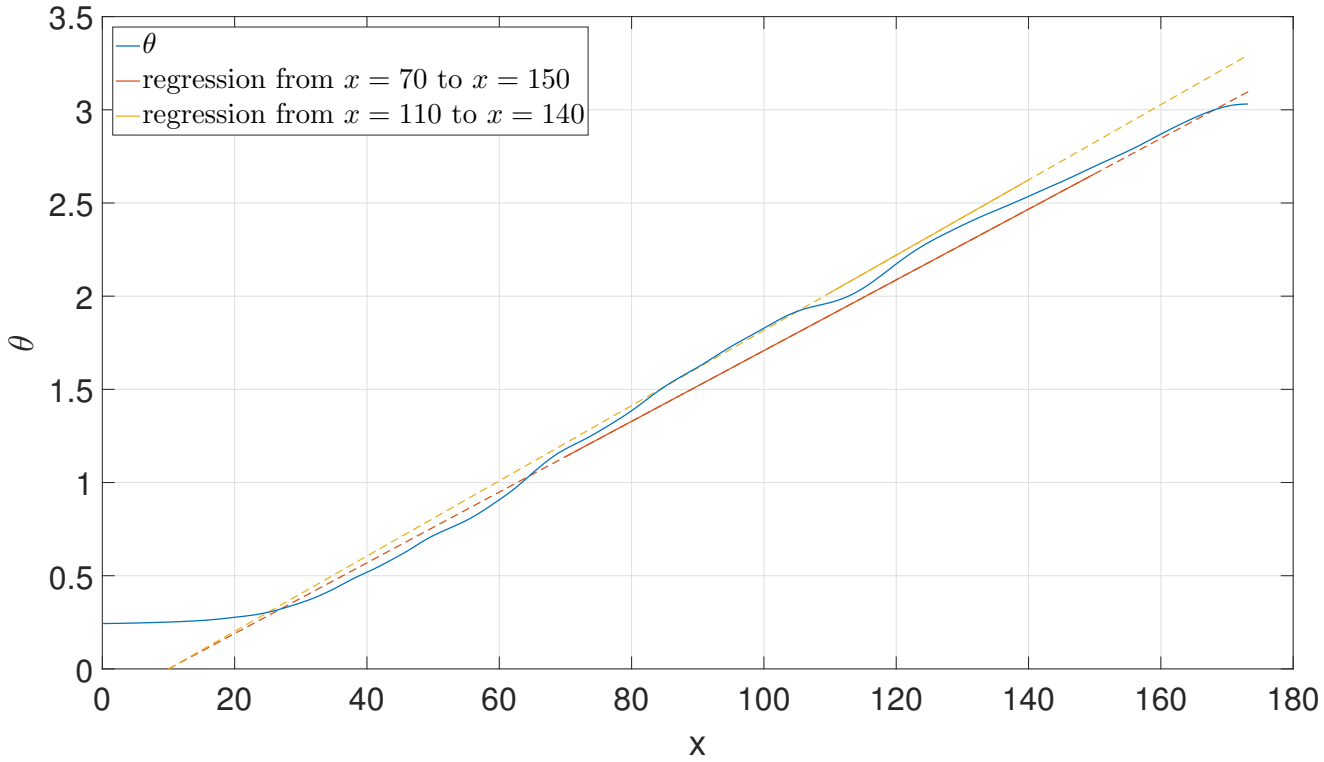

Figure 4.26: Streamwise evolution of the momentum thickness with its linear regression approximation.

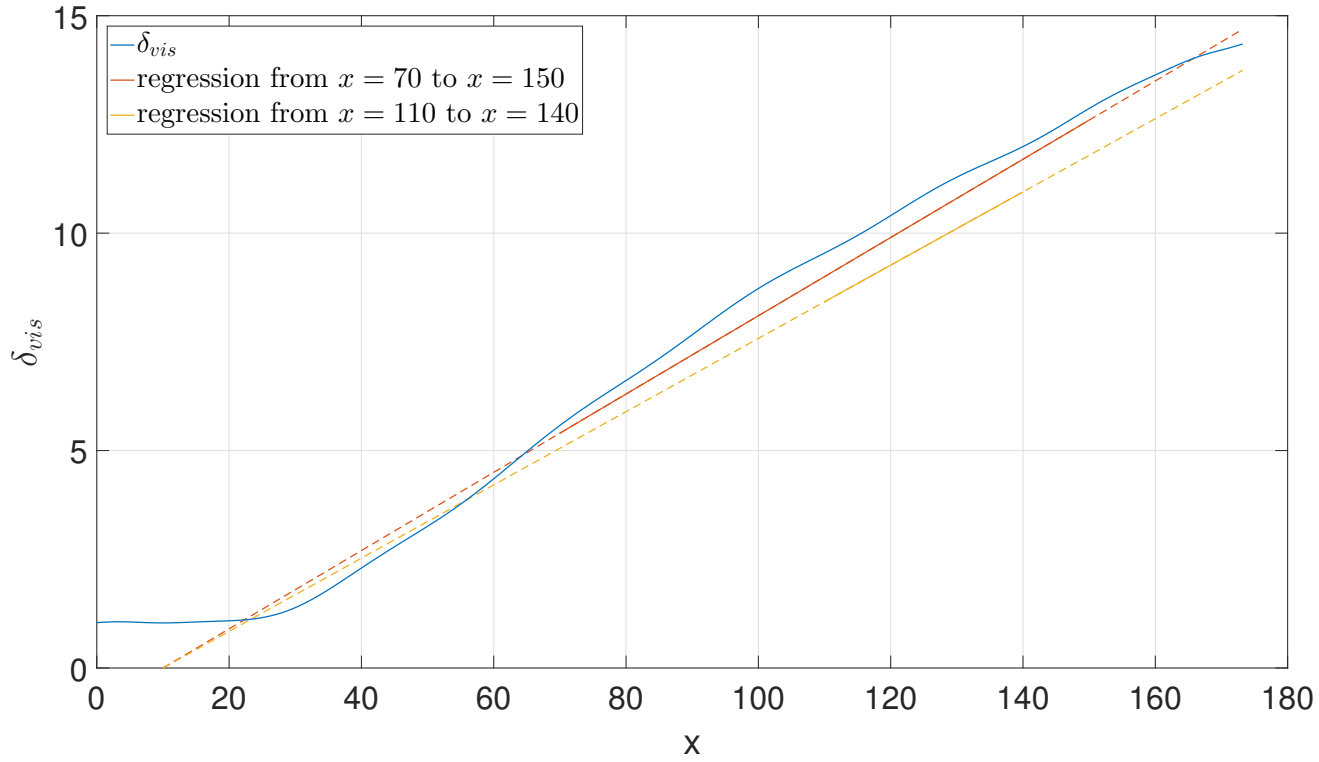

Figure 4.27: Streamwise evolution of the visual thickness with its linear regression approximation.

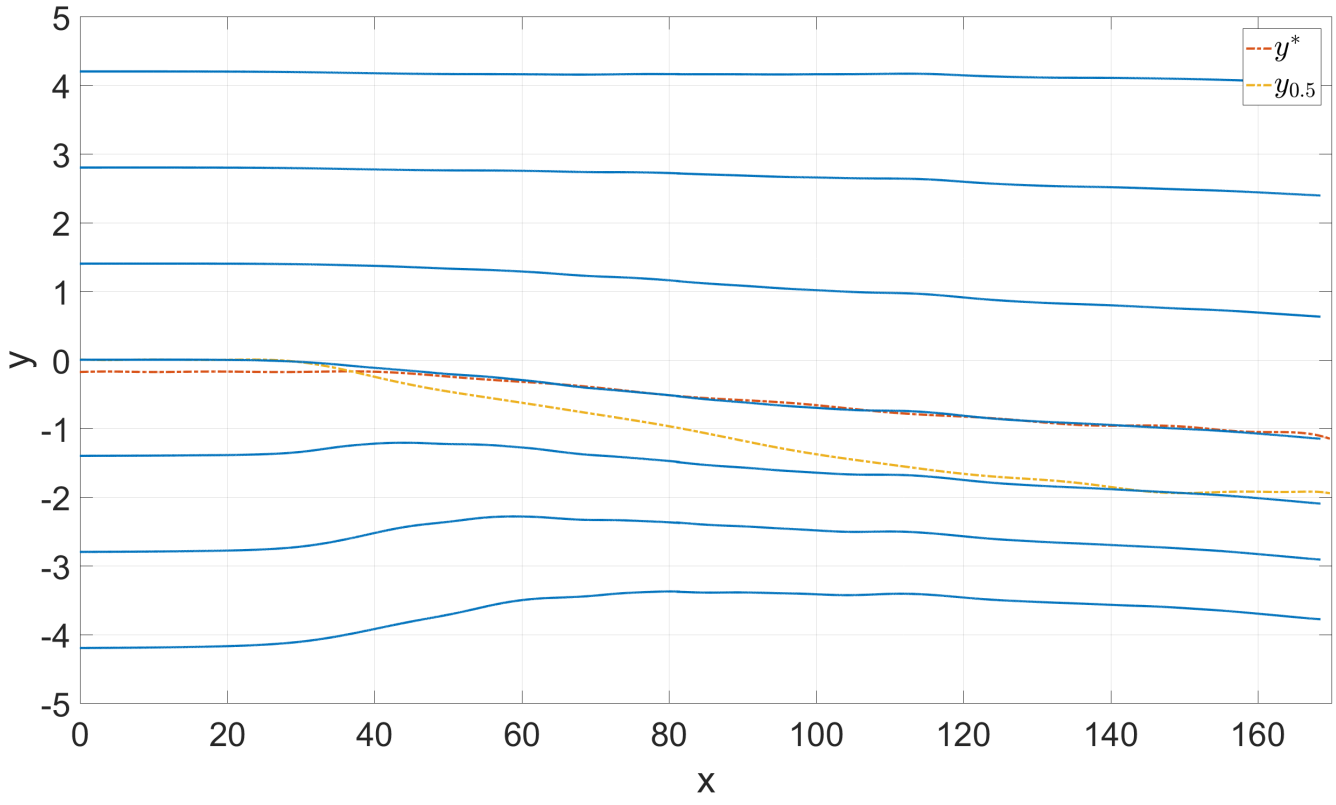

Figure 4.28: Some streamlines of the flow with the positions of the dividing streamline and $y_{0.5}$.

4.8.2 Comments

The following comments can be made about figures 4.25 to 4.28 :

- in figures 4.25, 4.26 and 4.27, the different definitions of the mixing layer thicknesses are drawn as a function of the streamwise distance. The red line on these figures represent the linear regressions computed on the data between $x = 70$ and $x = 150$ while the yellow line is for the data between $x = 110$ and $x = 140$. These lines were forced to go through the virtual origin and are extended by dash lines. The linear growth rate of the mixing layer is then quite pronounced, as expected. However, for δ_ω and δ_{vis}, the regression lines are shifted with respect to the curves by underestimating the values of these thicknesses.
  Between $x \simeq 60$ and $x \simeq 70$, there is a "bump" in the curves in the three figures which could mark the passage from the transition region to the fully-turbulent region. From $x \simeq 140$, the curves tend to move away from their linear evolution, which could reflect the influence of the outflow condition.
  Note finally that the fluctuations in the curve of δ_ω are due to its definition which involves a derivative ;

- in figure 4.28, the streamlines emanating from the beginning of the domain are represented. The shape of these streamlines are interesting. In the upper part, the fluid is slowly diverted to the bottom of the domain. In the lower part, the fluid is first directed towards the center before changing direction and following a direction parallel to that followed by the fluid in the upper part. Although different at the beginning, the dividing streamline then almost coincides with the streamline initially located at $y = 0$, which validates equation (1.24). The position where the mean velocity is equal to the convection velocity, $y_{0.5}$, descends more rapidly than $y*$ and the two lines are hence significantly different.

4.9 Energy spectrum

4.9.1 Introduction

By examining figures of section 4.2, it appears that turbulent motions are composed of structures being as large as the domain dimensions as well as much smaller structures. According to the theory of the turbulent energy cascade, kinetic energy is extracted from the mean flow by the large scale structures. These large structures, often compared to eddies, are unstable and break up. By doing this, they transfer their energy to smaller eddies and so on. The process continues until the eddies are so small that they become stable. At these small scales, the kinetic energy is dissipated under thermal energy by viscous action. To verify this theory, it might be interesting to visualize the energy of the turbulent fluctuations according to their size. This can be done by analyzing a turbulent velocity signal measured at a certain place in the flow in the spectral space. The appropriate tool is the Fourier analysis whose principle is recalled in appendix B.

Let u be the turbulent velocity signal considered. After computing its Fourier coefficients $\widehat{u}$, the energy associated to each of its modes is simply given by :

$$E = \widehat{u} \cdot \widehat{u}^* \ ,$$

where $\widehat{u}^*$ is the complex conjugate of $\widehat{u}$. This energy is made dimensionless by dividing it by the convection velocity squared :

$$E_{adim} = \frac{E}{U_c^2}.$$

The frequency is made dimensionless using the convective time $T_c = L_x/U_c$:

$$f_{adim} = f \cdot T_c.$$

The $-5/3$ power law of the energy spectrum in the inertial subrange is fundamental in the analysis of turbulent flows. This observation is based on the two Kolmogorov's similarity hypotheses. The first of this hypothesis states that the characteristics of the small-scale motions are uniquely determined by the viscosity ν and the dissipation rate of the turbulent kinetic energy ϵ. The second one assumes that for the motions of scale l contained in $l_0 >> l >> \eta$ where l_0 is the lenghtscale of the largest eddies and η is the Kolmogorov lengthscale, their statistics are uniquely determined by ϵ, independent of ν [30]. Dimensional analysis then gives the law in question :

$$E(\kappa) = C_K \epsilon^{2/3} \kappa^{-5/3} \ ,$$

where C_K is a universal constant and κ is the wavenumber proportional to the inverse of the size of the eddies.
κ is thus a spatial variable whereas the spectrum considered is a frequency spectrum. To compute $E(\kappa)$, it would have been necessary to measure the instantaneous velocity along a grid line and then make a FFT of that signal. However, by invoking Taylor's hypothesis of frozen turbulence, the spatial energy spectrum and the frequency spectrum give essentially the same information[1].

4.9.2 Graphs

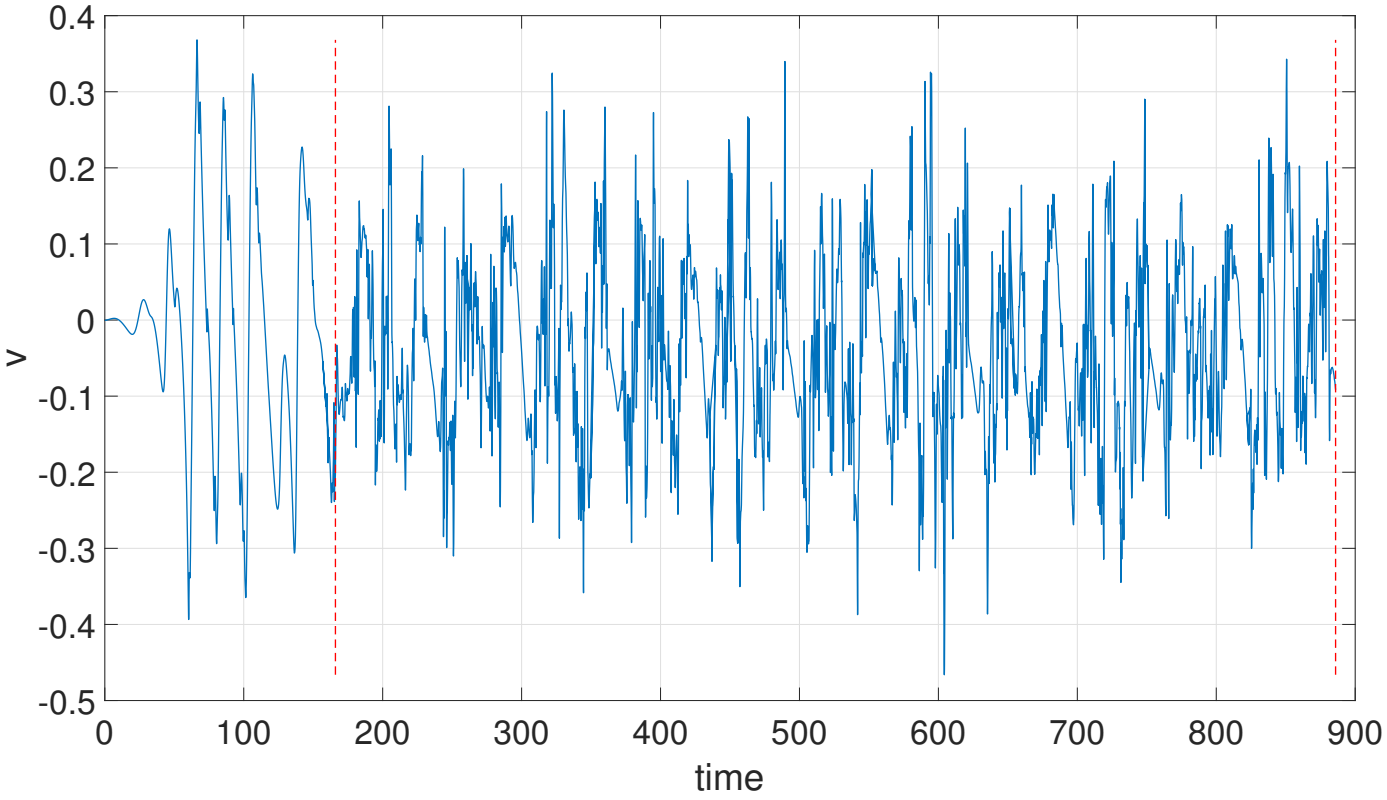

Figure 4.29: Transverse velocity signal measured at $(x,\ y) = (100,\ 0)$. The well-established turbulent part of the signal is identified by the red dash lines.

[1] If the turbulent intensity is not too high, this hypothesis assumes that «the velocity fluctuations at point x and time t is the same as that at time $(t - \tau)$ at point $(x - \epsilon)$ where $\tau = (x - \epsilon)/\overline{u}$»[19].

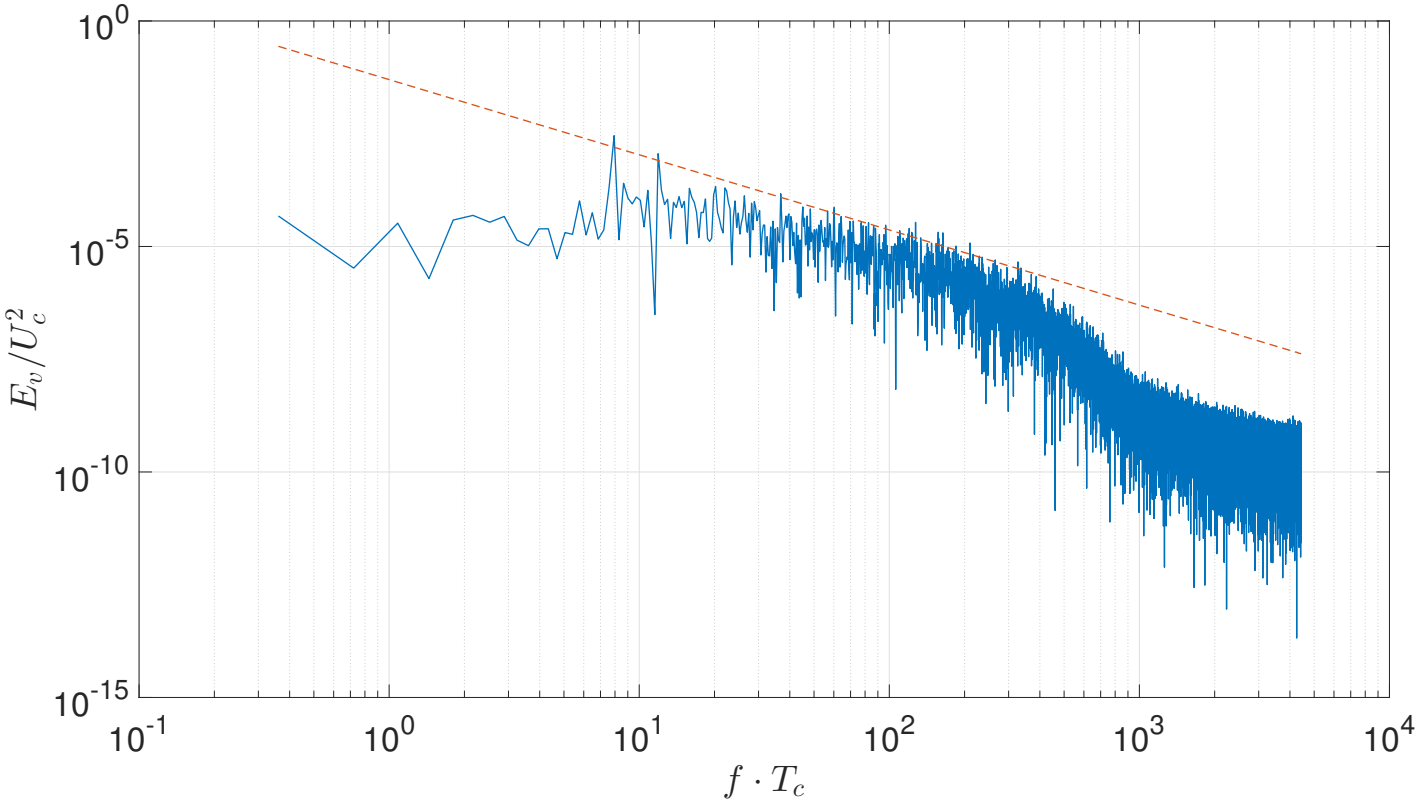

Figure 4.30: Frequency energy spectrum of the transverse velocity signal of figure 4.29. The $-5/3$ slope is also shown by the red dash line.

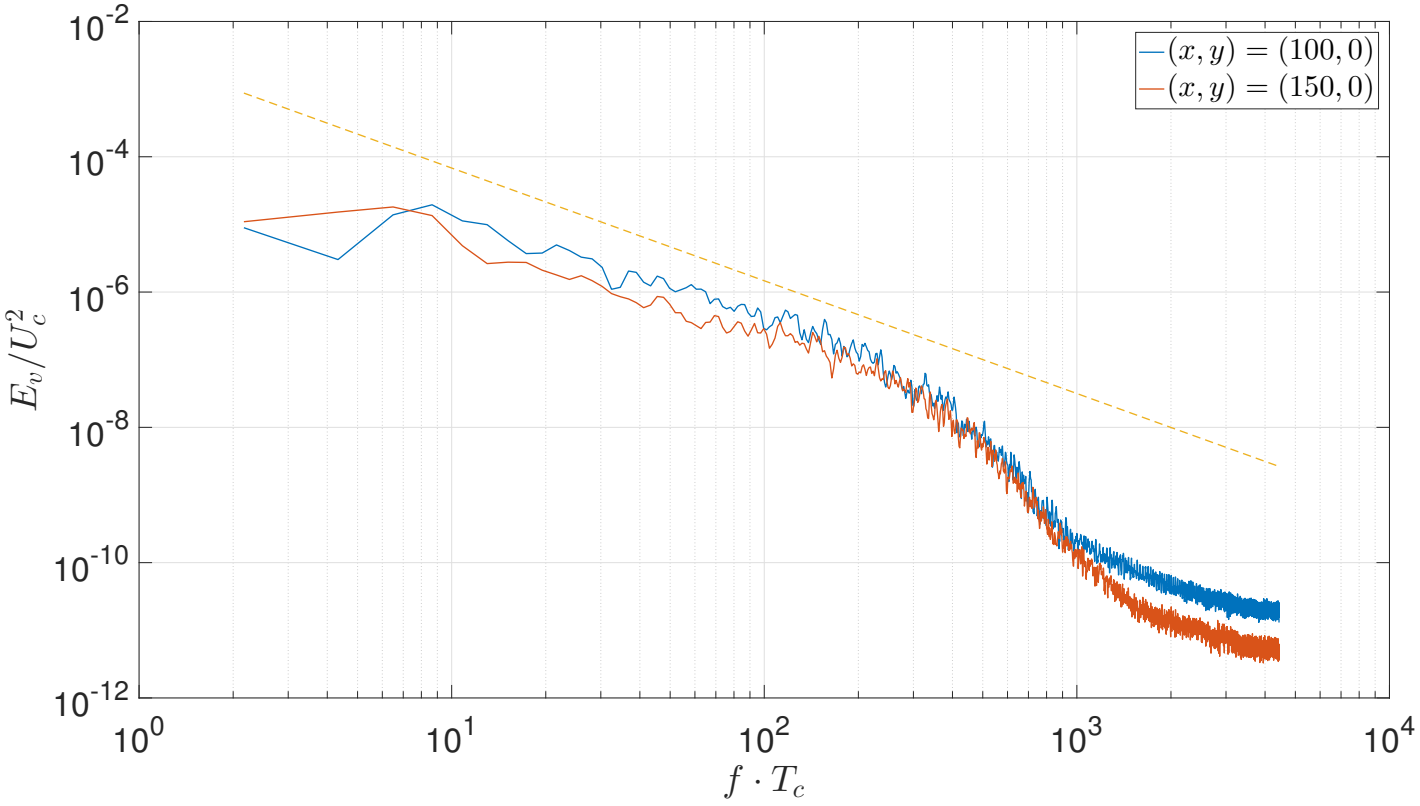

Figure 4.31: Smoothed frequency energy spectra of two transverse velocity signals obtained by power spectral density estimate. The $-5/3$ slope is also shown by the yellow dash line.

4.9.3 Comments

The following comments can be made about figures 4.29 to 4.31 :

- in figure 4.29, the velocity signal before the first vertical red dash line is composed mainly of low frequencies. During this time interval, the large structures initiated by the initial condition develop and become progressively unstable. Then, the flow becomes turbulent and higher frequencies are superimposed on the signal. Only the part of the signal between the two vertical red dash lines is used to compute the spectrum ;

- in figure 4.30, the spectrum of the velocity signal in figure 4.29 was obtained by computing the FFT of the last 24576 ($= 2^{13} \cdot 3$) data of the signal extracted from a total of 28458 data. The lowest frequencies, which correspond to the largest turbulent motions, contain the most energy, as expected. By examining higher frequencies, the energy progressively adopts the theoretical behavior of the inertial subrange, namely the "$-5/3$ decay". This result suggests that the subgrid scale model does not introduce any diffusion, and hence that the flow attained a fully-developed inertial range in this region of the spectrum. Then, at even higher frequencies, energy deviates from this $-5/3$ slope and decreases more rapidly, which shows the dissipation of the kinetic energy at small scales by the LES model. Finally, at the highest frequencies, the decay rate of the energy changes and becomes less important. This behavior is likely due to LES model itself. However, the level of energy at those highest frequencies is very small compared to that in the inertial range ;

- in figure 4.31, the frequency spectrum of figure 4.30 as well as a spectrum from another velocity signal are represented. These spectra contain the same information as the noisy spectrum on figure 4.30. They were smoothed using the PWELCH function of MATLAB. This function computes several Fast Fourier Transforms of the signal in different frequency windows. Then, it puts the results together and it averages. Here, eight windows containing each 3072 ($= 2^{10} \cdot 3$) data were used.
  One observes a very similar form for the two spectra. The energy of the most downstream signal is slightly lower than the energy of the other signal at all the scales except at the largest ;

- let us finally remark that for the simulation of the two-dimensional mixing layer in [5], some frequencies had a greater energy compared to that of their neighboring frequencies. These few frequencies had an associated wavelength of the order of the domain size. The authors of [5] concluded that "cavity waves" related to the size of the domain existed and therefore slightly perturbed the results. This phenomenon seems absent in three dimensions because no dominant frequency emerges from the energy spectra.

4.10 Convergence

4.10.1 Graphs

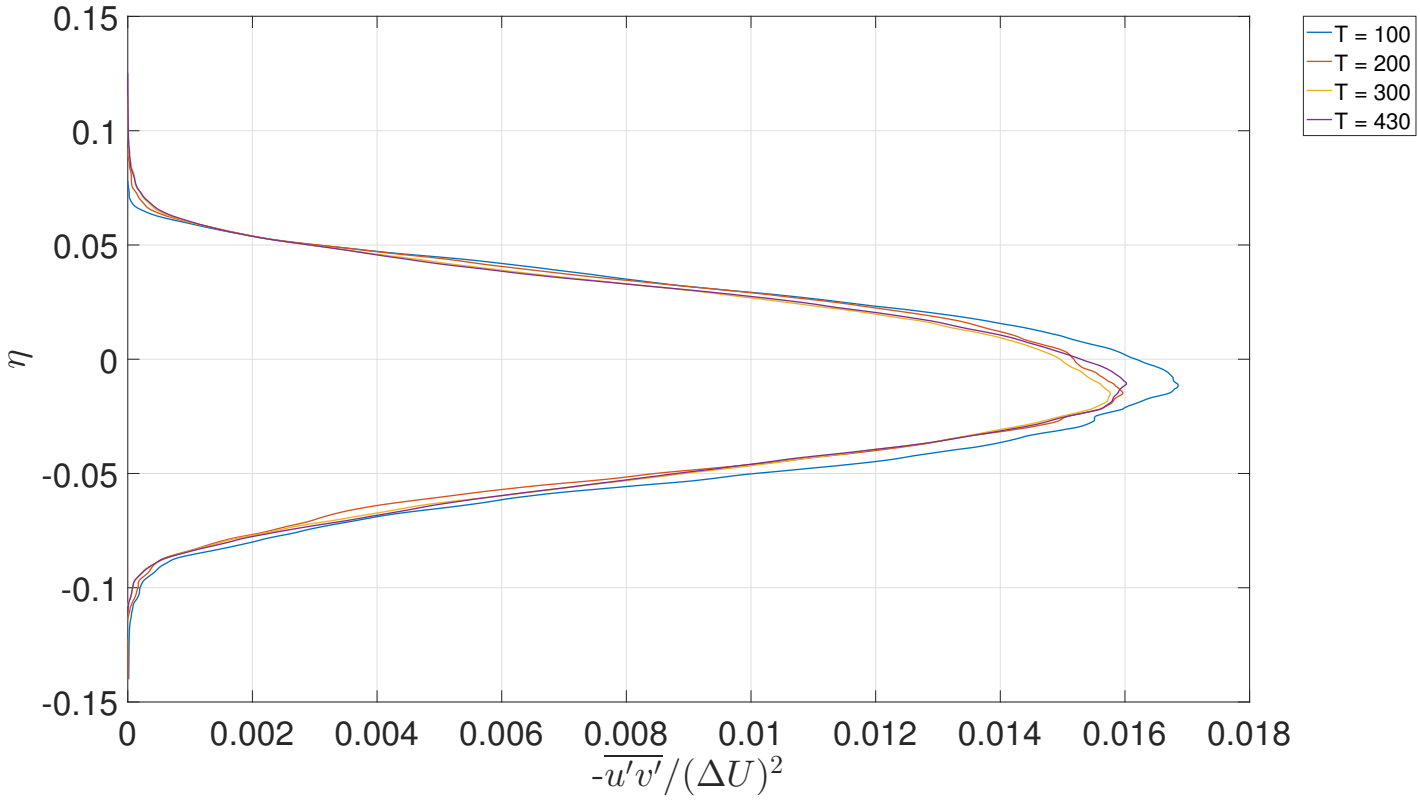

Figure 4.32: Covariance of the streamwise and transverse velocity fluctuations at x = 130 for different statistics periods T.

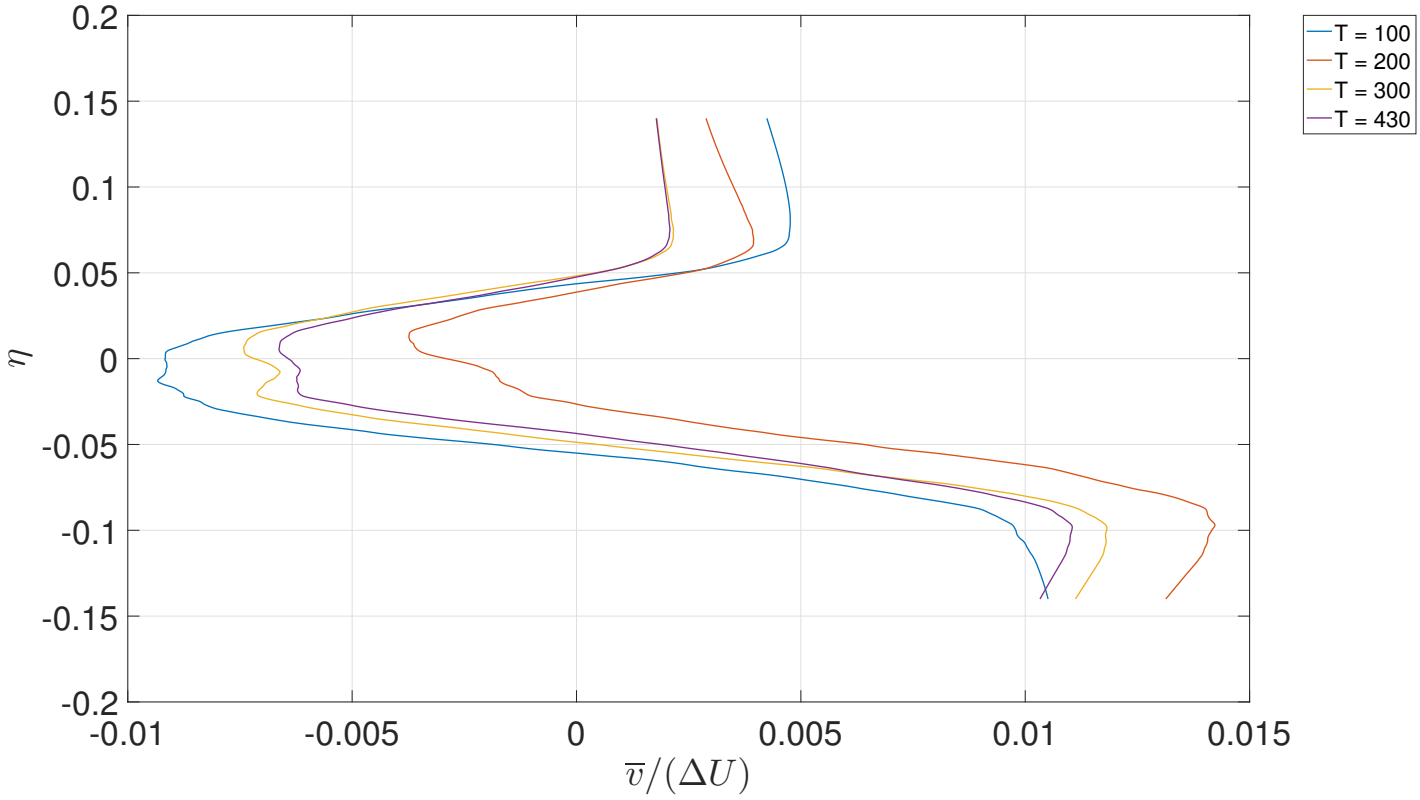

Figure 4.33: Mean transverse velocity at x = 130 for different statistics periods T.

4.10.2 Comments

The following comments can be made about figures 4.32 to 4.33 :

- in figure 4.32, the curve after a period $T = 100$ is not converged. The one after $T = 200$ tends towards the last two curves but by examining carefully the curve, one sees that it presents some irregularities in certain points which have been smoothed by increasing the period in which the statistics were collected. A minimum period of $T = 300$ was therefore necessary to obtain adequate statistics ;
- in figure 4.33, increasing the period over which the statistics are collected gives different curves which seem to converge towards a single curve after $T = 300$. However, this convergence is not complete and an increase in the statistics period may be necessary to achieve better convergence. Moreover, the covariances including the spanwise velocity fluctuations (figures 4.18 and 4.19) are not yet fully converged, as mentioned in section 4.6 ;
- from these observations, the following conclusion can be made. Although the statistics are probably not fully converged, the period of $T = 430$ considered is sufficient to obtain adequate results. It is also likely that the increase in the period, as large as it may be, will not make the profiles perfectly self-similar.

4.11 Comparison

The choice of the velocity ratio U_1/U_2 was made in order to be able to compare some results of the numerical simulation with experimental results of Brown and Roshko of 1974 [11] (see section 1.3 for more details). The velocity profiles at different streamwise locations obtained from traverse Pitot tube measurements is compared to the profiles of the simulation in figure 4.34. The results are in quite good fit.

The growth rates of the two situations are also compared in table 4.2 on the entire turbulent region considered (from $x = 70$ to $x = 150$) and on the self-similar region (from $x = 110$ to $x = 140$). The growth rates of the vorticity and momentum thicknesses are close to those measured by Brown and Roshko experimentally. For the vorticity thickness, the best growth rate (with a relative error of about 7%) with respect to [11] is obtained by considering the self-similar region. For the momentum thickness, it is the contrary (with a relative error of about 3%). The first source of differences between the two results is obviously the inevitable inaccuracies in the laboratory measurements. Then, the simulation characteristics can introduce other errors. Contrary to what one might think, these errors are probably not the result of the choice of the intensity of the turbulent perturbations superimposed on the incoming vorticity profile (see section 3.4). Indeed, in [3], several levels of white noise inlet perturbations were added to the velocity and it has been demonstrated that «whatever the perturbation amplitude studied, the same expansion rate is recorded in the LES results». The shape of the incoming velocity profile may however have an influence on the growth rate of the mixing layer, as it was shown by [35].

Finally, the normalized maximal turbulent shear stress is compared in table 4.3 for the different regions identified in figure 4.10 and for the entire region considered. As shown in figure 4.10, the mean between $x = 110$ and $x = 160$ is closest to the experimental value (with a relative error of about 5%).

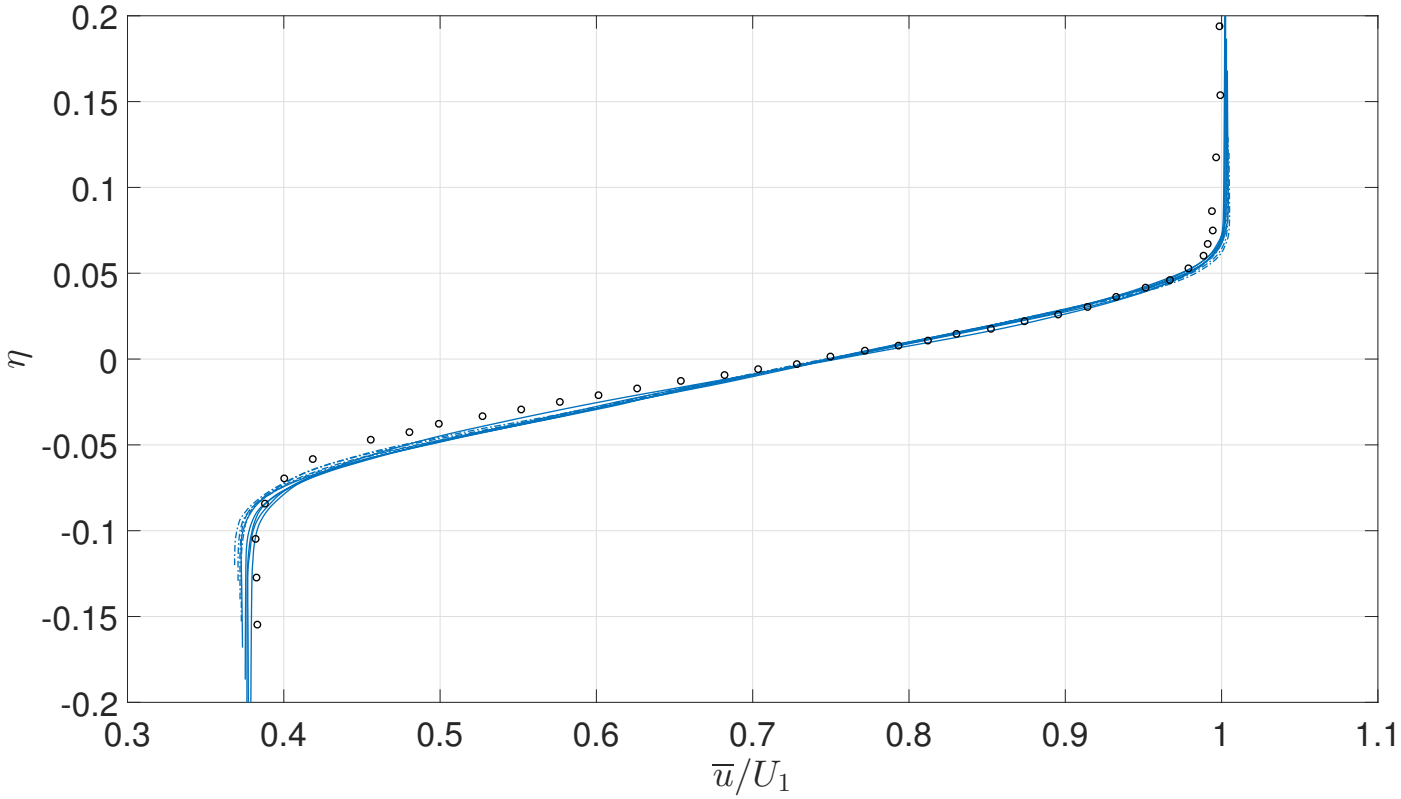

Figure 4.34: Mean streamwise velocity profiles at different x locations as a function of η and the experimental data from [11] (black dots).

		$\mathrm{d}\delta_\omega/\mathrm{d}x$	$\mathrm{d}\theta/\mathrm{d}x$
VPM	$x = 70 \rightarrow 150$	0.1014	0.0190
	$x = 110 \rightarrow 140$	0.0820	0.0202
B&R [11]		0.088	0.0184

Table 4.2: Comparison of the growth rates between the simulation and the experiment of [11].

		$\left(-\overline{u'v'}/(\Delta U)^2\right)_{max}$
VPM	$x = 70 \rightarrow 150$	0.0184
	$x = 110 \rightarrow 140$	0.0164
	$x = 110 \rightarrow 160$	0.0155
B&R [11]		0.0148

Table 4.3: Comparison of the maximal turbulent shear stress between the simulation and the experiment of [11].

Conclusions and perspectives

Conclusions

The subject of this master thesis was the numerical simulation and the study of a *spatially-developing incompressible three-dimensional turbulent mixing layer*. The simulation was carried out by means of an in-house CFD code which relies on the vorticity-velocity formulation of the incompressible Navier-Stokes equations. The method takes advantage of the stability of the Lagrangian formulation for the advection of the vorticity field carried by particles. An underlying grid is also present to resolve the Poisson equation for the velocity and evaluate the differential operators. The two approaches communicate via high order interpolation schemes. The turbulent character of the flow is handled by an LES Regularized Variational Multiscale (RVM) model.
The boundary conditions implemented in the code were slightly adapted to match the desired situation. Moreover, a Gaussian vorticity slab, corresponding to a hyperbolic tangent velocity profile, was chosen as the initial condition and was inserted at the inflow at each time step. Some perturbations were superimposed on this profile in order to accelerate the development of the mixing layer towards its turbulent state.

The main objective of the dissertation was to create an accurate simulation on quite a large computational domain and at high Reynolds number. On the one hand, compared to the references consulted, the accuracy of the simulation is undoubtedly of high quality. By choosing a lower initial Reynolds number, a DNS might even have been considered. The Reynolds number is also higher than in previous studies. On the other hand, the length of the domain is smaller than those in the references. This is explained by the finer resolution of the present mesh and by the higher value of the ratio between the length and the width. This first objective has therefore been fulfilled even if carrying out a simulation over a longer domain would be interesting.

Concerning the results, the different views showed a highly three-dimensional turbulent flow with a mixing layer growing in thickness with downstream distance. With the value of the Reynolds number and the perturbations, the transition to turbulence is quite fast and the fully-turbulent region of the flow occupies almost half of the domain. Before this region, the development of the Kelvin-Helmholtz instabilities which lead to the roll-up of the spanwise vortices appears, as well as the secondary streamwise structures. Thanks to the high resolution of the simulation, the small scale turbulent motions can clearly be identified.
The mean streamwise velocity profile has a very good self-similarity and the linear growth rate of the various thicknesses is well respected. Moreover, this velocity profile and these growth rates are close to those measured by Brown and Roshko in their experiment [11]. The variances of the velocity fluctuations as well as the turbulent shear stress are not fully self-similar, unlike the two-dimensional simulation [5]. The covariances including the spanwise velocity fluctuations are not yet very small, which might indicate that the flow statistics are not yet fully converged. The question of whether the increase in the period in which statistics are collected can improve the self-similarity of the profiles remains open but it is likely that the perfect self-similarity will never be reached for the concerned quantities.
The analysis of the spectrum showed that the flow attained fully-developed turbulent state in

the studied region and that the multiscale subgrid-scale model does not introduce dissipation over a significant portion of the spectrum, leading to a quite large inertial range.
The second objective of the thesis, namely to assess the results given by the VPM code against classical results for the mixing layer, has thus also been achieved. However, more experimental and/or numerical results corresponding to the situation treated would be necessary to evaluate the results obtained rigorously.
The method used in the code is optimal for simulating a mixing layer. However, it is difficult to judge the effectiveness of the code in terms of computational resources because comparisons are lacking.

Perspectives
In a future study, it might be interesting to address the following elements :

- **Reynolds number** : it could be reduced by an order of magnitude so that the subgrid modeling acts less. Its value would still be sufficient for the flow to rapidly transition to turbulence ;
- **perturbations** : the perturbations on the incoming flow could be removed. The flow would then take longer to develop but the visualization and the study of the two-dimensional structures as well as the transition zone would be possible. The effect of the change in perturbation intensity could also be studied and the results compared with experimental results to see which level of perturbations best corresponds to reality ;
- **domain size and discretization** : the domain could be longer in order to have a larger fully-developed region. Furthermore, if the Reynolds number is decreased and the perturbations are removed, this increase in length could be necessary because the laminar and transition regions would be longer. As the SGS model would still be activated, a coarser resolution could be envisaged without disrupting the development of large scale motions ;
- **simulation time** : by decreasing the number of points, it would be possible to achieve a much greater number of convective times than that achieved here. A more advanced convergence study of the statistics would then be possible ;
- **incoming velocity** : the shape of the incoming velocity profile has a strong influence on the development of the flow towards turbulence. It would therefore be interesting to compare the hyperbolic tangent profile used with a profile taking into account the boundary layers of the splitter plate ;
- **flow visualization** : in order to highlight the coherent structures in the visualization of the flow, some vortex identification methods could be used, such as the Q-criterion or λ_2-criterion methods. The proper orthogonal decomposition (POD) could also be envisaged ;
- **statistics** : in addition to the one-point statistics examined in this dissertation, two-point velocity correlations could be interesting to obtain in order to measure the correlation distances in the turbulent flow ;
- **pressure field** : by resolving another Poisson equation with the appropriate boundary conditions, the pressure field could be recovered and then studied. Interesting results could possibly be found.

Bibliography

[1] D 'Ovidio A. "Coherent structures in turbulent mixing layers". PhD thesis. University of Leicester, 1998.

[2] Michalke A. "On the inviscid instability of the hyperbolic-tangent velocity profile". In: *Journal of Fluid Mechanics* (1964).

[3] Tenaud C. et al. "Large Eddy Simulation of a spatially developing incompressible 3D mixing layer using the $v - \omega$ formulation". In: *Computer and Fluids* (2005).

[4] CECI. *Consortium des Équipements de Calcul Intensif*. `http://www.ceci-hpc.be/`. Feb. 2016.

[5] Bailly Cédric and Carton de Wiart. Corentin. *Investigation numérique de la similarité d'une couche de cisaillement bidimensionnelle*. 2008.

[6] Speziale Charles G. "On the advantages of the vorticity-velocity formulation of the equations of fluid dynamics". In: *NASA* (1986).

[7] Yoder D.A., DeBonis J.R., and Georgiadis N.J. "Modeling of turbulent free shear flows". In: *NASA* (2013).

[8] Ahmed F. and Tanma A.S. "Similarity Solution Of Plane Turbulent Mixing Layer". In: *International journal of scientific and technology research volume 3* (2014).

[9] Jeffrez Lee Freeman. "On the growth rate of turbulent mixing layers: a new parametric model". PhD thesis. Faculty of California Polytechnic Sate University, 2014.

[10] Winckelmans G. *LMECA2853 - Turbulence*. 2015-2016.

[11] Brown G.L. and Roshko A. "On density effects and large structure in turbulent mixing layers". In: *Journal of Fluid Mechanics* (1974).

[12] Winckelmans G.S. *Vortex Methods*. 2007, Chapter 5 - Encyclopedia of Computational Mechanics.

[13] Tennekes H. and Lumley J.L. *A first course in turbulence*. MIT Press, 1972.

[14] Jiménez J. *Turbulence and vortex dynamics*. 2004.

[15] Mann J. "Wind field simulation". In: *Prob. Engng. Mech.* (1998).

[16] Williamson J.H. "Low-Storage Runge-Kutta Schemes". In: *Journal of Computational Physics* (1980).

[17] P. Koumoutsakos. "Multiscale Flow Simulations Using Particles". In: *Annu. Rev. Fluid Mech* (2005).

[18] Bricteux L. et al. "Assessment of multiscale models for LES: spectral behaviour in very high Reynolds number turbulence an cases with aircraft wake vortices". In: *Journal of Turbulence* (2007).

[19] Davidson L. *Fluid mechanics, turbulent flow and turbulence modeling*. 2017.

[20] Mojtaba Dehghan Manshadi. *Wind Tunnels and Experimental Fluid Dynamics Research*. In Tech, 2011. Chap. 12.

[21] Y. Marichal. “An immersed interface vortex particle-mesh method”. PhD thesis. Université catholique de Louvain, 2014.

[22] Rogers M.M. and Moser R.D. “The Three-Dimensional Evolution of a PLane Mixing Layer - Part1. The Kelvin-Helmholtz Roll-Up”. In: *NASA Technical Memorandum* (1991).

[23] Rogers M.M. and Moser R.D. “The Three-Dimensional Evolution of a PLane Mixing Layer - Part2. Pairing and Transition to Turbulence”. In: *NASA Technical Memorandum* (1992).

[24] Chatelain P. *LMECA2300 - Advanced Numerical Methods*. 2015-2016.

[25] Chatelain P and P. Koumoutsakos. “A Fourier-based elliptic solver for vortical flows with periodic and unbounded directions”. In: *Journal of Computational Physics* (2010).

[26] Chatelain P et al. “Billion vortex particle direct numerical simulations of aircraft wakes”. In: *Computer methods in applied mechanics and engineering* (2007).

[27] Chatelain P et al. “Large Eddy Simulation of Wind Turbine Wakes”. In: *Flow Turbulence Combust* (2013).

[28] Chatelain P et al. “Vortex methods applied to the large eddy simulation of wind turbine flows”. In: *Journal of Computational Physics* (2015).

[29] Chatelain P et al. “Vortex Particle-Mesh simulations of Vertical Axis Wind Turbine flows: from the blade aerodynamics to the very far wake”. In: (2016).

[30] Stephen B. Pope. *Turbulent Flows*. Cambridge University Press, 2000.

[31] Backaert S, Chatelain P, and Winckelmans G. “Vortex Particle-Mesh with Immersed Lifting Lines for Aerospace and Wind Engineering”. In: *Symposium on Particle Methods in Fluid Mechanics* (2015).

[32] Fu S. and Li Q. “Numerical simulation of compressible mixing layers”. In: *International journal of heat and fluid flows* (2006).

[33] Laizet S., Lardeau S., and Lamballais E. “Direct numerical simulation of a mixing layer downstream a thick splitter plate”. In: *Physics of fluid* (2010).

[34] Lloyd N. Trefethen. *Spectral Methods in Matlab*. SIAM, 2000.

[35] McMullan W.A., Gao S., and Coats C.M. “The effect of inflow conditions on the transition to turbulence in large eddy simulations of spatially developing mixing layers”. In: *International Journal of Heat and Fluid Flow* (2009).

[36] Yang W.B. et al. “Large Eddy Simulation of mixing layer”. In: *Journal of Computational and Applied Mathematics* (2004).

[37] Wang Y., Tanahashi M., and Miyauchi T. “Coherent fine scale eddies in turbulence transition of spatially-developing mixing layer”. In: *International journal of heat and fluid flows* (2007).

A | Linear stability theory

The goal of this appendix is to give an overview of the equations used to study the stability of a free shear flow. To do that, some perturbations are added to the flow. If these perturbations remain small, the flow is stable. But, if they grow such that the base flow moves far from its original state, then the flow is said to be unstable.
Let's assume a velocity field of the form :

$$\mathbf{u} = \mathbf{U} + \mathbf{u}' \ ,$$

just like in equation (1.6). Here, $\mathbf{U}$ is the velocity of the base flow and $\mathbf{u}'$ is an infinitesimal perturbation field superimposed on the base flow. It can be shown that the evolution equations for the perturbations are [14] :

$$\begin{aligned} \frac{\partial u_i'}{\partial x_i} &= 0, \\ \frac{\partial u_i'}{\partial t} + U_j \frac{\partial u_i'}{\partial x_j} + u_j' \frac{\partial U_i}{\partial x_j} &= -\frac{\partial \mathrm{P}}{\partial x_i} + \nu \frac{\partial^2 u_i'}{\partial x_j \partial x_j} - u_j' \frac{\partial u_i'}{\partial x_j}. \end{aligned} \tag{A.1}$$

The last non-linear term in equations (A.1) is neglected to linearize the equations about the equilibrium solution $\mathbf{U}$. The resulting linearized equations are linked to the rapid distortion theory (RDT). In this theory, it is assumed that the large scales of the flow are controlled by the linear processes due to the base flow instead of by the non-linear self-deformation produced by the fluctuations [14].
One makes the assumption of a parallel flow (the initial velocity profile of a mixing layer is a parallel flow) such that :

$$\mathbf{U} = (U(y),\ 0,\ 0).$$

Then, one takes the divergence of the momentum equation (A.1) and from this result, one substitutes the pressure in the momentum equation for v' to obtain :

$$\left[\left(\frac{\partial}{\partial t} + U(y) \frac{\partial}{\partial x} \right) \frac{\partial^2}{\partial y^2} - \frac{\mathrm{d}^2 U(y)}{\mathrm{d}y^2} \frac{\partial}{\partial x} - \nu \frac{\partial^4}{\partial y^4} \right] v' = 0. \tag{A.2}$$

Equation (A.2) is called the *Orr-Sommerfeld* equation and it governs the dynamics of the transverse velocity perturbation. To simplify the analysis, the case of an inviscid flow is often treated. The *Orr-Sommerfeld* equation then reduces to the *Rayleigh* equation.
Equation (A.2) is autonomous in time t and in the space coordinates x and z. The solution of this equation can thus be written as a superposition of normal modes :

$$v' = \widehat{v'}(y) \cdot e^{i(\kappa_x x + \kappa_z z - \omega t)} \ , \tag{A.3}$$

where κ_x and κ_z are the wavenumbers of the streamwise and spanwise perturbations, respectively, and ω is the complex angular frequency which can be expressed as $\omega = \kappa_x \cdot c$ with the wave propagation velocity c. Here, the temporal problem is considered. κ_x and κ_z are thus real and $\omega = \omega_r + i\omega_i$. The perturbation will then grows exponentially if $\omega_i > 0$ or equivalently if $c_i > 0$.

Injecting equation (A.3) into equation (A.2) without the viscous term, one obtains the following equation :

$$\left[(U(y)-c)\left(\frac{\partial^2}{\partial y^2}-k^2\right)-\frac{\mathrm{d}^2U(y)}{\mathrm{d}y^2}\right]\widehat{v'}=0 \tag{A.4}$$

in which $k^2=\kappa_x^2+\kappa_z^2$. In fact, with the inviscid Rayleigh equation, the amplification factor of the perturbations, given by $\kappa_x \cdot c_i$, will be maximal for $\kappa_z = 0$. Only the two-dimensional case has to be studied and the behavior of oblique waves, in which $\kappa_z \neq 0$, can be deduced from the analysis made for the two-dimensional situation.
Equation (A.4) can be seen as an eigenvalue problem for c. By prescribing the correct boundary conditions on $\widehat{v'}$ and the desired velocity profile for the base flow $U(y)$, one can resolve this problem for c by choosing various values of κ_x. In [2], this procedure is followed for the case of a hyperbolic tangent velocity profile of the form

$$U(y^*)=\frac{1}{2}[1+\tanh(y^*)]\ ,$$

where y^* is dimensionless. The result is that this profile is unstable for all dimensionless wavenumbers κ_x^* between 0 and 1 since the corresponding eigenvalues c_i are all positive. Moreover, the maximal amplification factor of the perturbations $(\kappa_x \cdot c_i)_{max}$ is found to correspond to the dimensionless wavenumber

$$\kappa_{x,max}^*=0.4446\ .$$

This streamwise wavenumber can be related to a dimensionless streamwise wavelength λ_x of the instability waves :

$$\lambda_{x,max}^*=\frac{2\pi}{\kappa_{x,max}^*}\approx 14.0\ .$$

This wavelength is the most unstable wavelength of the Kelvin-Helmholtz instability for a hyperbolic tangent velocity profile. For the dimensional velocity profile used in this dissertation

$$U(y)=U_c+\frac{\Delta U}{2}\tanh\left(\frac{2y}{\delta_{\omega_0}}\right)\ ,$$

this wavelength writes as a function of the initial vorticity thickness :

$$\lambda_{x,max}\approx 14.0\cdot\delta_{\omega_0}.$$

From this result, the corresponding spanwise wavelength associated to the most unstable mode is determined :

$$\lambda_{z,max}^*\approx 0.6\cdot\lambda_{x,max}^*.$$

Let's finally note that the theory presented above describes only the linear amplification of the vorticity waves of the Kelvin-Helmholtz instabilities and is restricted to the largest flow scales. Then, one observes a non-linear evolution during which the vorticty tends to concentrate by forming vortex blobs.

B | Fourier representation

Any discrete periodic function can be decomposed into a finite sum of trigonometric functions that represent the different modes describing the function in spectral space. This decomposition can be applied on a function depending on a space variable or a time variable. Here, the case of a time-dependent function is treated because the velocity signal to be analyzed varies over time and not over space.
Let U_j be the value of a discrete function U evaluated at a time t_j. U is periodic with a period T and is composed of n values U_j. The following relation can then be written :

$$t_j = j \cdot \frac{T}{n} = j \cdot \Delta t \quad \text{with } j = 0, 1, 2, ..., n-1.$$

The Fourier series of U is given by :

$$U_j = \sum_{p=-n/2}^{n/2} \widehat{U}_p \cdot e^{i\omega_p t_j} \quad j = 0, 1, 2, ..., n-1 \ ,$$

where is i the imaginary unit such that $i^2 = -1$ and

$$\omega_p = 2\pi f_p = 2\pi \frac{p}{T}$$

is the angular frequency associated to the Fourier mode p. The Fourier coefficients are computed thanks to the following relation :

$$\widehat{U}_p = \frac{1}{n} \sum_{j=0}^{n-1} U_j \cdot e^{-i\omega_p t_j}.$$

It can be shown that the coefficients $\widehat{U}_p$ and $\widehat{U}_{-p}$ are complex conjugates such that :

$$\widehat{U}_p = \widehat{U}_{p,R} + i \cdot \widehat{U}_{p,I} \ ,$$

$$\widehat{U}_{-p} = \widehat{U}_{-p,R} - i \cdot \widehat{U}_{-p,I} \ ,$$

where $\widehat{U}_{p,R}$ and $\widehat{U}_{p,I}$ are the real and complex parts of $\widehat{U}_p$, respectively. The computations of the Fourier coefficients can therefore be restricted to the modes going from $p = 0$ to $p = \frac{n}{2}$. The mode zero $p = 0$ is simply the mean of the function U over the time interval T. The last mode $p = \frac{n}{2}$ contains only a real part by definition in such a way that the Fourier representation of U contains the same amount of information than the original function U. This remark is illustrated by table B.1.
Finally, the cut-off frequency associated to the last mode is found to be equal to $f_{p,max} = \frac{1}{2\Delta t}$.

From a practical point of view, in MATLAB, the computation of the Fourier coefficients can be done by calling the function FFT. Two important remarks about this function :

1. to obtain the correct coefficients, one must divide the result by the length of the signal considered :

$$\widehat{U}_p = \text{FFT}(U)/n \ ;$$

p	$\widehat{U}_{p,R}$	$\widehat{U}_{p,I}$
0	×	
1	×	×
2	×	×
⋮		
$\frac{n}{2}-1$	×	×
$\frac{n}{2}$	×	

Table B.1: Fourier modes and the corresponding Fourier coefficients

2. it returns the coefficients from $p = 0$ to $p = \frac{n}{2}$ and then from $p = -\frac{n}{2} + 1$ to $p = -1$. So,

$$\widehat{U}_p = \left[\widehat{U}_0, \widehat{U}_1, \widehat{U}_2, ..., \widehat{U}_{n/2}, \widehat{U}_{-n/2+1}, \widehat{U}_{-n/2+2}, ..., \widehat{U}_{-1}\right].$$

C | Intermediate simulations

C.1 Simulation without incoming perturbations

The views presented in this section were obtained from a simulation without perturbations added to the incoming flow. The perturbations on the initial condition were present. Here are some parameters of the simulation :

- $(N_x,\ N_y,\ N_z) = (1024,\ 64,\ 64)$;
- $(L_x,\ L_y,\ L_z) = (134.4,\ 8.4,\ 8.4)$;
- $N_{procs} = 64$.

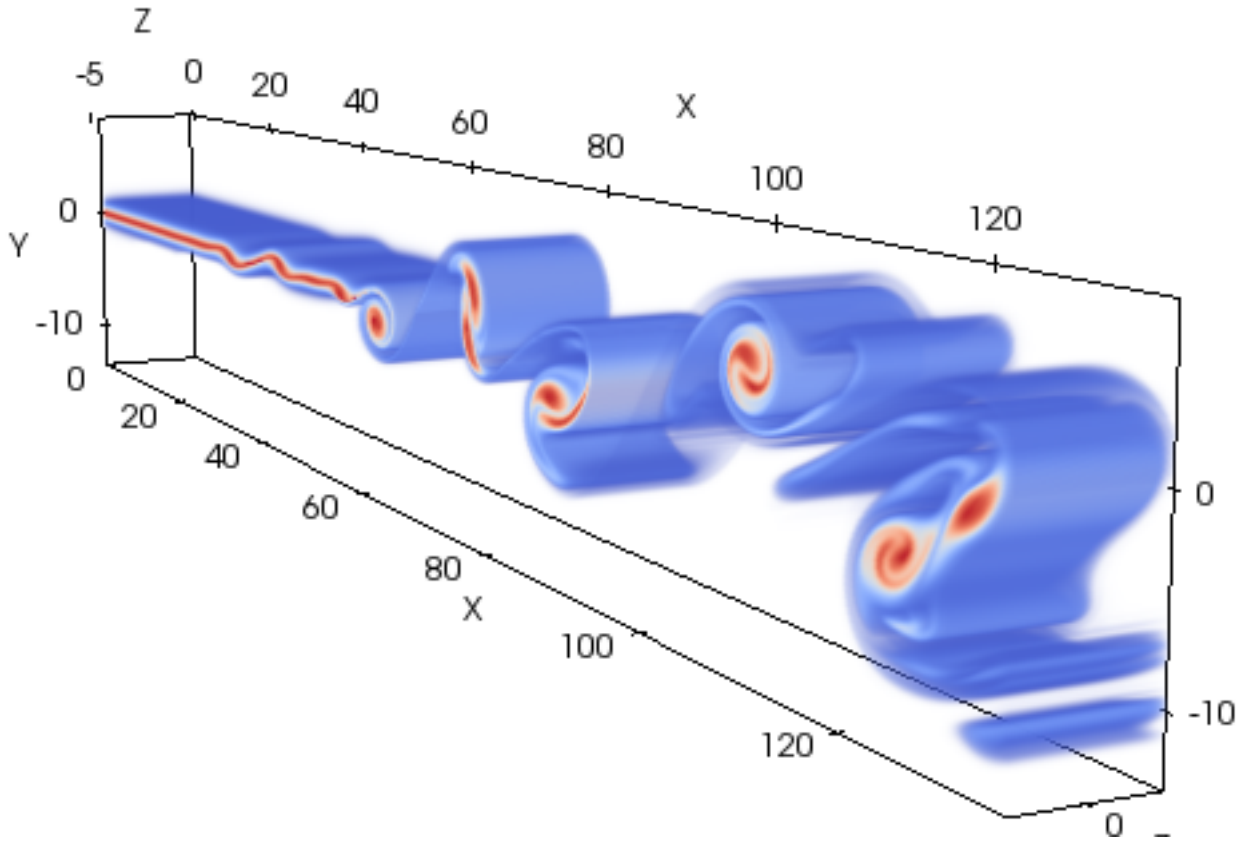

Figure C.1: 3-D view of the norm of $\boldsymbol{\omega}$ saturated at the value of $\omega_{init,max}$ at t = 275 $(1.41 \cdot t_{conv})$.

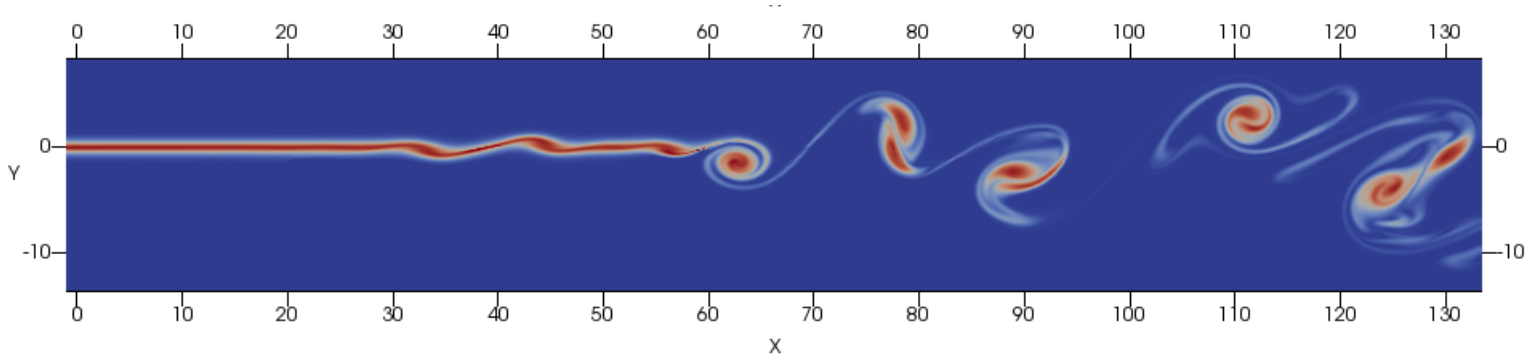

Figure C.2: Spanwise slice in the 3-D view of figure C.1.

C.2 Simulation with white noise at the beginning of the domain

The views presented in this section were obtained from a simulation with a white noise added to the vorticity in a small region at the beginning of the domain, just after the end of the buffer. The flow coming from the buffer was not perturbed by the database. The perturbations on the initial condition were present. Here are some parameters of the simulation :

- $(N_x,\ N_y,\ N_z) = (1280,\ 80,\ 80)$;
- $(L_x,\ L_y,\ L_z) = (134.4,\ 8.4,\ 8.4)$;
- $N_{procs} = 64$.

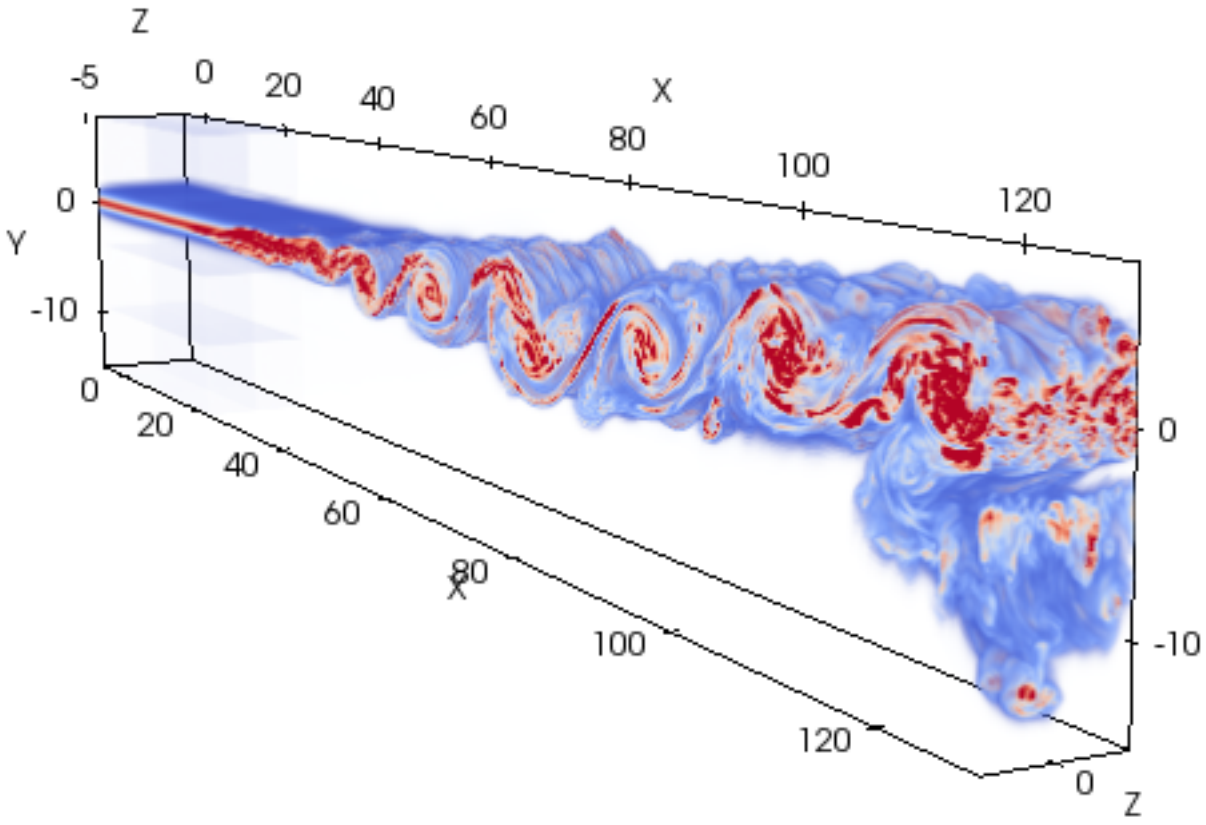

Figure C.3: 3-D view of the norm of $\boldsymbol{\omega}$ saturated at the value of $\omega_{init,max}$ at t = 230 ($1.19 \cdot t_{conv}$).

The figure C.4 comes from a simulation with the same characteristics than the one corresponding to figure C.3, except that the domain is here longer.

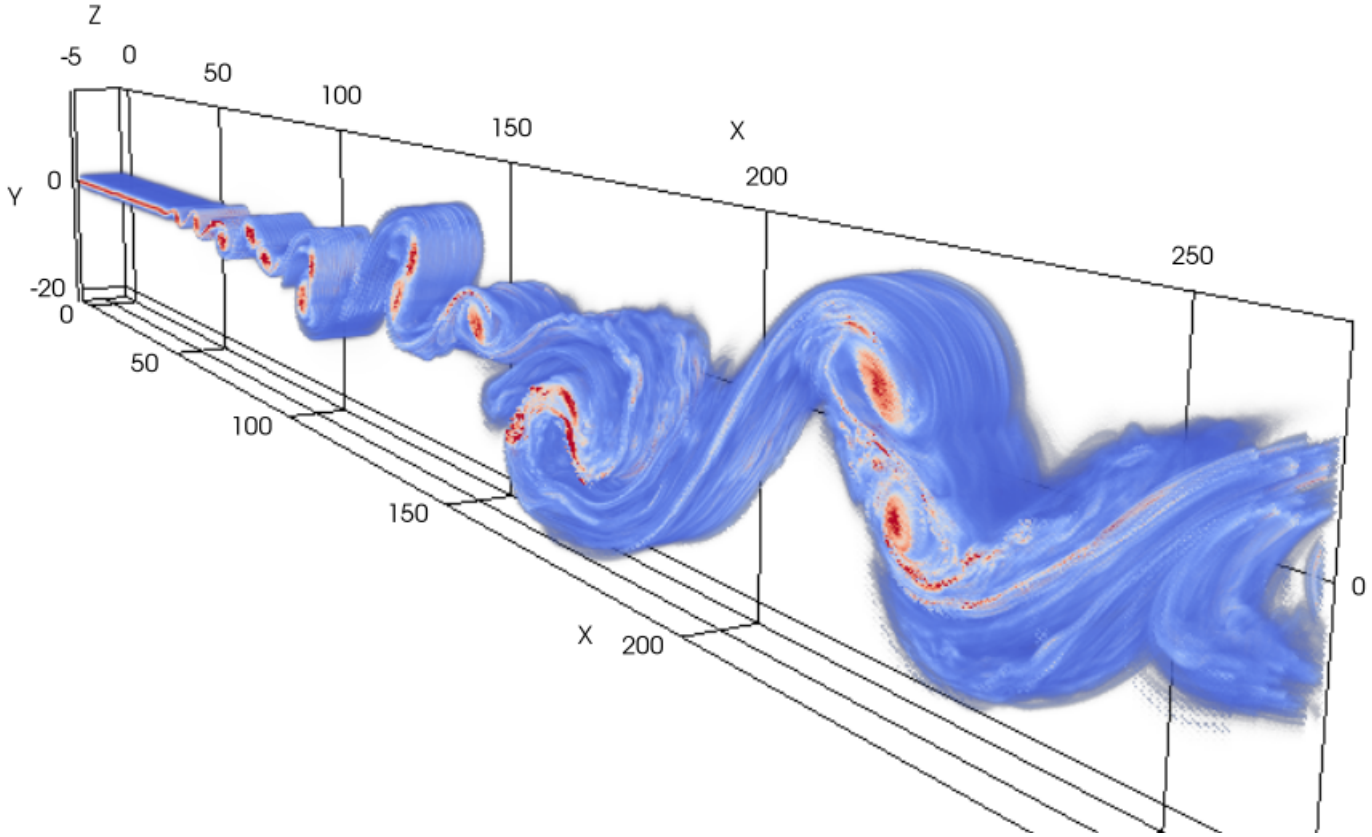

Figure C.4: 3-D view of the norm of $\boldsymbol{\omega}$ saturated at the value of $\omega_{init,max}$ at t = 320 $(0.82 \cdot t_{conv})$.

D | Additional views

D.1 2-D views at a given time

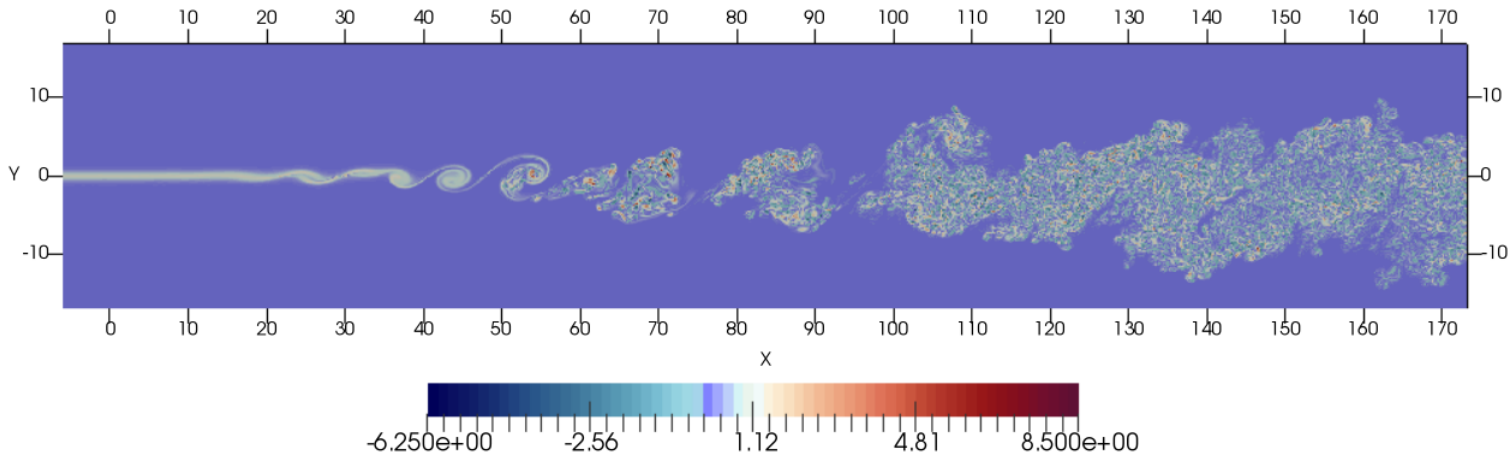

Figure D.1: Slice of $\omega_z/\omega_{init,max}$ at t = 812 $(3.12 \cdot t_{conv})$.

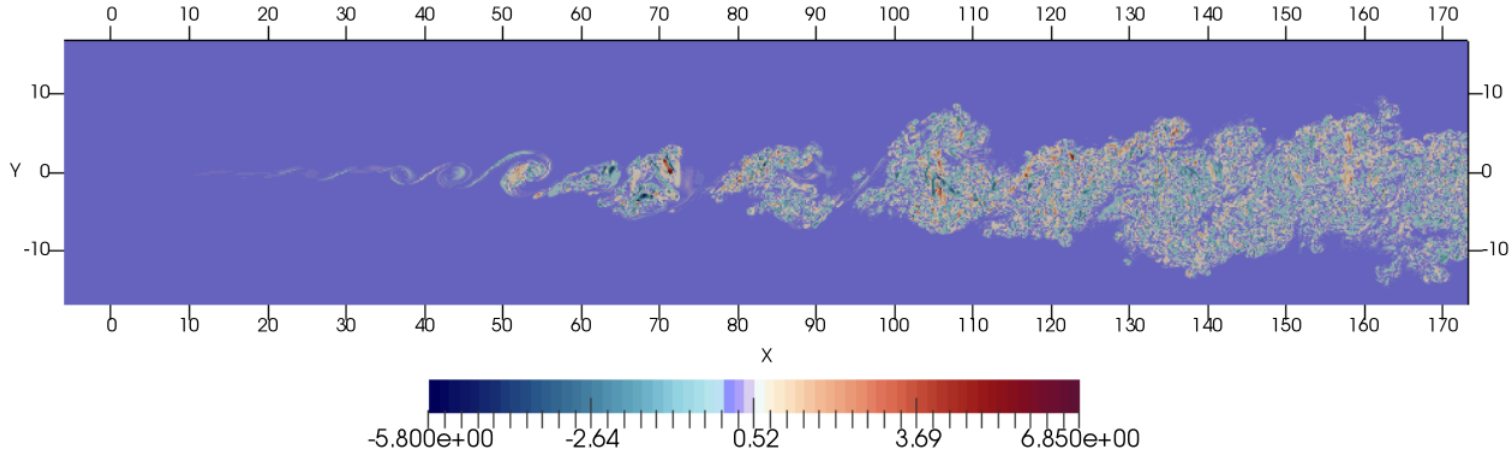

Figure D.2: Slice of $\omega_y/\omega_{init,max}$ at t = 812 $(3.12 \cdot t_{conv})$.

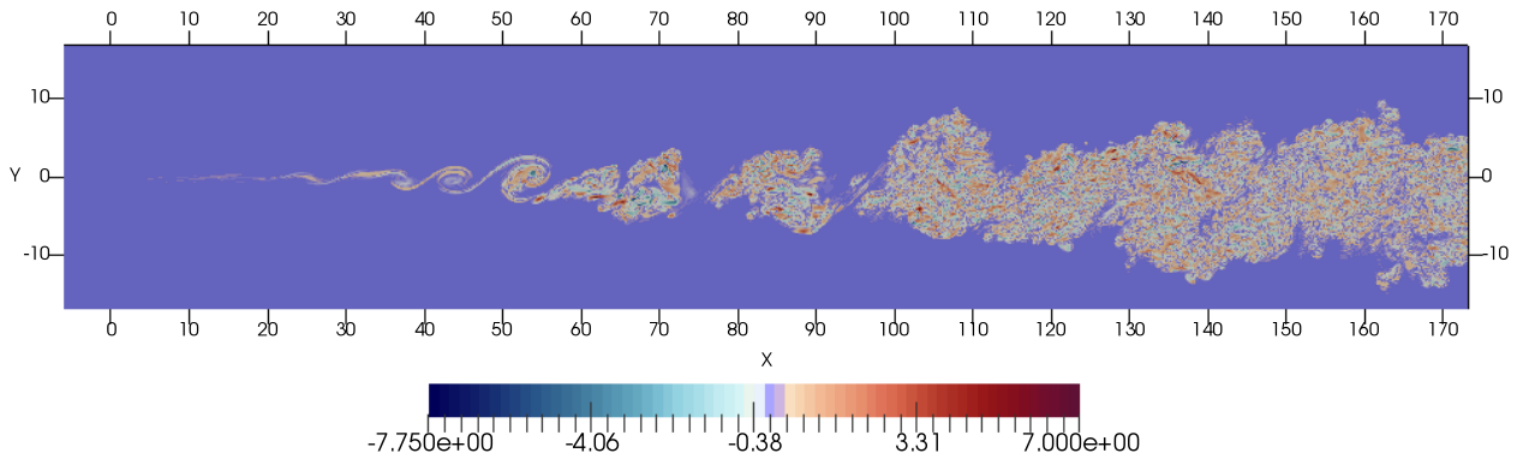

Figure D.3: Slice of $\omega_x/\omega_{init,max}$ at t = 812 $(3.12 \cdot t_{conv})$.

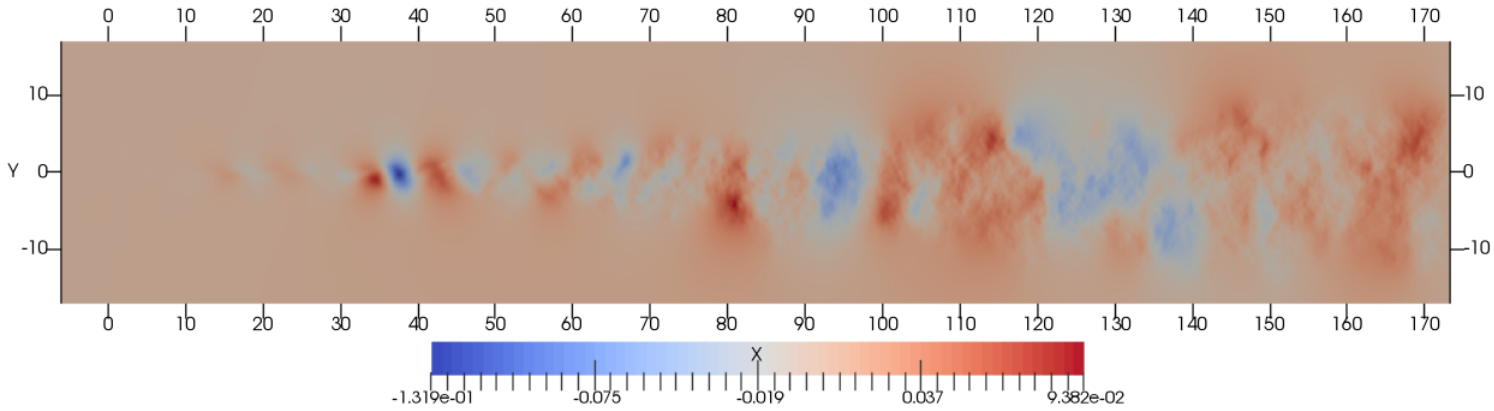

Figure D.4: Spanwise average of v/U_1 at t = 812 $(3.12 \cdot t_{conv})$.

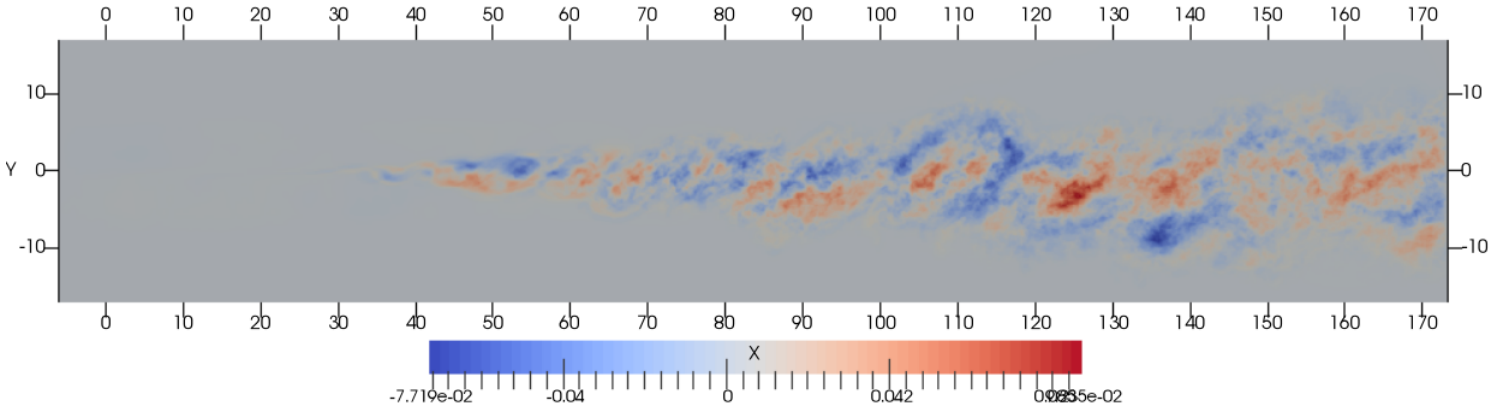

Figure D.5: Spanwise average of w/U_1 at t = 812 $(3.12 \cdot t_{conv})$.

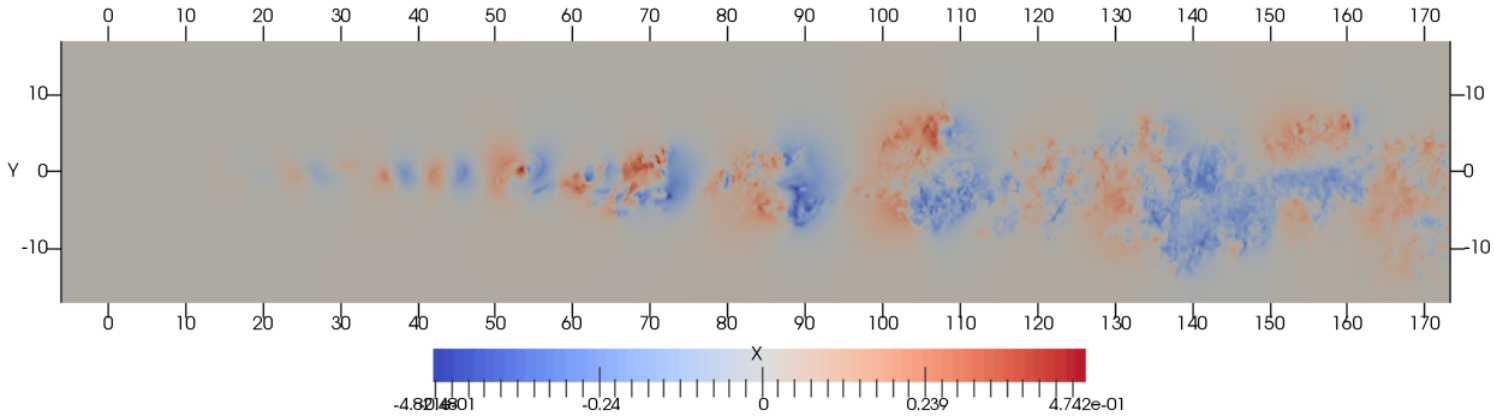

Figure D.6: Slice of v/U_1 at t = 812 ($3.12 \cdot t_{conv}$).

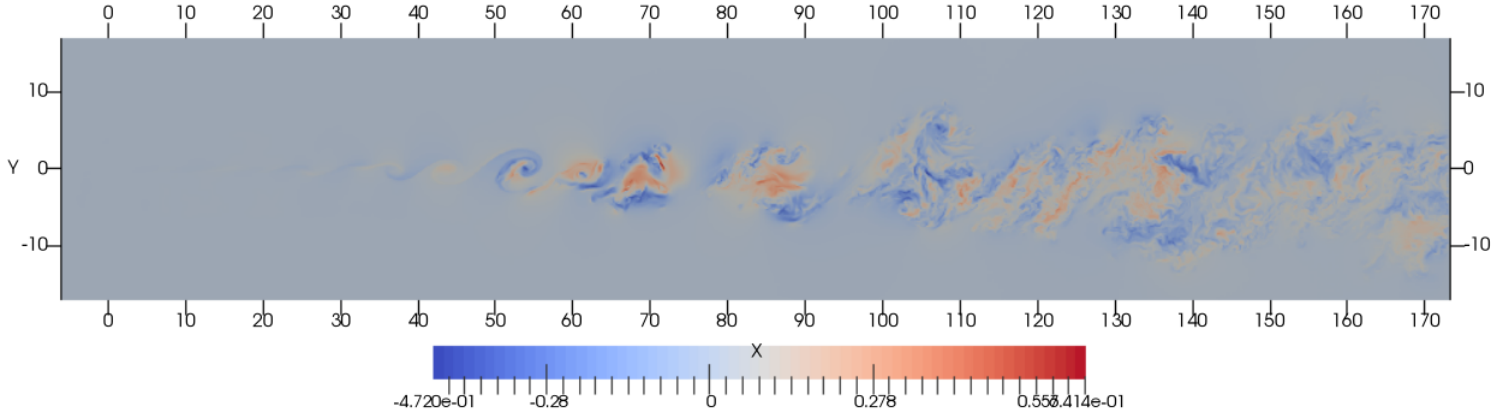

Figure D.7: Slice of w/U_1 at t = 812 ($3.12 \cdot t_{conv}$).

D.2 Averaged 2-D views

The views presented in this section result from the temporal averaging of the quantities over a period $T = 430$.

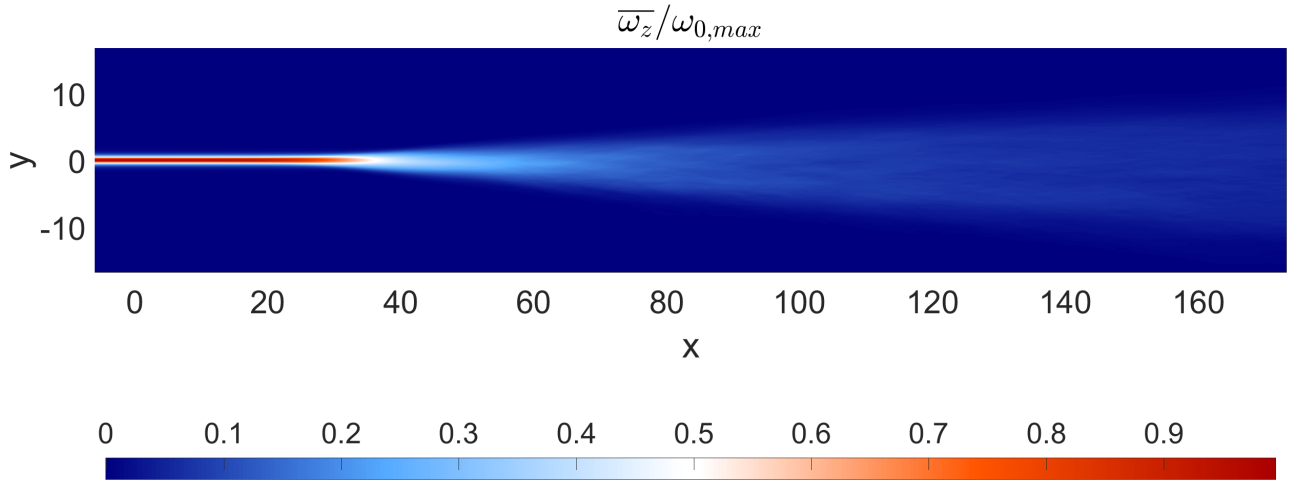

Figure D.8: Spanwise average of $\overline{\omega_z}/\omega_{0,max}$.

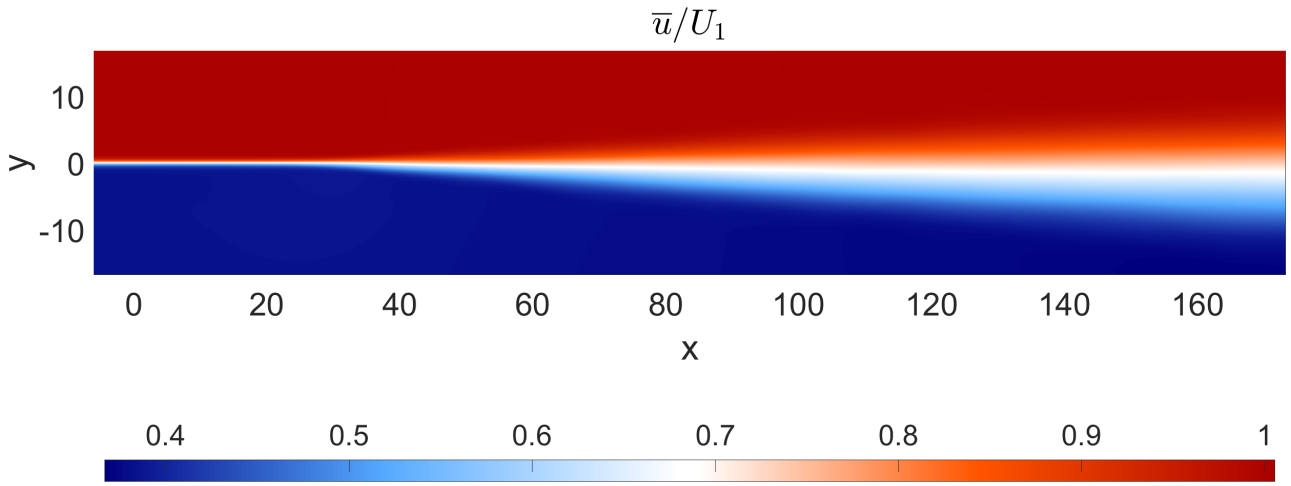

Figure D.9: Spanwise average of $\overline{u}/U_1$.

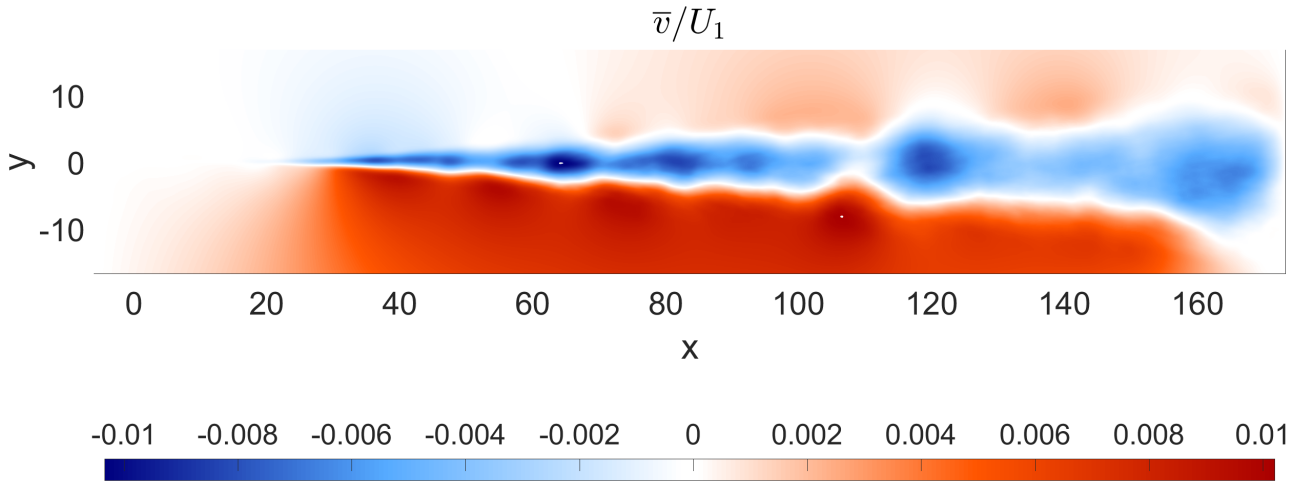

Figure D.10: Spanwise average of $\overline{v}/U_1$.

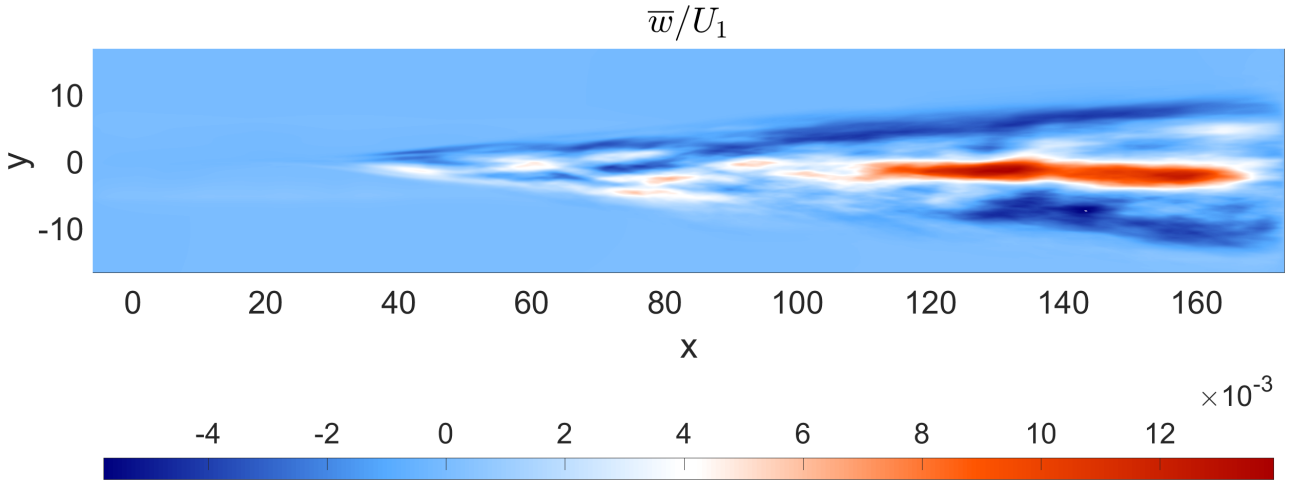

Figure D.11: Spanwise average of $\overline{w}/U_1$.

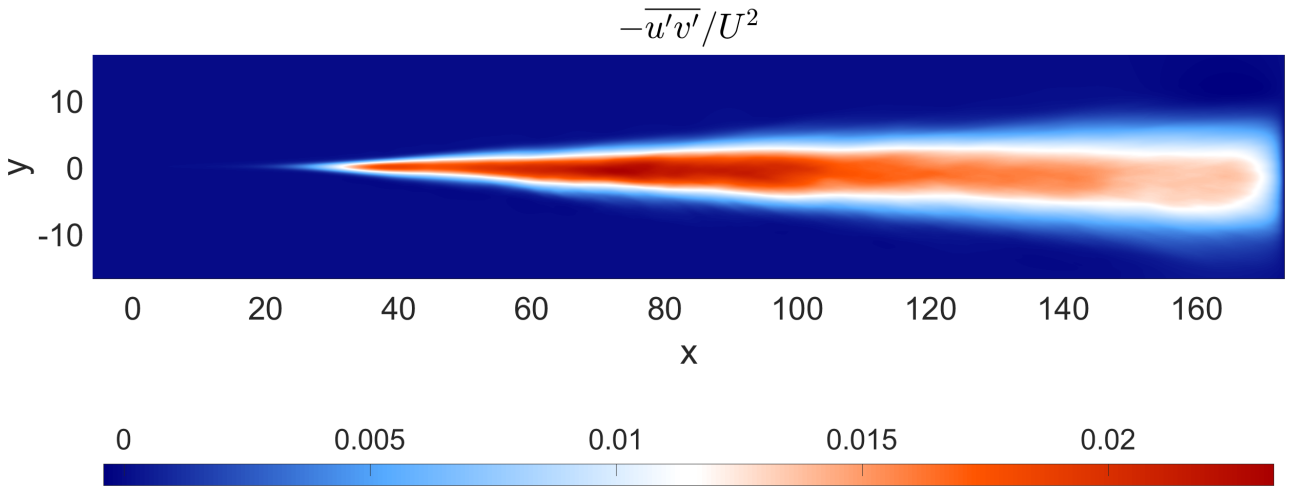

Figure D.12: Spanwise average of $-\overline{u'v'}/(\Delta U)^2$.

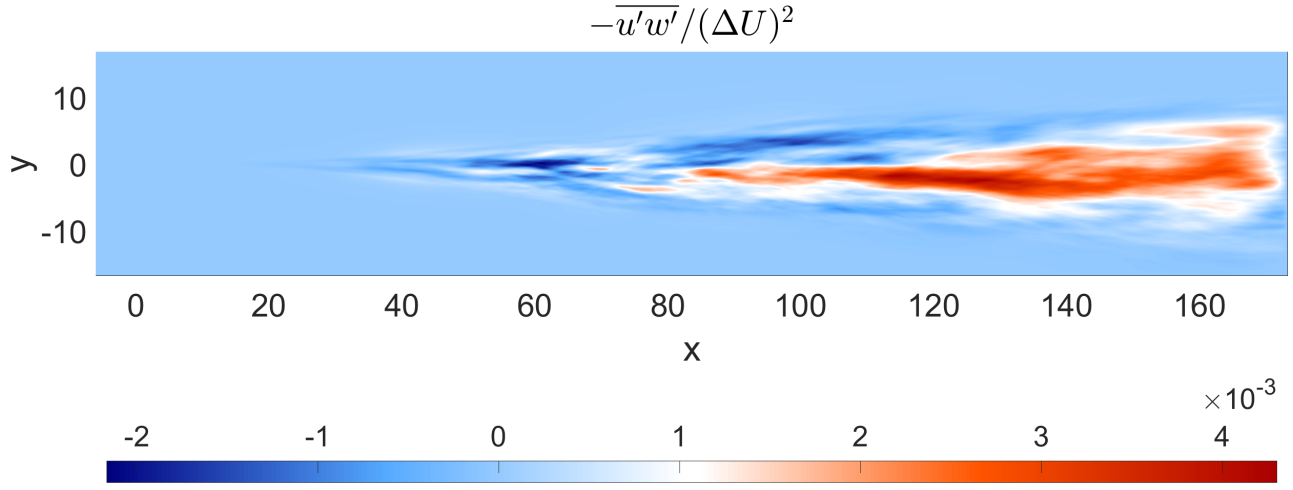

Figure D.13: Spanwise average of $-\overline{u'w'}/(\Delta U)^2$.

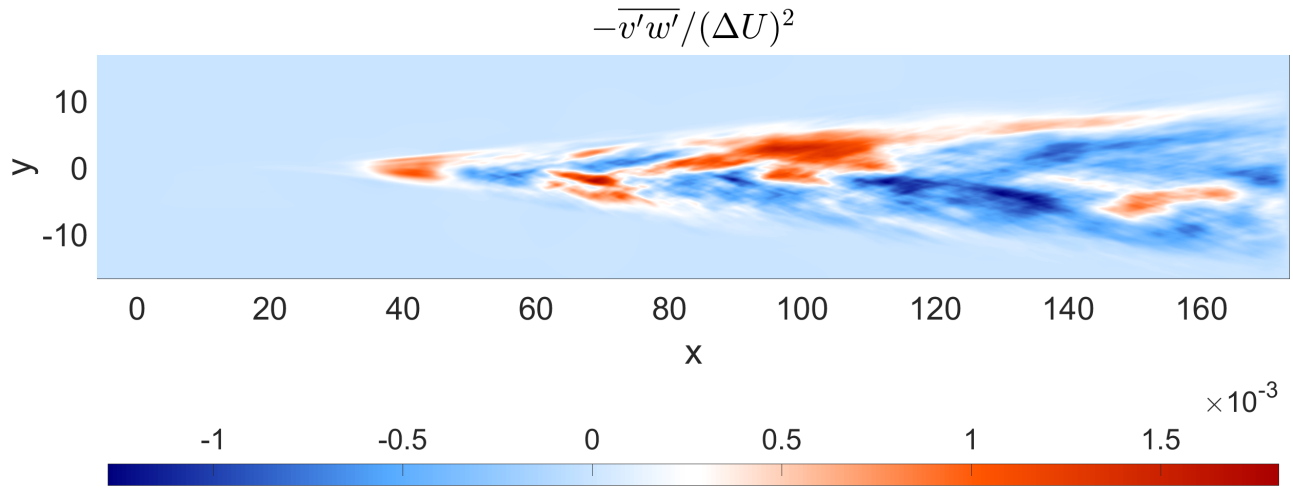

Figure D.14: Spanwise average of $-\overline{v'w'}/(\Delta U)^2$.

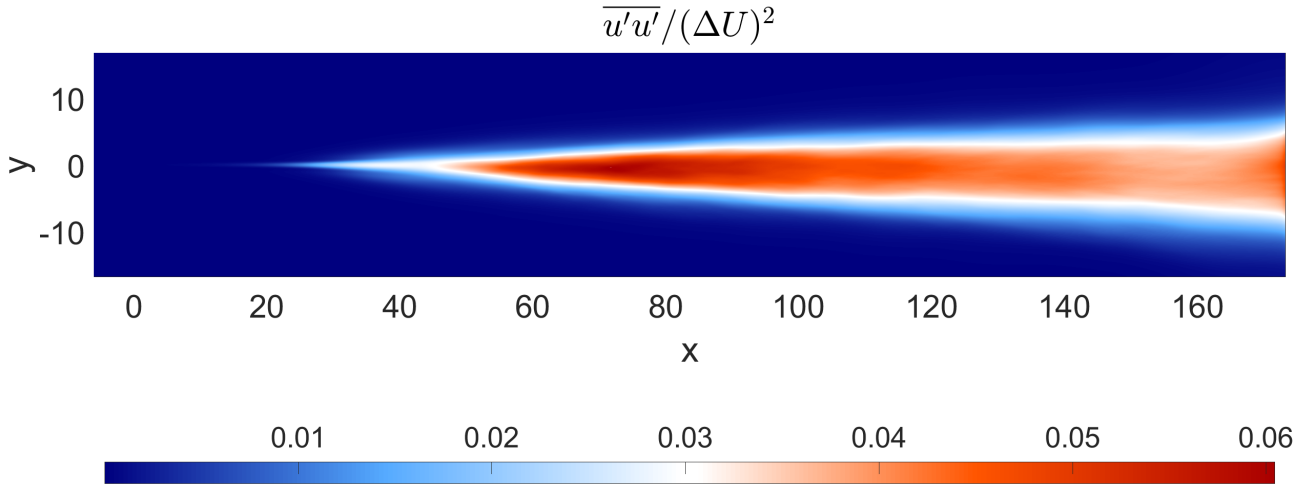

Figure D.15: Spanwise average of $\overline{u'u'}/(\Delta U)^2$.

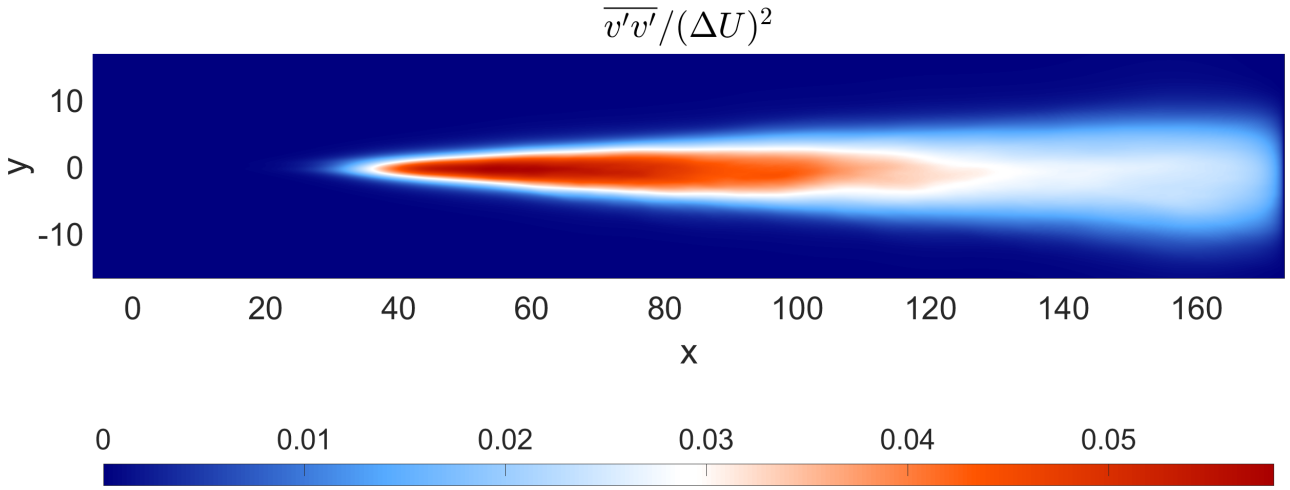

Figure D.16: Spanwise average of $\overline{v'v'}/(\Delta U)^2$.

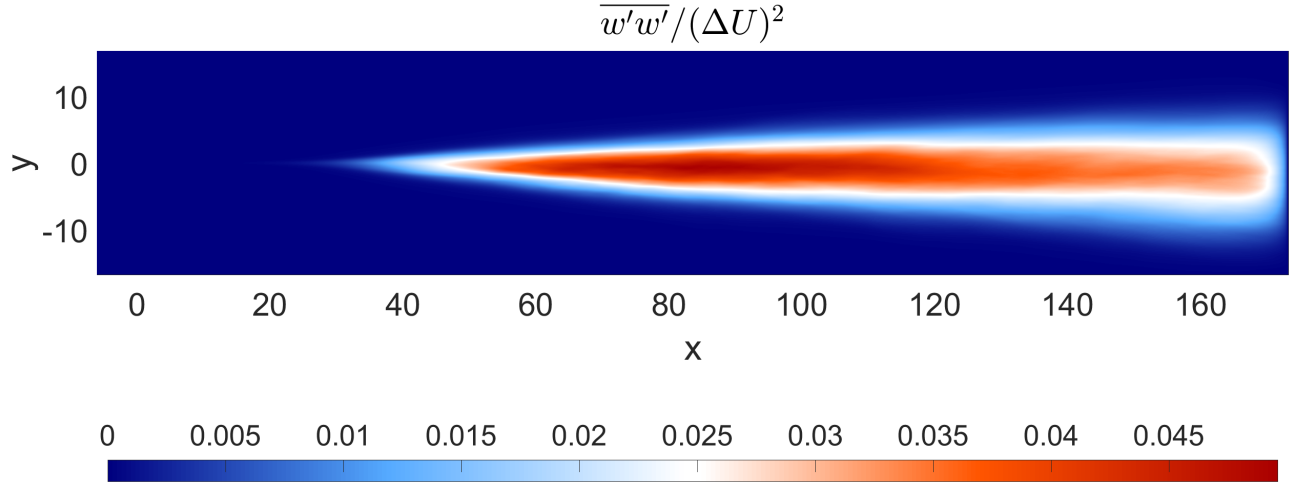

Figure D.17: Spanwise average of $\overline{w'w'}/(\Delta U)^2$.

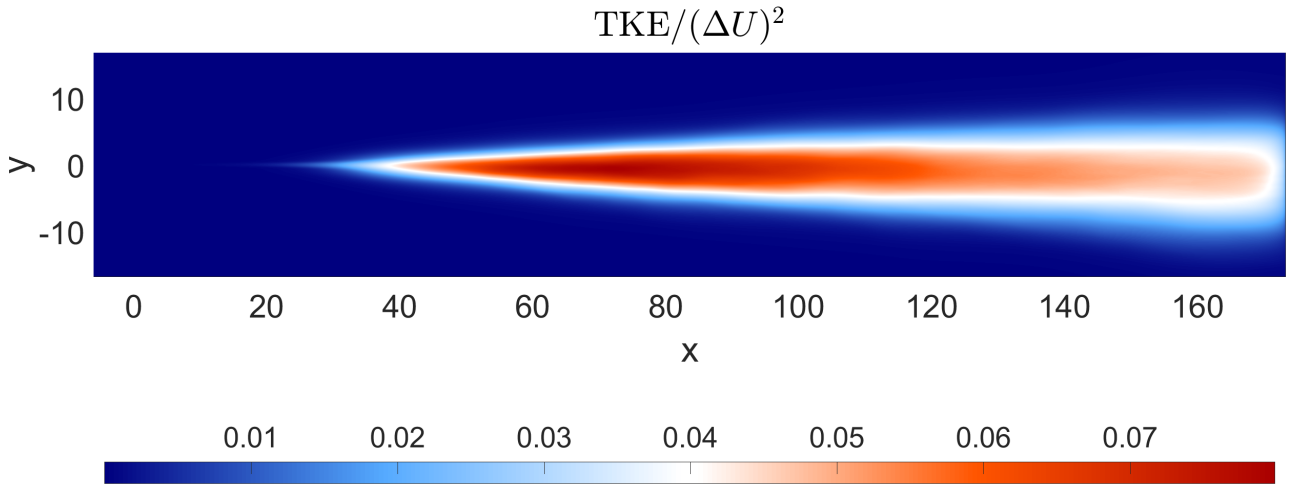

Figure D.18: Spanwise average of the turbulent kinetic energy $\overline{k}/(\Delta U)^2$.

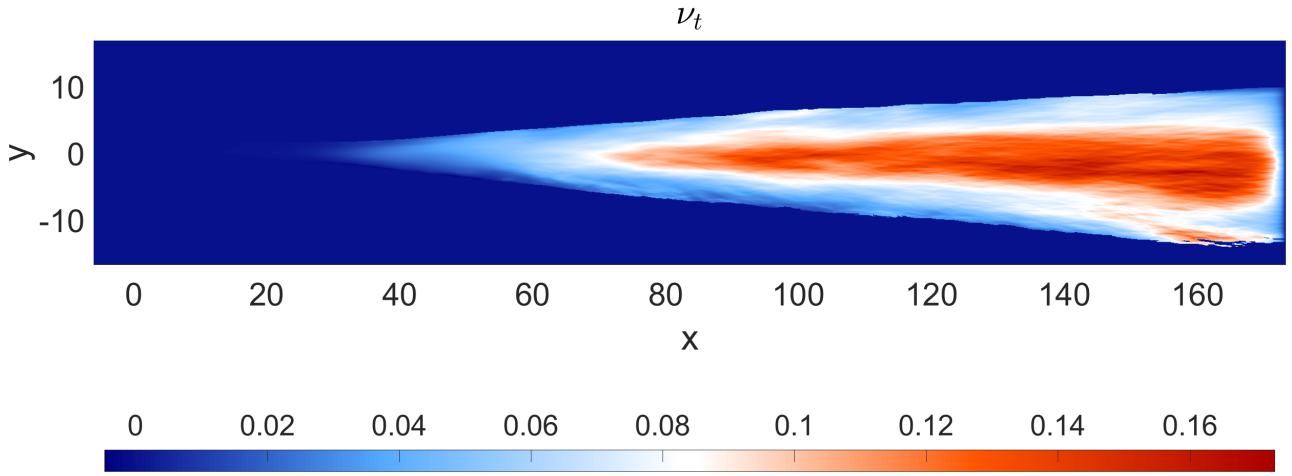

Figure D.19: Spanwise average of the turbulent viscosity $\nu_t = -\overline{u'v'}/\frac{\partial \overline{u}}{\partial y}$.

D.3 3-D views

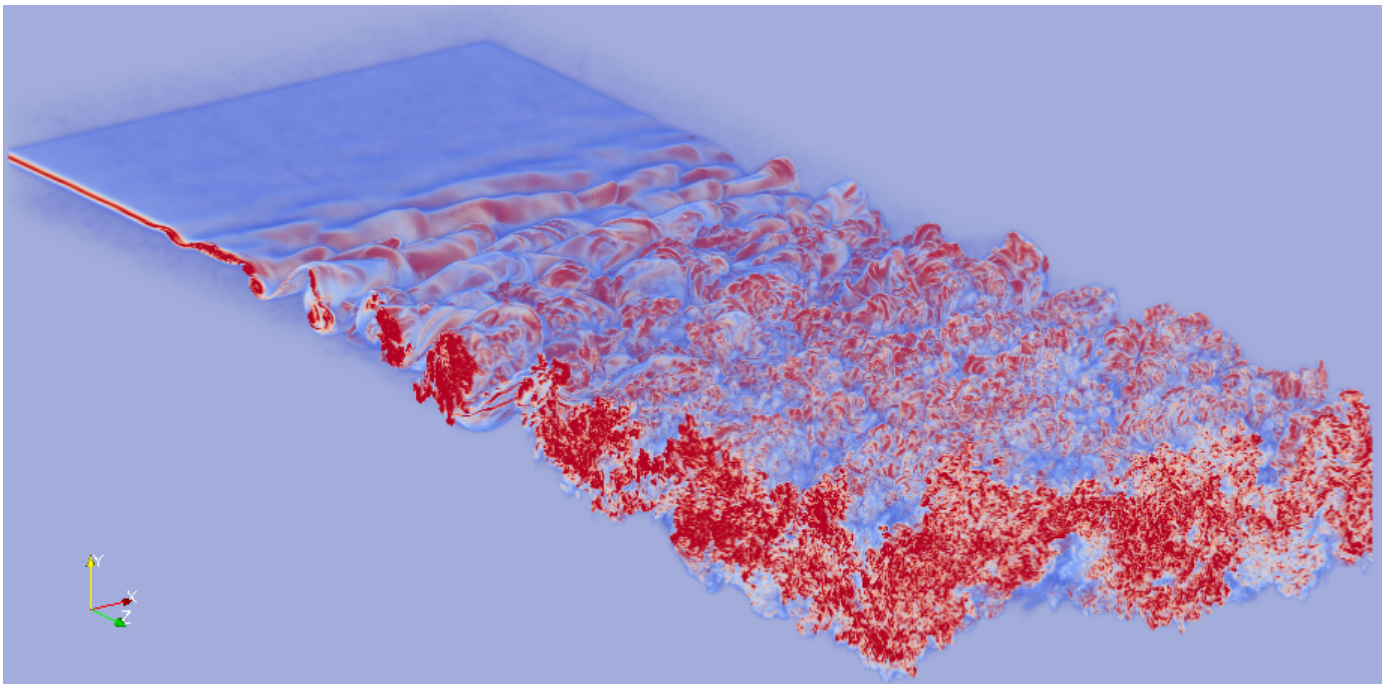

Figure D.20: 3-D view of the magnitude of the vorticity field saturated at the value of $\omega_{init,max}$ at t = 800 ($3.08 \cdot t_{conv}$).

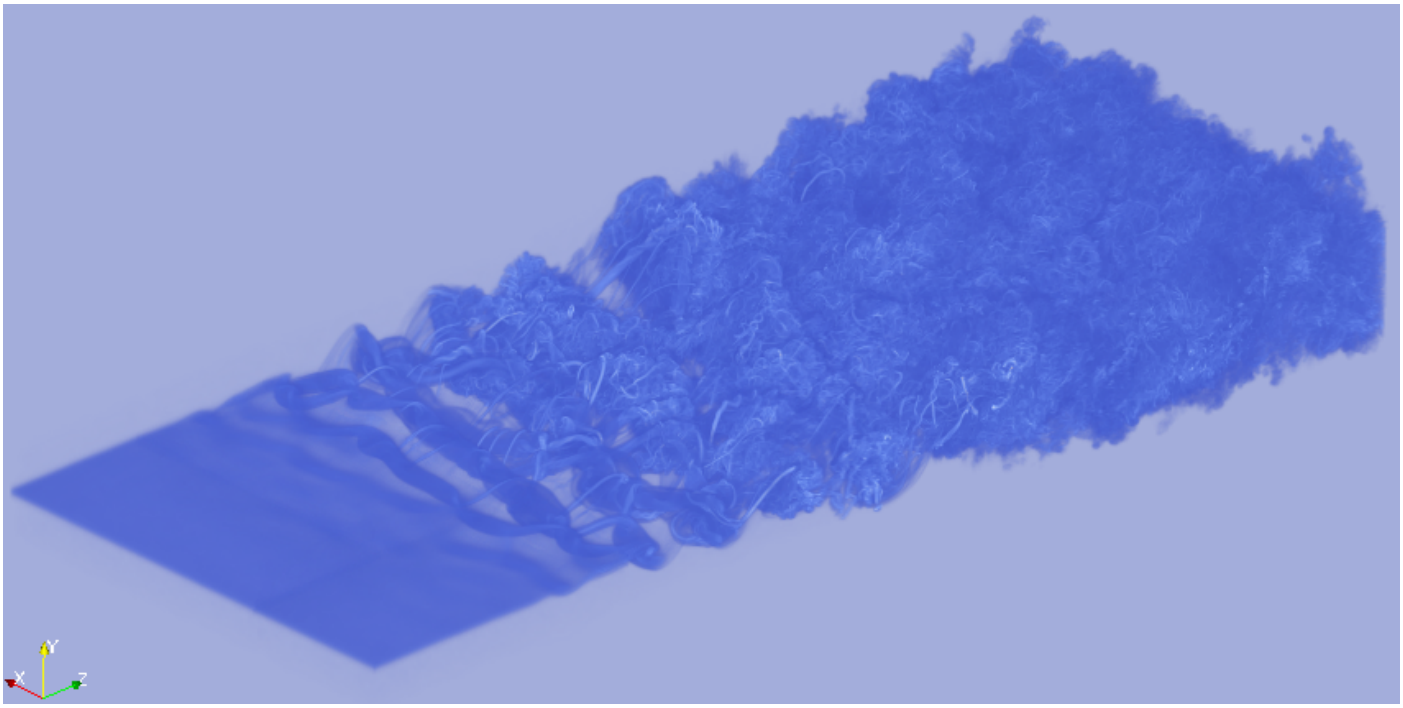

Figure D.21: 3-D view of the magnitude of the vorticity field at t = 800 ($3.08 \cdot t_{conv}$).

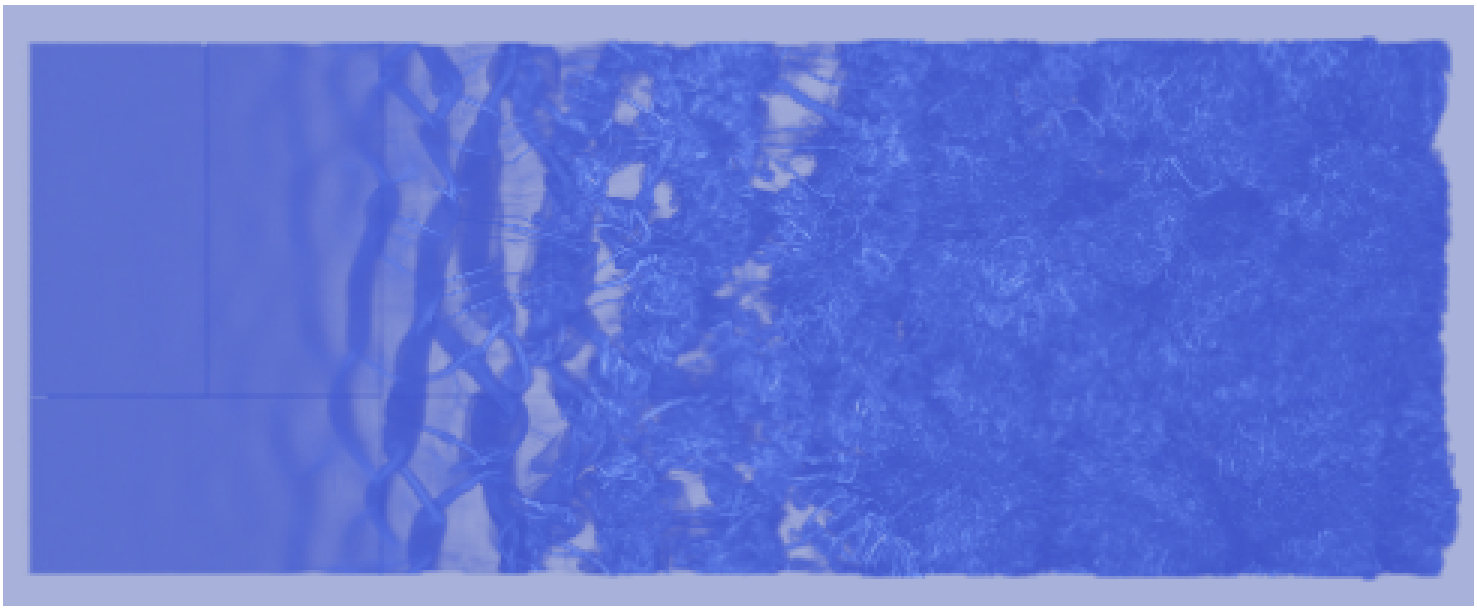

Figure D.22: View from the top of the magnitude of the vorticity field at t = 800 ($3.08 \cdot t_{conv}$)

Rue Archimède, 1 bte L6.11.01, 1348 Louvain-la-Neuve **www.uclouvain.be/epl**